

Spinon-like excitations in spin-1/2 quantum antiferromagnets

Présentée le 5 avril 2022

Faculté des sciences de base
Laboratoire de magnétisme quantique
Programme doctoral en physique

pour l'obtention du grade de Docteur ès Sciences

par

Irina SAFIULINA

Acceptée sur proposition du jury

Prof. L. Villard, président du jury
Prof. H. M. Rønnow, Dr M. Enderle, directeurs de thèse
Prof. M. Mourigal, rapporteur
Prof. T. Perring, rapporteur
Prof. F. Mila, rapporteur

ACKNOWLEDGEMENTS

First and foremost, I am extremely grateful to my supervisors – Mechthild and Henrik. They introduced me to the world of quantum magnetism and inelastic neutron scattering. They gave me the opportunity to work on advanced fundamental problems in the field of magnetism, and I hope I did not disappoint them. I was fortunate enough to work with two geniuses, and each of them equally guided me throughout my PhD.

I want to thank Mechthild for her patience and attention to all the problems that have arisen during my PhD. For teaching me to be careful when processing and interpreting the data. For accompanying me in all my experiments. For helping me not to lose hope when one of the experiments turned out to be not as successful as I would like. In addition, her brilliant sense of humour never let me give up.

I am equally grateful to Henrik for his support, especially during the first Covid lockdown. I am grateful to him for his creativity, for a constant source of ideas, for introducing me to a huge number of scientists who helped me during my PhD both with advice and in conducting experiments.

Besides my advisors, I would like to thank the rest of my thesis committee: Prof. Laurent Villard, Prof. Frédéric Mila, Prof. Martin Mourigal, and Prof. Toby Perring for accepting to be a part of my thesis Jury. I appreciate their valuable comments and interesting scientific discussion during my Oral Exam.

My sincere thanks go to Dr. Bjorn Fåk for his constant support during all time-of-flight experiments and in the following data analysis and interpretation. His teaching talent has helped me to understand the basics of neutron scattering more than once.

I want to thank ILL Graduate School supervised by H. Fischer. ILL gave me access to high-end equipment and provided me with many courses and lectures to broaden my scientific horizons. I would also thank EPFL for giving me the opportunities to travel for schools and conferences and for the valuable courses, including French lessons.

Additionally, in no particular order, I want to thank the following people for preparing or participating in this work at ILL, EPFL, and ISIS: U. Hansen, J. Olivier, A. Wildes, N. Qureshi, M. Boehm, P. Steffens, C. Ritter, E. Suard, P. Chevalier, E. Lelievre-Berna, L. Mangin-Thro, I. Zivkovic, P. Babkevich, R. Stewart, P. Biswas. I would like to acknowledge A. Kurbakov from PNPI (Gatchina, Russia) for sample availability and fruitful discussions.

I want to extend my sincere thanks to ILL and EPFL PhD students and their relatives with whom I completed my doctoral studies (in no particular order): Stas, Anya, Ursula, Ana, Radu, Loreto, Silvia, Palmerina, Quentin, Marta, Giuseppe, Madeleine, Mohammed, Maria, Zhanar, Angel,

Gaynor, Edmond, Lukas, Francesca, Murias, Carmen, Peter, Antonio, Virgile and Luc (EPFL team). Without you guys, my pastime would not have been so cheerful.

Finally, I want to thank my husband for his constant care, support, and help. Thanks to him, I am finishing my PhD, and my inspiration from science did not fade away.

ABSTRACT

Quantum magnetism remains a hot topic in condensed matter physics due to its complexity and possible powerful and significant applications in data storage and memory. To understand how the materials can achieve these goals, one should have a clear idea about the fundamentals behind it. In this thesis, we focus on three examples that can help us deepen the knowledge in many-body effects, which stand to be crucial for quantum magnetism.

(1) The well-known **CuSO₄·5D₂O** material has already demonstrated the model behaviour as one-dimensional Heisenberg antiferromagnet in zero and high ($H > H_{sat}$) fields. The fully-polarized magnetic ground state is described by linear spin-wave theory with magnons, whereas at zero field, the excitations are pairs of topological excitations called spinons. In an intermediate field, the dynamic properties are even more complicated. The inelastic spectrum cannot be reproduced without considering exotic elementary excitations and bound states such as psinons and Bethe strings. Although Bethe in 1931 provided an exact solution for 1D Heisenberg systems, there is still no quantitative comparison between theory and experiment.

(2) The magnetic ground state and hence the dynamic properties of the gemstone mineral green diopside, **Cu₆[Si₆O₁₈] · 6H₂O** are under debate: starting from controversial theories and continuing with non-explained experimental observations. Diopside is a quasi-one-dimensional spin chain with dominant antiferromagnetic interactions. Recent studies claim the classical spin chain behaviour and absence of any quantum fluctuations in the system. In contrast, our experimental findings indicate the presence of continuous excitations above and below T_N .

(3) Newly synthesized material **CuSb₂O₆** of rosielite-type structure tends to become a quantum spin-liquid (QSL) candidate since the magnetic cations Cu²⁺ are arranged in trigonal layers, and no long-range order is observed down to 2 K. The idea of QSL on the triangular lattice was proposed by P. Anderson in 1973. Since his work, a lot of efforts have been made to explore deeper, both theoretically and experimentally, this state. As for now, there are several requirements needed to be met – small spin number, absence of long-range order or spin freezing, long-range entanglement, and the associated fractional spin excitations. We aim to establish whether or not CuSb₂O₆ can be considered as a potential quantum spin-liquid candidate employing different techniques suitable for a powder sample.

Keywords: quantum spin liquids, quantum spin chains, frustration, inelastic neutron scattering, Heisenberg antiferromagnets, polarized neutrons, time-of-flight spectroscopy.

RÉSUMÉ

Le magnétisme quantique reste un sujet brûlant en physique de la matière condensée en raison de sa complexité et de ses possibles applications puissantes et importantes dans le stockage de données et la mémoire. Pour comprendre comment les matériaux peuvent atteindre ces objectifs, il faut avoir une idée claire des principes fondamentaux qui les sous-tendent. Dans cette thèse, nous nous concentrons sur trois exemples qui peuvent nous aider à approfondir les connaissances sur les effets à N corps, ce qui s'avère crucial pour le magnétisme quantique.

(1) Le matériau bien connu $\text{CuSO}_4 \cdot 5\text{D}_2\text{O}$ a déjà démontré le comportement du modèle en tant qu'antiferromagnétique de Heisenberg unidimensionnel dans des champs nuls et élevés ($H > H_{\text{sat}}$). L'état fondamental magnétique totalement polarisé est décrit par la théorie des ondes de spin linéaires avec des magnons alors qu'à champ nul les excitations sont des paires d'excitations topologiques appelées spinons. Dans un domaine intermédiaire, les propriétés dynamiques sont encore plus compliquées. Le spectre inélastique ne peut pas être reproduit sans considérer les excitations élémentaires exotiques et les états liés tels que les psinson et les cordes de Bethe. Bien que Bethe en 1931 ait fourni une solution exacte pour les systèmes Heisenberg 1D, il n'y a toujours pas de comparaison quantitative entre la théorie et l'expérience.

(2) L'état fondamental magnétique et donc les propriétés dynamiques de la diopase verte minérale de pierre précieuse, $\text{Cu}_6[\text{Si}_6\text{O}_{18}] \cdot 6\text{H}_2\text{O}$ sont en débat : partir de théories controversées et continuer avec des observations expérimentales non expliquées. La diopase est une chaîne de spin quasi unidimensionnelle avec des interactions antiferromagnétiques dominantes. Des études récentes revendiquent le comportement classique de la chaîne de spin et l'absence de fluctuations quantiques dans le système. En revanche, nos résultats expérimentaux indiquent la présence d'excitations continues au-dessus et au-dessous de T_N .

(3) Le matériau CuSb_2O_6 nouvellement synthétisé de structure de type rosiaite tend à devenir un candidat liquide de spin quantique (QSL) puisque les cations magnétiques Cu^{2+} sont disposés en couches trigonales et aucun ordre à longue distance n'est observé jusqu'à 2 K. L'idée de QSL sur le réseau triangulaire a été proposée par P. Anderson en 1973. Depuis ses travaux, de nombreux efforts ont été déployés pour explorer plus profondément, à la fois théoriquement et expérimentalement, cet état. Pour l'instant, plusieurs exigences doivent être remplies – petit nombre de spins, absence d'ordre à longue distance ou de gel de spin, intrication à longue distance et les excitations de spin fractionnaires associées. Nous visons à établir si CuSb_2O_6 peut être considéré comme un candidat potentiel liquide de spin quantique en utilisant différentes techniques adaptées à un échantillon de poudre.

Mots clés: liquides de spin quantiques, chaînes de spin quantiques, frustration, diffusion inélastique de neutrons, antiferromagnétiques de Heisenberg, neutrons polarisés, spectroscopie de temps de vol.

Contents

Acknowledgments	1
Abstract	3
Résumé	4
List of Figures	6
List of Tables	11
List of Acronyms	12
1 Introduction	13
2 Methods	17
2.1 Neutron scattering	17
2.1.1 Nuclear scattering	18
2.1.2 Magnetic scattering	18
2.1.3 Neutron techniques and instrumentation	19
2.2 Linear spin-wave theory	26
2.3 Reverse Monte Carlo	26
2.4 Magnetic susceptibility	27
2.5 Specific heat	27
2.6 Muon spectroscopy	28
3 Field-dependent dynamics in $\text{CuSO}_4 \cdot 5\text{D}_2\text{O}$	29
3.1 Quantum spin-1/2 antiferromagnetic spin chains in zero and non-zero magnetic field	29
3.2 State of the art $\text{CuSO}_4 \cdot 5\text{D}_2\text{O}$	33
3.3 Time-of-flight experiment	35
3.3.1 Experimental details	35
3.3.2 Data reduction in Mantid	35

3.3.3	Crystal orientation	36
3.3.4	Background subtraction	38
3.3.5	Incoherent scattering	41
3.3.6	Magnetic form-factor	43
3.3.7	Multiple scattering	44
3.3.8	Magnetization values	48
3.3.9	Proper average for unpolarized neutrons	52
3.3.10	Comparison with theory	53
3.4	Polarization analysis	57
3.4.1	Vertical magnetic field	58
3.4.2	Horizontal magnetic field	61
3.5	Summary	69
4	Quantum nature of magnetic excitations in $\text{Cu}_6[\text{Si}_6\text{O}_{18}] \cdot 6\text{H}_2\text{O}$	70
4.1	A sea of conflicts	71
4.2	Magnetic structure determination	73
4.3	Magnetic excitations in ordered state	77
4.4	Evidence of quantum fluctuations above and below T_N	79
4.5	Summary	81
5	Dynamics in frustrated triangular antiferromagnet CuSb_2O_6	82
5.1	Frustration	82
5.2	Triangular lattice	84
5.3	Quantum spin liquid concept	87
5.4	Sample characterization	88
5.4.1	Powder diffraction	89
5.4.2	DC susceptibility	90
5.4.3	Specific heat	93
5.5	Absence of long-range magnetic order	96
5.6	Magnetic excitations in CuSb_2O_6	100
5.7	Character of spin correlations in CuSb_2O_6	106
5.8	Summary	111
6	Conclusion	112

List of Figures

1.1	Classical antiferromagnetic spin-wave dispersion and dynamical structure factor of KCuF_3	14
1.2	RVB states on triangular and kagome lattices	14
1.3	Fractionalisation in three-dimensional spin systems	15
2.1	Layout of a D2B@ILL instrument	21
2.2	Layout of a D3@ILL instrument	22
2.3	Layout of a triple-axis-spectrometer	23
2.4	Layout of IN5@ILL time-of-flight instrument	25
3.1	Plots of the two- and four-spinon parts of the dynamical structure factor at momenta $k = \pi/4, \pi/2, 3\pi/4$ and π	31
3.2	Lineshapes of dynamical structure factors $S^{zz}(q, \omega)$, $S^{+-}(q, \omega)$, $S^{-+}(q, \omega)$ of spin-1/2 Heisenberg antiferromagnetic spin chain calculated for different magnetization values	32
3.3	Dynamical structure factor calculated by M. Kohno for $M = 40, 80, 120$	33
3.4	Magnetic unit cell and interactions scheme of $\text{CuSO}_4 \cdot 5\text{D}_2\text{O}$	34
3.5	Excitation spectrum of $\text{CuSO}_4 \cdot 5\text{D}_2\text{O}$ in the fully polarized state	34
3.6	Aligned $\text{CuSO}_4 \cdot 5\text{D}_2\text{O}$ sample used for the IN5@ILL experiment.	35
3.7	Measured dynamic structure factor $S(Q, \omega)$ along chain direction in vertical magnetic fields $H = 0, 1.5, 3, 3.3, 3.5, 9.5$ T.	37
3.8	Measured dynamic structure factor $S(Q, E)$ of an empty magnet.	37
3.9	Several constant energy cuts showing absence of spin-wave excitations at energies below 0.78 meV at 9.5 T.	38
3.10	Experimental constant momentum transfer cuts with Caux lineplots	40
3.11	Background associated with scattering from the sample environment	41
3.12	Constant energy cuts with prior subtraction of $H = 9.5$ T data.	42
3.13	TOF Experimental maps before multiple scattering correction	43
3.14	Effective magnetic form-factor of Cu^{2+} for TOF experiment	44
3.15	Dynamical structure factor of $H = 0$ T and multiple scattering	45
3.16	Multiple scattering function $\mu(\omega)$ for zero field	46

3.17	Comparison of original and multiple scattering subtracted $H = 0$ T data-sets. . .	46
3.18	Comparison of original and multiple scattering subtracted $H = 9.5$ T data-sets. . .	47
3.19	Dynamical structure factors $S(h, \omega)$ for different field values $H = 0, 1.5, 3, 3.3, 3.5, 9.5$ T with applied magnetic form-factor correction and subtracted background, incoherent and multiple scattering.	47
3.20	Magnetization curve for $S = 1/2$ antiferromagnetic Heisenberg spin chain . . .	49
3.21	$H = 1.5$ T experimental data-set and theoretical $M = 120$ and $M = 126$ calculations.	50
3.22	Gaussian fit of constant energy scans of $H = 1.5$ T data-set and $M = 120$ and $M = 126$ theoretical calculations	50
3.23	Results of sequential fitting of $H = 1.5$ T and $M = 120$ and $M = 126$ theoretical calculations	51
3.24	Magnetization values obtained from IN5@ILL experiment.	52
3.25	Colormaps of the projected prefactors $(1 + \hat{Q}^{z^2})$ and $(1 - \hat{Q}^{z^2})$	53
3.26	Qualitative comparison of experimental dynamical structure factors and Kohno's theoretical calculations	54
3.27	Constant energy cuts for $H = 1.5$ T and $H = 3$ T and its comparison with corresponding theoretical calculations	55
3.28	Constant energy cuts for $H = 3.3$ T and $H = 3.5$ T and its comparison with corresponding theoretical calculations	56
3.29	Constant momentum transfer cuts integrated along selected h regions for intermediate applied magnetic fields.	57
3.30	Bethe strings observed in IN5@ILL experiment.	58
3.31	Longitudinal and transverse cross-sections measured with applied vertical field $H = 1.7$ T at IN14@ILL instrument	59
3.32	$S^{zz}(h, \omega)$ and $\frac{1}{4}(S^{+-}(h, \omega) + S^{-+}(h, \omega))$ obtained by Kohno for $M = 120$. .	60
3.33	Magnetization curve obtained from IN5@ILL experiment and IN14@ILL experiment with vertical field geometry.	61
3.34	Variation of an effective horizontal g -tensor for two copper magnetic subsystems when magnetic field is parallel to the scattering plane.	62
3.35	Intensity maps of the theoretical magnon dispersion in the fully polarized state with vertical and horizontal magnetic field of $H = 5$ T	63
3.36	Constant h -scans measured in horizontal magnetic field $H = 3.4$ T for the paramagnetic mode	64
3.37	Energy-field $E(H)$ dependence for paramagnetic mode at different h values in $\mathbf{Q} = (h, -1/2, -1/2)$ obtained from LSWT.	65

3.38	Dynamical structure factors $S^{-+}(h, \omega)$ and $S^{+-}(h, \omega)$ obtained by Kohno for $M = 120$ and $M = 66$	66
3.39	Comparison of $H = 1.7$ T $S^{+-}(h, \omega)$ and $S^{+-}(h, \omega)$ constant energy scans with theoretical $M = 120$ dynamical structure factors.	67
3.40	Comparison of $H = 1.7$ T $S^{+-}(h)$ and $S^{+-}(h)$ constant energy scans with theoretical $M = 120$ dynamical structure factors (continuation).	68
3.41	Comparison of $H = 3.4$ T $S^{+-}(h)$ and $S^{+-}(h)$ constant energy scans with theoretical $M = 66$ dynamical structure factors.	68
3.42	Comparison of $H = 3.4$ T $S^{+-}(h)$ and $S^{+-}(h)$ constant energy scans with theoretical $M = 66$ dynamical structure factors (continuation).	69
4.1	Crystal structure of $\text{Cu}_6[\text{Si}_6\text{O}_{18}] \cdot 6\text{H}_2\text{O}$	70
4.2	Inelastic neutron spectra measured at time-of-flight CNCS@SNS in diopside at $T = 1.7$ K	72
4.3	LSWT calculations for tilted configurations	73
4.4	LSWT calculations taking into account the tilt of 5° from the c -axis for $(h01.5)$ and $(00l)$ reciprocal directions	76
4.5	LSWT calculations taking into account the tilt of 5° from the c -axis for (hhl) reciprocal direction	78
4.6	Experimental magnetic scattering $ \mathbf{M}_\perp ^2$ measured at different \mathbf{Q} vectors at ThALES instrument.	79
4.7	Calculated spin-wave dispersion along $(00l)$ direction	80
5.1	Examples of geometrical frustration	83
5.2	Frustration caused by competing interactions: square lattice.	83
5.3	Possible ground states for $J_1 - J_2 - J_3$ model in honeycomb lattice	84
5.4	$T = 0$ K phase diagram of the triangular Ising model with nearest J_{nn} and next-nearest-neighbor J_{nnn} interactions.	86
5.5	Ground state of the 2D antiferromagnetic XY model on the triangular lattice.	87
5.6	Example of the triangular arrangement of spins.	88
5.7	RT powder neutron diffraction pattern measured at D2B@ILL.	90
5.8	Magnetic susceptibility of CuSb_2O_6	91
5.9	The magnetization isotherms measured in the field range $(-14 - 14$ T) and in the temperature range $1.7 - 50$ K.	92
5.10	The magnetization isotherms measured in the field range $(0 - 14$ T) and in the temperature range $1.7 - 8$ K	93
5.11	Specific heat C_p of CuSb_2O_6 as a function of temperature in zero field	95
5.12	Magnetic contribution to the specific heat at 0T and 14T applied magnetic field.	96

5.13	Low-temperature ZF- μ SR signals up to 2 K.	97
5.14	ZF- μ SR signals at $T = 46$ mK and $T = 2$ K.	98
5.15	Zero field background-subtracted muon asymmetry curves at 0.046, 10, 50 and 200 K.	99
5.16	Temperature dependence of the μ^+ spin relaxation rate from the zero field μ SR measurements	99
5.17	$S(Q, \omega)$ measured at $T = 1.6, 10, 25$ and 50 K at IN5 with neutron incident energy $E_i = 3.55$ meV	101
5.18	$S(Q, \omega)$ measured at $T = 1.6, 50$ and 100 K at IN5 with neutron incident energy $E_i = 12.1$ meV	101
5.19	$S(Q, \omega)$ measured at $T = 60$ mK at LET with neutron incident energy $E_i =$ 1.03, 1.07, 3.70, and 12.14 meV	102
5.20	$S(Q, \omega)$ measured at $T = 1.7$ K at LET with neutron incident energy $E_i =$ 1.03, 1.07, 3.70, and 12.14 meV	103
5.21	$\chi''(Q, \omega)$ measured at $T = 1.6, 10, 25$, and 50 K at IN5 with neutron incident energy $E_i = 3.55$ meV	104
5.22	$\chi''(Q, \omega)$ measured at $T = 1.6, 50$, and 100 K at IN5 with neutron incident energy $E_i = 12.1$ meV	104
5.23	Wave-vector dependence of $\chi''(Q)$ integrated over the energy range $0.4 < E < 2$ meV	105
5.24	Energy dependence of the imaginary part of the magnetic susceptibility $\chi''(E)$ integrated over momentum transfer range $0.5 < Q < 0.8 \text{ \AA}^{-1}$ for $T = 1.7$ and 0.06 K.	106
5.25	Diffraction patterns measured at D4 instrument at $T = 4$ K and at $T = 20, 30$ and 40 K	107
5.26	Difference diffraction pattern measured at D4 and integrated LET signal in $0.4 < E < 3$ meV energy range	108
5.27	SPINVERT fit results	110
5.28	SPINVERT fit results	111

List of Tables

2.1	List of TAS experiments and their details.	24
2.2	List of TOF experiments and their details.	25
3.1	Field value estimation.	51
3.2	Energy of the paramagnetic and chain modes obtained from the fit	65
4.1	Irreducible representations and their symmetry operations according to the space group $R\bar{3}$ and propagation vector $\mathbf{k} = (0, 0, 1.5)$	74
4.2	Results of D3 experiment	76
5.1	Crystallographic data of CuSb_2O_6 within the framework of the $P\bar{3}1m$ (No. 162) space group at RT observed using neutron powder diffraction data refinement. .	90
5.2	Results of various fits to the magnetization curve	93

List of Acronyms

AFM	Antiferromagnetic
BKT	Berezinskii-Kosterlitz-Thouless
CRYOPAD	Cryogenic Polarization Analysis Device
FC	Field cooled
FM	Ferromagnetic
LRMO	Long-range magnetic order
LSWT	Linear spin wave theory
NSF	Non spin-flip
QSL	Quantum Spin Liquid
RMC	Reverse Monte Carlo
RT	Room temperature
RVB	Resonating Valence Bond
SAF	Superantiferromagnetic
SF	Spin-flip
TAS	Triple-axis spectrometry
TLL	Tomonaga-Luttinger liquid
TOF	Time-of-flight
ZFC	Zero-field cooled

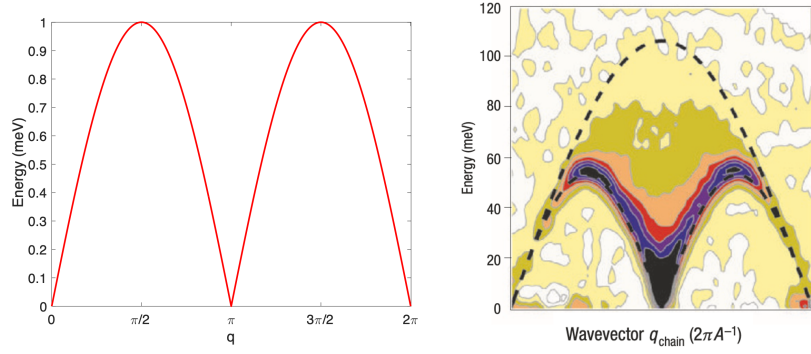
CHAPTER 1

INTRODUCTION

Spinons are a commonly used characteristic associated with the spin-liquid behavior. At the moment, there are many reviews [1–6] devoted to quantum spin liquids, their experimental realizations, as well as theoretical aspects of the corresponding ground state. Here, we present the selected properties of certain materials that are somehow related to the materials studied in this thesis.

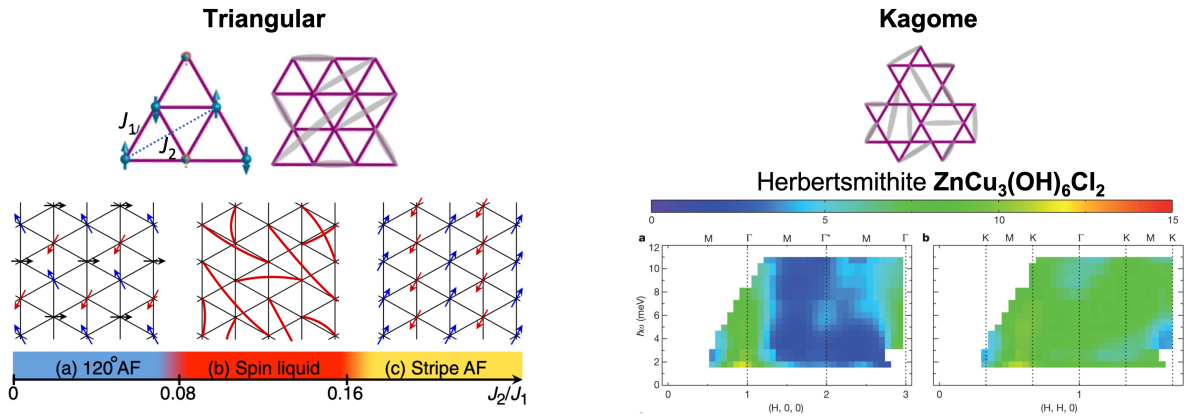
A historically significant model in the pursuit of the quantum spin liquid (QSL) ground state is a one-dimensional chain of antiferromagnetically (AFM) coupled isotropic or Heisenberg $S = 1/2$ moments. One of the textbook examples of such material is KCuF_3 [7]. The dynamical structure factor in zero field (Fig.1.1 *right*) does not correspond to the classical spin-wave picture with magnons, as elementary excitations (Fig.1.1 *left*). In fact, there is a continuum, which arises due to fractionalized excitations, called spinons. Each of the spinons carries spin-1/2 and freely propagates along the chain with no energy loss. Since each spinon has its own energy-momentum relation, the spectra appear continuous. This model was solved exactly by Bethe [8] in 1931, who predicted a spin-pair correlations to be proportional to a power law: $\langle \mathbf{S}(0) \cdot \mathbf{S}(r) \rangle_{t=0} \propto \frac{(-1)^r}{r}$.

If for one-dimensional case there is an exact analytical solution, situation changes drastically for higher dimensions. And one of the key ingredients to observe a QSL state in higher dimensions is frustration. To represent the ground state of antiferromagnetically interacting spins on the two-dimensional triangular lattice, P. W. Anderson proposed a resonating valence bond (RVB) model [9], in which any two antiparallel spins pair up to form a spin singlet, with a total spin $S = 0$ and vanishing net magnetic moment. There is no particular arrangement of these singlets and the wavefunction of this state is a linear superposition of all possible configurations of the singlets (Fig.1.2). This state was termed as quantum spin liquid QSL and characterized by the following features: absence of long-range magnetic order, no spontaneous symmetry breaking of the crystal lattice or spins, long-range entanglement between the spins, and fractional


FIGURE 1.1

Left: Classical antiferromagnetic magnon dispersion calculated for $J = 1$ meV; *right:* dynamical structure factor of KCuF_3 measured at $T = 6$ K (adapted from [7]).

spin excitations. Later on, it has been shown [10] that there is a classical solution to avoid such a geometrically frustrated configuration on the triangular lattice – each spin on a triangle points to 120° with respect to each other resulting to a ground state with the 120° long-range magnetic order [5]. However, if one includes further neighbor interactions, in a certain regions of $J_1 - J_2$ ratios, QSL state is yet a ground state of the system. For the kagome lattice, geometrical frustration cannot be bypassed by having the 120° order as does the triangular lattice. Theoretical calculations suggest that the ground state for the kagome lattice is a QSL, although the detailed classification for such a state is still under hot debate. One of the remarkable examples is herbertsmithite [11], where the diffuse magnetic scattering was observed in the inelastic spectra and in which this signal was attributed to multi-spinon continua.


FIGURE 1.2

Left: Triangular lattice (adapted from [5]) and its $J_1 - J_2$ phase diagram (adapted from [12]); *right:* Kagome lattice (adapted from [5]) and magnetic excitations of herbertsmithite (adapted from [11]).

In three-dimensional (3D) spin systems, the fractionalisation is also possible. One of the well-explored examples are pyrochlore compounds which consists of a three-dimensional network

of corner-sharing tetrahedra. The pyrochlore lattice can support the spin ice state which arises from the combination of strong local Ising anisotropy and ferromagnetic interactions as was found in $\text{Ho}_2\text{Ti}_2\text{O}_7$ [13]. Spin ice is characterized by a macroscopic ground state degeneracy and fractional monopole excitations. Those states only exist for large local moments and/or very strong local anisotropies. In comparison to the pyrochlore compounds, current understanding of three-dimensional networks of corner-sharing triangles, such as the hyperkagome lattice, is much less developed, despite the fact that they are expected to support spin liquid behavior in the presence of isotropic antiferromagnetic interactions [14]. One of the physical realisations of the hyperkagome lattice is $\text{PbCuTe}_2\text{O}_6$, which has quantum $S = 1/2$ ions and is proximate to a quantum spin liquid [15].

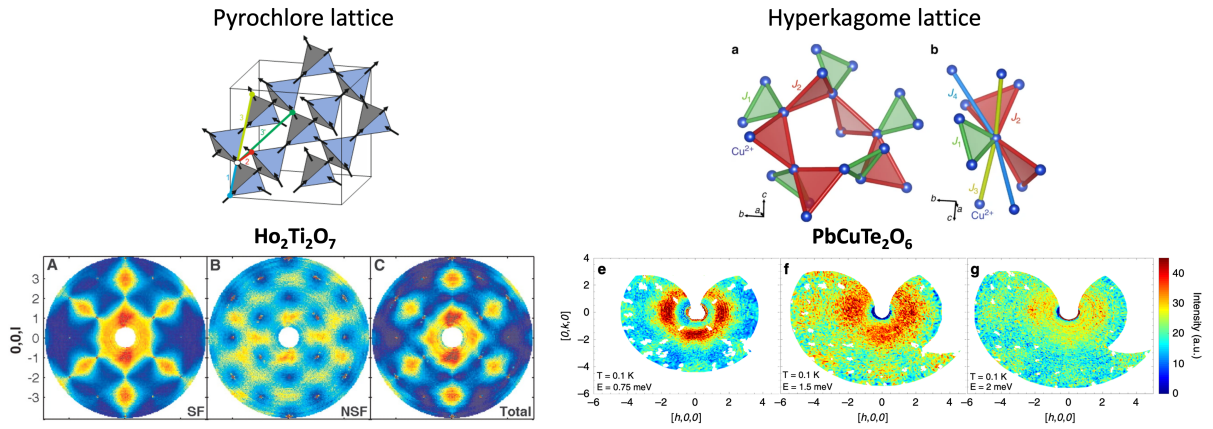


FIGURE 1.3

Left: Pyrochlore lattice (adapted from [16]) and the scattering function $S(\mathbf{Q})$ of $\text{Ho}_2\text{Ti}_2\text{O}_7$ [13]; *right:* hyperkagome lattice and single crystal inelastic spectra of $\text{PbCuTe}_2\text{O}_6$ measured at constant energy transfer [15].

In the current thesis, three materials with spinon-like excitations will be presented – starting from its experimental evidence in a quasi-one-dimensional system and two (three)-dimensional frustrated triangular system and ending with the evolution of spinon-continuum in applied magnetic field. The chapters are organized as follows.

Chapter 2 reviews the methods, which were used during the current thesis. Most of it is devoted to the description of the neutron scattering technique since it is the main and most powerful method for studying quantum magnets.

Chapter 3 presents a very accurate study of the best-known realization of one-dimensional Heisenberg $S = 1/2$ antiferromagnet $\text{CuSO}_4 \cdot 5\text{D}_2\text{O}$ in the applied magnetic field below saturation. The new quasiparticles, which govern the spectrum in applied magnetic field, behave like spinons in low applied magnetic field and demonstrate magnon-like bound states close to the saturation.

Chapter 4 demonstrates the evidence of quantum fluctuations of spinon-like character in very contradicting quasi-one-dimensional material $\text{Cu}_6[\text{Si}_6\text{O}_{18}] \cdot 6\text{H}_2\text{O}$. With polarization analysis, we extracted pure magnetic scattering and observed continuum-like scattering below and above T_N .

Chapter 5 is a comprehensive research of a new potential quantum spin liquid candidate CuSb_2O_6 . The sample is available only in powder, thus we have used other experimental techniques besides neutron scattering for its characterization. The experimental findings so far indicate a highly frustrated (including frustration in triangular motifs) magnetic system with no evidence of long-range magnetic order, which is probably three-dimensional realization of a quantum spin liquid.

CHAPTER 2

METHODS

In this chapter, I will provide a reader with the experimental techniques used during the current thesis. The idea of this chapter is not to rewrite Squires [17], Lovesey [18], or other (e.g. [19]) excellent books but to highlight the main principles and equations, which are essential to understand during the data analysis.

2.1 NEUTRON SCATTERING

Neutron scattering is a very powerful technique to study condensed matter and, especially magnetism. This is primarily due to the peculiarities of the interaction of a neutron with matter. Neutron probes the whole volume of the sample and generally scatters only once within the sample. The scattering process can be described with the so-called Master equation, where scattering cross-section is defined as

$$\frac{d^2\sigma}{d\Omega dE_f} = \frac{k_f}{k_i} \left(\frac{m}{2\pi\hbar^2} \right)^2 \sum_{\sigma_i, \sigma_f, n_0, n_1} p(\sigma_i) p(n_0) |\langle k_f \sigma_f n_1 | V | k_i \sigma_i n_0 \rangle|^2 \delta(\epsilon_1 - \epsilon_0 - \hbar\omega), \quad (2.1)$$

where $d\Omega$ is a solid angle of the neutron scattered; dE_f is a final energy interval, which is captured by the detector; k_i, k_f are initial and final wave vector of a neutron; m is a neutron mass; σ_i, σ_f are initial and final neutron spin state; n_0, n_1 are quantum number for the sample's initial and final state; ϵ_0, ϵ_1 are initial and final sample energy; E_i, E_f are initial and final energy of a neutron; $E_i - E_f = \hbar\omega$ is an energy transfer; V is an interaction potential between sample and neutron; $p(n_0)$ is a probability to find a sample in the initial state n_0 ; $p(\sigma_i)$ is a probability to find neutron in the initial spin state σ_i .

2.1.1 NUCLEAR SCATTERING

Neutron interacts with a nucleus, which leads to an isotropic nuclear scattering characterized by a scattering length b . The scattering length depends on the isotope, the nuclear spin value, and the total spin of neutron and nucleus. Coherent scattering is the result of the interference of scattered neutrons from different crystallographic sites. It manifests itself in the form of Bragg reflections or phonons, while incoherent scattering appears due to the fluctuations of the scattering length from the mean value \bar{b} on each site $\sqrt{(\bar{b}^2) - (\bar{b})^2}$. For monoatomic sample, the cross-sections can be read as

$$\left(\frac{d^2\sigma}{d\Omega dE_f} \right)_{coh} = \frac{k_f}{k_i} \frac{\bar{b}^2}{2\pi\hbar} \sum_{ij} \int_{-\infty}^{+\infty} \langle e^{i\mathbf{Q}[\mathbf{r}_j(t) - \mathbf{r}_i(0)]} \rangle e^{-i\omega t} dt \quad (2.2)$$

$$\left(\frac{d^2\sigma}{d\Omega dE_f} \right)_{incoh} = \frac{k_f}{k_i} \frac{(\bar{b}^2) - (\bar{b})^2}{2\pi\hbar} \sum_i \int_{-\infty}^{+\infty} \langle e^{i\mathbf{Q}[\mathbf{r}_i(t) - \mathbf{r}_i(0)]} \rangle e^{-i\omega t} dt, \quad (2.3)$$

where $e^{i\mathbf{Q}\mathbf{r}_i(t)}$ reflects the definition of an interaction by Fermi pseudopotential, \mathbf{Q} is momentum transfer and \mathbf{r} stands for nucleus position in the unit cell.

It is worth mentioning here the link of a double differential cross-section with a so-called scattering function or dynamical structure factor $S(\mathbf{Q}, \omega)$ as follows:

$$\frac{d^2\sigma}{d\Omega dE_f} = \frac{k_f}{k_i} \bar{b}^2 S(\mathbf{Q}, \omega). \quad (2.4)$$

In this equation, the dynamical structure factor multiplied with \bar{b}^2 reflects the properties of the sample. The momentum transfer dependence indicates the atomic positions, whereas energy dependence expresses the motion of atoms. Thus, neutrons allow us to study where the atoms are and how they move. Moreover, the double differential cross-section is the entry measured during the neutron experiment.

2.1.2 MAGNETIC SCATTERING

Since the neutron has a spin $S = 1/2$ and hence a magnetic moment, it probes the electronic magnetic moment of a sample via dipole-dipole interaction, which is as strong as the interaction with the nuclei, so that makes neutron a powerful instrument to study magnetism. However, the magnetic scattering is no longer isotropic – one observes only magnetic moments (and/or its fluctuations), which are perpendicular to the momentum transfer \mathbf{Q} . Similarly to Eq.2.4, the double-differential cross-section for magnetic scattering is given by:

$$\left(\frac{d^2\sigma}{d\Omega dE_f} \right)_{mag} = \frac{k_f}{k_i} (\gamma r_0)^2 S_{mag}(\mathbf{Q}, \omega), \quad (2.5)$$

where (γr_0) is a strength of dipole-dipole interaction between the neutron and electronic spins, and $S_{mag}(\mathbf{Q}, \omega)$ reveals the information about the structure and movement of electronic spins, so that describes the magnetic correlations of the system in space and in time.

Considering that the neutron senses only perpendicular projection of the magnetic moments, one rewrites Eq.2.5 as:

$$\left(\frac{d^2\sigma}{d\Omega dE_f} \right)_{mag} = \frac{k_f}{k_i} (\gamma r_0)^2 \left(\frac{gf(\mathbf{Q})}{2} \right)^2 e^{-2W(\mathbf{Q})} \sum_{\alpha\beta} \left(\delta_{\alpha\beta} - \hat{Q}_\alpha \hat{Q}_\beta \right) S_{mag}^{\alpha\beta}(\mathbf{Q}, \omega), \quad (2.6)$$

where $f(\mathbf{Q})$ is a magnetic form-factor for a given magnetic atom, g is a gyromagnetic ratio, $e^{-2W(\mathbf{Q})}$ is a Debye-Waller factor, which reflects the nuclei motion, $\left(\delta_{\alpha\beta} - \hat{Q}_\alpha \hat{Q}_\beta \right)$ is a dipole factor expressing perpendicular projection of a magnetic moment, so that $|\mathbf{M}_{\perp\mathbf{Q}}| = \hat{\mathbf{Q}} \times (\mathbf{M}(\mathbf{Q}) \times \hat{\mathbf{Q}})$, in which $\mathbf{M}(\mathbf{Q})$ is a Fourier transform of the sample magnetization $\mathbf{M}(\mathbf{r})$. The dynamical structure factor $S^{\alpha\beta}(\mathbf{Q}, \omega)$ is defined as

$$S_{mag}^{\alpha\beta}(\mathbf{Q}, \omega) = \frac{1}{2\pi\hbar} \sum_{ij} e^{-i\mathbf{Q}(\mathbf{r}_i - \mathbf{r}_j)} \int_{-\infty}^{+\infty} dt e^{-i\omega t} \langle S_i^\alpha(t) S_j^\beta(0) \rangle, \quad (2.7)$$

where $\langle S_i^\alpha(t) S_j^\beta(0) \rangle$ reveals spin-spin correlations present in the sample.

To eliminate a trivial temperature dependence of the excitations population in $S(\mathbf{Q}, \omega)$, it is worthwhile to analyze the dynamic susceptibility $\chi(\mathbf{Q}, \omega)$, which imaginary part $\chi''(\mathbf{Q}, \omega)$, is related to $S(\mathbf{Q}, \omega)$ as

$$S(\mathbf{Q}, \omega) = -\frac{1}{\pi} \frac{1}{1 - e^{-\hbar\omega/k_B T}} \chi''(\mathbf{Q}, \omega). \quad (2.8)$$

Thus, in the observed temperature dependence of $\chi''(\mathbf{Q}, \omega)$ one can conclude of underlying physics.

2.1.3 NEUTRON TECHNIQUES AND INSTRUMENTATION

NEUTRON DIFFRACTION

To obtain information of a crystal (magnetic if any) structure, one can perform neutron diffraction experiments. On diffraction instruments, the final energy E_f is not analyzed, so that we obtain

integrated by energy scattering function $S(\mathbf{Q}) = \int_{-\infty}^{+\infty} S(\mathbf{Q}, \omega) d\omega$. This is valid if the incident neutron energy E_i is much higher than all excited states in the sample.

The principle of neutron diffraction is based on the Bragg's law:

$$2d \sin \Theta = n\lambda, \quad (2.9)$$

where d is an interplanar spacing, Θ is a scattering angle, n is an order of diffraction (integer), and λ is a neutron wavelength. Therefore, the cross-section for nuclear elastic coherent scattering is:

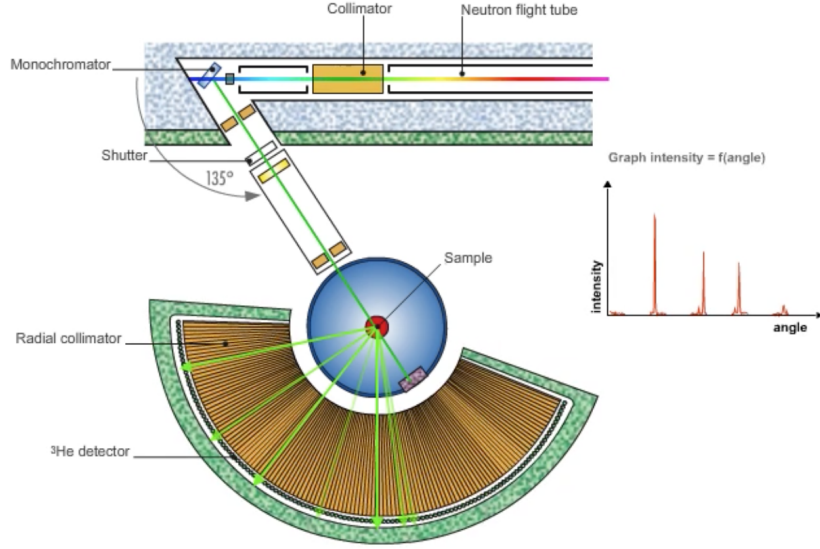
$$\left(\frac{d\sigma}{d\Omega} \right)_{nuc}^{el} = N \frac{(2\pi)^3}{V} \sum_{\tau} \delta(\mathbf{Q} - \tau) |F_N(\mathbf{Q})|^2, \quad (2.10)$$

where $F_N(\mathbf{Q}) = \sum_d b_d e^{i\mathbf{Q} \cdot \mathbf{d}} e^{-W_d(\mathbf{Q})}$ is a nuclear structure factor, $\tau = \mathbf{k}_i - \mathbf{k}_f$. As can be seen from Eq.2.10, the delta function explicitly displays the appearance of a peak at $\mathbf{Q} = \tau$, which reflects Bragg's law 2.9. In fact, what we get from the experiment is a delta function but convoluted with instrument resolution and broadening due to the microstructural effects in the sample so that the intensity of a measured peak would have a finite value. Since each peak has its own width, position, and intensity, each parameter gives the following information about the sample: symmetry and lattice dimensions are "stored" in the peak position, location of atoms inside the unit cell – in the intensity, and width of the peak reflects Debye-Waller factor together with instrument resolution and possible microstructural effects. Neutron diffraction can be successfully used for the magnetic structure determination, and for elastic magnetic scattering, we have:

$$\left(\frac{d\sigma}{d\Omega} \right)_{mag}^{el} = (\gamma r_0)^2 N_m \frac{(2\pi)^3}{V} \sum_{\tau_m} \delta(\mathbf{Q} - \tau_m) |\hat{\mathbf{Q}} \times (\mathbf{F}_M(\mathbf{Q}) \times \hat{\mathbf{Q}})|^2, \quad (2.11)$$

where in analogy to elastic nuclear scattering $\mathbf{F}_M(\mathbf{Q}) = \sum_i \left(\frac{g_i f_i(\mathbf{Q})}{2} \right) \langle \mathbf{S}_i \rangle e^{i\mathbf{Q} \cdot \mathbf{r}_i} e^{-W_i(\mathbf{Q})}$ is a magnetic structure factor. In this case, magnetic Bragg peaks will be found at new positions $\mathbf{Q} = \tau_m$ in reciprocal space.

Depending on the studied material type (single crystal or powder sample), different types of instruments were used. The principle of the experiment remains the same, while the technical environment is different. In the thesis, for the investigation of a powder sample crystal structure, CuSb₂O₆, D2B@ILL (Fig.2.1), and D4@ILL were used. The profile analysis of the obtained diffraction pattern was done by the Rietveld method [20] implemented in Fullprof [21].


FIGURE 2.1

Layout of a D2B instrument. The wavelength of neutrons $\lambda = 1.594 \text{ \AA}$ is selected by Ge(335) monochromator. A bank of 128 detectors allows to capture the Bragg reflections in the angular range of about 4° to 160° [22].

POLARIZED NEUTRON DIFFRACTION

Using polarized neutrons, one can separate different contributions like nuclear coherent, magnetic coherent, and incoherent scattering to the total scattering according to their structural or magnetic origin [23]. By analyzing the polarization of incoming \mathbf{P}_i and outgoing \mathbf{P}_f neutron beams, Blume [24] and Maleev [25] define the general cross-section for polarized neutrons as

$$\frac{d\sigma}{d\Omega} = N^*N + \mathbf{M}_\perp^* \mathbf{M}_\perp + N^*[\mathbf{P}_i \cdot \mathbf{M}_\perp] + N[\mathbf{P}_i \cdot \mathbf{M}_\perp^*] + i\mathbf{P}_i[\mathbf{M}_\perp^* \times \mathbf{M}_\perp] + \nu_i + \sigma_{nsi} \quad (2.12)$$

and

$$\begin{aligned} \mathbf{P}_f \frac{d\sigma}{d\Omega} = & \mathbf{P}_i(N^*N + \nu_i) - \mathbf{P}_i \mathbf{M}_\perp^* \mathbf{M}_\perp - \frac{1}{3} \mathbf{P}_i \sigma_{nsi} + \mathbf{M}_\perp[\mathbf{P}_i \cdot \mathbf{M}_\perp^*] + \mathbf{M}_\perp^*[\mathbf{P}_i \cdot \mathbf{M}_\perp] - \\ & - i\mathbf{M}_\perp^* \times \mathbf{M}_\perp + N^* \mathbf{M}_\perp + N \mathbf{M}_\perp^* - iN^*[\mathbf{P}_i \times \mathbf{M}_\perp] + iN[\mathbf{P}_i \times \mathbf{M}_\perp^*], \end{aligned} \quad (2.13)$$

where N is a nuclear scattering, \mathbf{M}_\perp is a magnetic scattering, σ_{nsi} is a nuclear spin incoherent scattering, ν_i is a nuclear isotope incoherent scattering. The first equation is the cross-section for an incoming polarized beam without polarization analysis after the sample, whereas the second

equation leads to a measurable cross-section when projected on a final polarization direction. In the following, we define a right-handed coordinate system linked to \mathbf{Q} and the scattering plane with $\hat{\mathbf{x}} \parallel \mathbf{Q}$, $\hat{\mathbf{y}} \perp \mathbf{Q}$ in the scattering plane, $\hat{\mathbf{z}} \perp \mathbf{Q}$ perpendicular to the scattering plane.

With spherical neutron polarimetry, the polarization tensor could be measured:

$$P = \begin{pmatrix} P_{xx} & P_{xy} & P_{xz} \\ P_{yx} & P_{yy} & P_{yz} \\ P_{zx} & P_{zy} & P_{zz} \end{pmatrix},$$

where $P_{\alpha\beta} = \frac{\sigma_{\alpha\beta} - \sigma_{\alpha\bar{\beta}}}{\sigma_{\alpha\beta} + \sigma_{\alpha\bar{\beta}}}$. Such matrices could be measured with Cryogenic Polarization Analysis Device (CRYOPAD) [26].

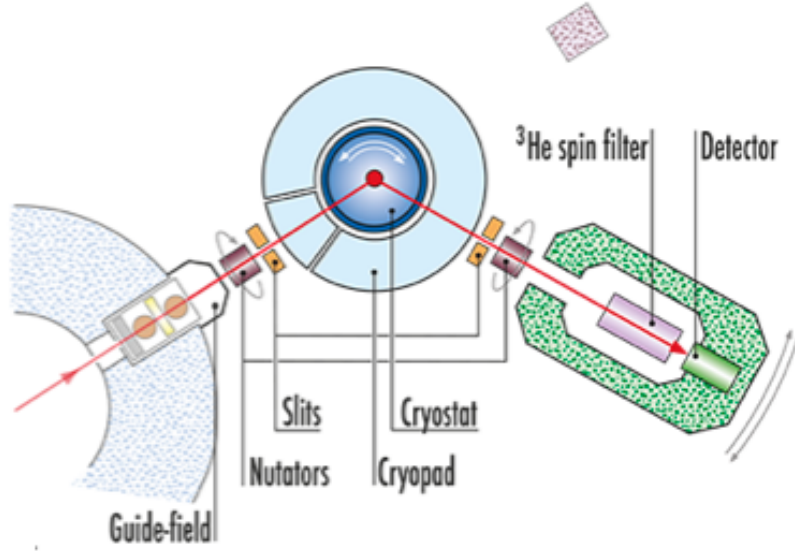


FIGURE 2.2

Layout of a D3@ILL instrument adapted from [27].

We used a single crystal diffractometer D3@ILL (Fig.2.2) for magnetic structure determination of $\text{Cu}_6[\text{Si}_6\text{O}_{18}] \cdot 6\text{H}_2\text{O}$. Polarized neutrons with wavelength $\lambda = 0.85 \text{ \AA}$ are created by Heusler(111) monochromator. The final neutron polarization is analyzed with ^3He spin filter, whose efficiency is usually tested by measuring one of the polarization channels of the strong nuclear Bragg reflection. The sample was mounted into an Orange Cryostat at base temperature $T = 1.5 \text{ K}$. In addition, a CRYOPAD device hosted CryoCradle [28], allowing access to out-of-plane Bragg reflections.

TRIPLE-AXIS SPECTROSCOPY

For single crystal inelastic scattering studies, triple-axis spectrometers (TAS) are often used allowing point-by-point measurements at particular \mathbf{Q} and ω values (Fig.2.3). The incoming energy of neutrons E_i is selected by a monochromator, which is usually a Bragg reflection of a well-defined crystal. Then neutrons scatter at the sample position, and the analyzer captures only those at the specific final energy E_f . The measurement of excitations therefore can be described as:

$$\mathbf{Q} = \mathbf{k}_i - \mathbf{k}_f = \boldsymbol{\tau} + \mathbf{q}, \quad (2.14)$$

$$\hbar\omega = \frac{\hbar^2}{2m_n}(k_i^2 - k_f^2) = \hbar\omega(\mathbf{q}), \quad (2.15)$$

where $\hbar\omega(\mathbf{q})$ is the energy of the measured excitation at specific wave-vector \mathbf{q} .

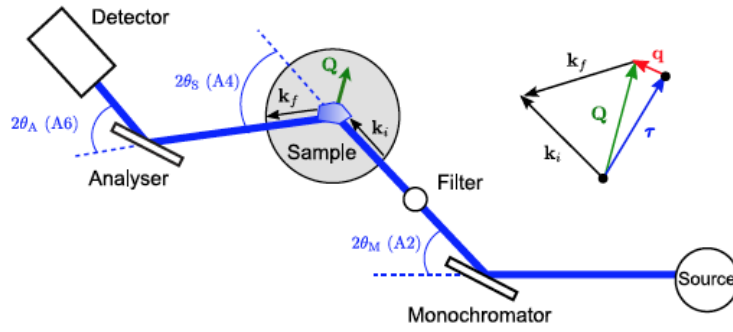


FIGURE 2.3
Layout of a triple-axis instrument adapted from [29].

XYZ POLARIZATION ANALYSIS

One of the huge TAS advantages is the possibility to polarize the incoming neutron beam and also to analyze the polarization of the outgoing beam. In the case of XYZ polarization analysis, which can be performed using Helmholtz coils, with a spin-flipper in k_f the following cross-sections

are defined:

$$\begin{aligned}
 \left. \frac{d^2\sigma}{d\Omega dE_f} \right|_{x \rightarrow x} &\propto \mathcal{N} + \frac{1}{3}\sigma_{si} \\
 \left. \frac{d^2\sigma}{d\Omega dE_f} \right|_{x \rightarrow \bar{x}} &\propto \mathcal{M}_y + \mathcal{M}_z - 2\mathcal{C} + \frac{2}{3}\sigma_{nsi} \\
 \left. \frac{d^2\sigma}{d\Omega dE_f} \right|_{y \rightarrow y} &\propto \mathcal{N} + \mathcal{M}_y + \frac{1}{3}\sigma_{nsi} \\
 \left. \frac{d^2\sigma}{d\Omega dE_f} \right|_{y \rightarrow \bar{y}} &\propto \mathcal{M}_z + \frac{2}{3}\sigma_{nsi} \\
 \left. \frac{d^2\sigma}{d\Omega dE_f} \right|_{z \rightarrow z} &\propto \mathcal{N} + \mathcal{M}_z + \frac{1}{3}\sigma_{nsi} \\
 \left. \frac{d^2\sigma}{d\Omega dE_f} \right|_{z \rightarrow \bar{z}} &\propto \mathcal{M}_y + \frac{2}{3}\sigma_{nsi},
 \end{aligned} \tag{2.16}$$

where $|\alpha \rightarrow \beta$ defines the initial polarization direction α and analyzed outgoing polarization β , and

$$\begin{aligned}
 \mathcal{N} &= \int_{-\infty}^{+\infty} e^{-i\omega t} dt \langle N^*(\mathbf{Q}, 0) N(\mathbf{Q}, t) \rangle_T, \\
 \mathcal{M}_{y(z)} &= \int_{-\infty}^{+\infty} e^{-i\omega t} dt \langle M_{\perp y(z)}^*(\mathbf{Q}, 0) \langle M_{\perp y(z)}(\mathbf{Q}, t) \rangle_T, \\
 \mathcal{C} &= -\frac{i}{2} \int_{-\infty}^{+\infty} e^{-i\omega t} dt \cdot \langle \mathbf{M}_{\perp \mathbf{Q}}^* \times \mathbf{M}_{\perp \mathbf{Q}} \rangle_T
 \end{aligned}$$

reflect nuclear correlations, distinguishable (allocated) magnetic, and chiral scattering correlations respectively.

In current thesis, the results of several triple-axis experiments are presented, the details of which can be found in the table below Tab.2.1.

Instrument	Material	Magnetic field	Cross-sections	Monochromator	Analyzer	Fixed
IN14	$\text{CuSO}_4 \cdot 5\text{D}_2\text{O}$	$\mathbf{H} \perp \mathbf{Q}$	$\bar{z}z, zz$	PG(002)+bender	Heusler(111)	$k_f = 1.075 \text{ \AA}^{-1}$
IN14	$\text{CuSO}_4 \cdot 5\text{D}_2\text{O}$	$\mathbf{H} \parallel \mathbf{Q}$	$x0, \bar{x}0$	Heusler(111)	–	$k_f = 1.075 \text{ \AA}^{-1}$
ThALES	$\text{Cu}_6[\text{Si}_6\text{O}_{18}] \cdot 6\text{H}_2\text{O}$	–	XYZ	Heusler(111)	Heusler(111)	$k_f = 1.5 \text{ \AA}^{-1}$
IN20	$\text{Cu}_6[\text{Si}_6\text{O}_{18}] \cdot 6\text{H}_2\text{O}$	–	XYZ	Heusler(111)	Heusler(111)	$k_f = 2.662 \text{ \AA}^{-1}$

TABLE 2.1
List of TAS experiments and their details.

TIME-OF-FLIGHT SPECTROSCOPY

Time-of-flight (TOF) technique allows to perform all measurements simultaneously over a broad range in (Q, ω) space, unlike triple-axis spectrometers. IN5@ILL (Fig.2.4) belongs to the direct geometry multi-chopper instruments, in which the wavelength (hence, E_i) is selected by choppers, and scattered neutrons with different final energy E_f are collected by huge detector arrays covering 30 m^2 . Multi-chopper system allows to control and optimize the resolution function with very high precision [30] and, hence, grants a superior resolution of the order of several μeV . Contrary to TAS, the time-of-flight technique is adapted not only for single crystal studies but also for powder samples.

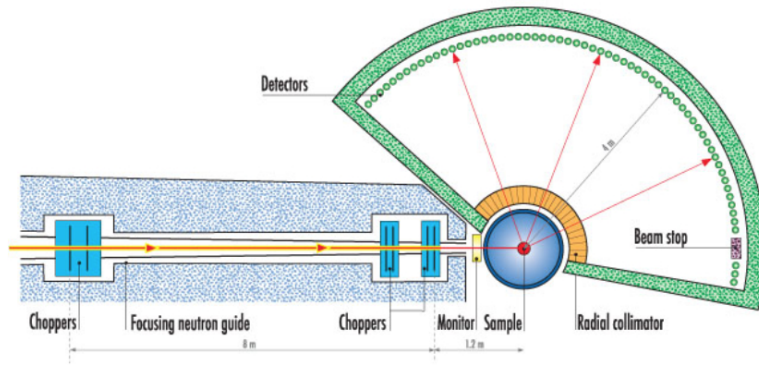


FIGURE 2.4

Layout of IN5@ILL time-of-flight instrument adapted from [31].

To have an overview of the magnetic excitations in powder CuSb_2O_6 sample, in addition to Cryostat measurements at IN5@ILL, we have performed LET@ISIS experiment with dilution insert. Since the Repetition Rate Multiplication method [32] is implemented in LET, neutrons with four different incident energies were able to pass through the chopper system, and therefore, we obtained four different data sets simultaneously. The list of performed time-of-flight experiments and their details are shown in Tab.2.2.

Instrument	Material	Temperature (K)	Incoming energy (meV)	Environment
IN5	$\text{CuSO}_4 \cdot 5\text{D}_2\text{O}$	0.075	$E_i = 2.27$	Vertical cryomagnet , dilution fridge
IN5	CuSb_2O_6	[1.6..100]	$E_i = 3.55, 12.1$	Orange Cryostat
LET	CuSb_2O_6	[0.06..1.7]	$E_i = 1.03, 1.77, 3.7, 12.14$	Dilution fridge

TABLE 2.2

List of TOF experiments and their details.

2.2 LINEAR SPIN-WAVE THEORY

Linear spin wave theory LSWT is indeed a subject of Chapter 4, where the magnetic excitations are studied below T_N . The main goal of these calculations is to obtain the energy-momentum relation of spin waves, which are elementary excitations in the magnetically ordered state. The method is realized in SpinW [33]. As an input, it requires a definition of the spin Hamiltonian and the magnetic structure, which represents the ground state of this Hamiltonian. Through Holstein-Primakoff [34] transformation, spin operators are then represented as bosonic annihilation a^\dagger and creation a operators, therefore reconstructing the Hamiltonian as a series expansion in powers of a^\dagger and a . Linear in LSWT means that only the terms linear to $a^\dagger a$ will be taken into account reflecting non-interacting magnons. Following Fourier transformation of the bosonic terms allows to obtain momentum transfer dependence of the Hamiltonian, diagonalization of which will finally give the magnon energies and spin-spin correlation functions, and hence the neutron scattering cross-section can be obtained.

2.3 REVERSE MONTE CARLO

When one deals with the paramagnetic state of the sample, characterized by short-range spin correlations and absence of long-range magnetic order (LRMO), spin-wave theory is no longer valid. Moreover, the task becomes more difficult when the sample is in powder form, and we cannot measure certain directions with inelastic neutron scattering to trace the dynamics. One of the methods that could be used for diffuse scattering study in powder samples is Reverse Monte Carlo (RMC). Contrary to direct Monte Carlo, the function which is minimised during the refinement is not an energy term defined by a spin Hamiltonian, but rather the sum of squared residuals that quantifies the level of disagreement between the fit and experimental data. Therefore, RMC based on the experimental data will provide information on spin pair correlations $\langle \mathbf{S}(0) \cdot \mathbf{S}(r) \rangle$, not interactions J_i .

This method is realized in SPINVERT [35]. It is based on a step-by-step application of the least squares approximation, where at each step the neutron scattering cross section $S(\mathbf{Q})$ for a given spin configuration $\langle \mathbf{S}(0) \cdot \mathbf{S}(r) \rangle$ is calculated, compared with experimental data. Then the initial configuration is transformed in order to minimize the discrepancy between the experiment and the model curve. For a powder isotropic paramagnet, magnetic scattering function integrated along ω takes the form:

$$S(Q) \propto \frac{2}{3} \left| \frac{g}{2} f(\mathbf{Q}) \right|^2 \left(1 + \frac{1}{N} \sum_{i,j} \mathbf{S}_i \cdot \mathbf{S}_j \frac{\sin Qr_{ij}}{Qr_{ij}} \right), \quad (2.17)$$

where $\langle \mathbf{S}(0) \cdot \mathbf{S}(r) \rangle = \sum_i^N \frac{1}{Z_{ij}(r)} \sum_j^{Z_{ij}(r)} \mathbf{S}_i \cdot \mathbf{S}_j$.

2.4 MAGNETIC SUSCEPTIBILITY

Magnetic susceptibility measurements determine the averaged value of the magnetization in a sample. The sample is magnetized by a constant magnetic field and the magnetic moment is measured, producing a magnetization curve $M(H)$. The slope of the $M(H)$ is called the susceptibility $\chi = dM/dH$. At high temperatures, the magnetic susceptibility is approximated by Curie-Weiss law [36]:

$$\chi(T) = \chi_0 + \frac{C}{T - \Theta_{CW}}, \quad (2.18)$$

where χ_0 is a temperature-independent term, C – Curie constant, from which one can obtain the value of the effective magnetic moment

$$C = \frac{N_A}{3k_B} \mu_{eff}^2,$$

Θ_{CW} [36] is a Curie-Weiss temperature, which is basically a sum of all interactions present in the system [36]

$$\Theta_{CW} = \sum_i \frac{z_i S(S+1) J_i}{3k_B},$$

and therefore with its sign one can conclude of dominant interactions in the system.

This technique is widely used for single crystal and powder samples as a quick examination of presence or absence of magnetic ordering.

2.5 SPECIFIC HEAT

Specific heat C is the most direct measure of fluctuations in any system. In a simplistic approximation, $C = C_{ph} + C_e + C_m$, where C_{ph} – lattice contribution, C_e – electronic contribution and C_m – magnetic contribution [37]. At low temperatures, where the systems are assumed to be in a thermal equilibrium, only magnetic fluctuations give rise to a magnetic specific heat contribution C_m . At critical temperature e.g. T_N , one can observe λ -anomaly, usually associated with LRMO. At higher temperatures, lattice fluctuations become significant, and they need to be removed in order to estimate the magnetic part of the specific heat. For that purpose, it is always a good practice to prepare a non-magnetic analog of the studied magnetic material. Whenever it is impossible, one has to simulate a lattice contribution, for example, using Debye and/or Einstein models. Change of magnetic contribution ΔC_m is linked to a change of the magnetic

entropy as:

$$\Delta S_m(T) = \int_0^T \frac{C_m(T)}{T} dT, \quad (2.19)$$

which reflects how much of the magnetic entropy is involved into a phase transition (if any).

Similar to susceptibility, specific heat measurements can be performed on single crystal and powder samples.

2.6 MUON SPECTROSCOPY

Complementary to mentioned above macroscopic methods, muons are an effective probe of local magnetic fields present in the sample and their dynamics. The implemented muons are very sensitive to any spin freezing and long-range magnetic order induced by magnetic atoms and hence can reveal a question of static magnetic moments present in the system.

We have performed a muon relaxation experiment in zero field. The goal of such experiment is to observe time evolution of muon polarization caused by randomly oriented local fields in the sample. This technique was developed by Kubo and Toyabe [38], who initially assumed a system of spins with the Gaussian distribution of field strengths, which describes the magnetic environment, thus the polarization function takes the form:

$$G_z^{GKT}(t) = \frac{1}{3} + \frac{2}{3} (1 - \sigma^2 t^2) \exp\left(-\frac{\sigma^2 t^2}{2}\right), \quad (2.20)$$

where $\sigma = \gamma_\mu \Delta$ is the relaxation rate. In Eq.2.20, $\frac{1}{3}$ and $\frac{2}{3}$ components arise from the fact that the local field is random in all directions so that $\approx \frac{1}{3}$ is parallel or antiparallel to the initial muon spin direction and $\approx \frac{2}{3}$ is perpendicular. Such muon response is often attributed to nuclear static fields [39]. Nuclear moments are weak and thus can be regarded static on the μ SR time window. In the paramagnetic state of systems, the electronic moments are fluctuating much too fast to have an effect on the μ SR signal and the muon spin will solely sense the field distribution created by the nucleus moments. As these are randomly oriented, they will create a weak Kubo-Toyabe depolarization of the muon ensemble and the minimum of the function will not always be visible in the data [40].

CHAPTER 3

FIELD-DEPENDENT DYNAMICS IN $\text{CuSO}_4 \cdot 5\text{D}_2\text{O}$

3.1 QUANTUM SPIN-1/2 ANTIFERROMAGNETIC SPIN CHAINS IN ZERO AND NON-ZERO MAGNETIC FIELD

In this section, we review theoretical and experimental studies related to the dynamics of quantum spin-1/2 antiferromagnetic linear spin chains, although limiting ourselves to those scientific discoveries that somehow influenced the following study of our material.

The history of 1D magnetism starts with Ising's consideration of infinite spin chain with nearest-neighbor AFM interactions in 1925 [41]. The Hamiltonian for this case is the following:

$$H = J \sum_i S_i^\alpha S_{i+1}^\alpha,$$

where J – intrachain AFM interaction between the neighboring spins, S_i^α – z -component of the spin \vec{S}_i on the site i for the Ising case. He has reported that there is no spontaneous magnetization occurs at any finite temperature. Whereas for $S = 1/2$ chain at $T = 0$ K Ising model suggests an ordered state, in the isotropic Heisenberg ($\alpha = x, y, z$) model, this chain remains disordered even at $T = 0$ K.

Almost century ago, in 1931, Bethe [8] provided an ansatz to find the exact eigenvalues and eigenvectors of the spin-1/2 Heisenberg Hamiltonian with antiferromagnetic nearest-neighbor interactions. At zero temperature $T = 0$ K, a ground state is a many-body spin singlet $S_{tot} = 0$ with power-law decaying spin correlations $\langle S_0^\alpha \cdot S_r^\alpha \rangle = \frac{(-1)^r}{r}$ [42] and can be mapped onto Tomonaga-Luttinger liquid (TLL). The excitation spectrum is gapless and composed of free

spinon pairs. Each spinon with spin-1/2 propagates freely along the chain and has its own energy-momentum relation making the spectrum appear continuous. The dispersion relations for the upper and lower boundaries are given by:

$$\omega_{low}(k) = \frac{\pi J}{2} |\sin(k)|, \quad (3.1)$$

$$\omega_{up}(k) = \pi J |\sin(k/2)|. \quad (3.2)$$

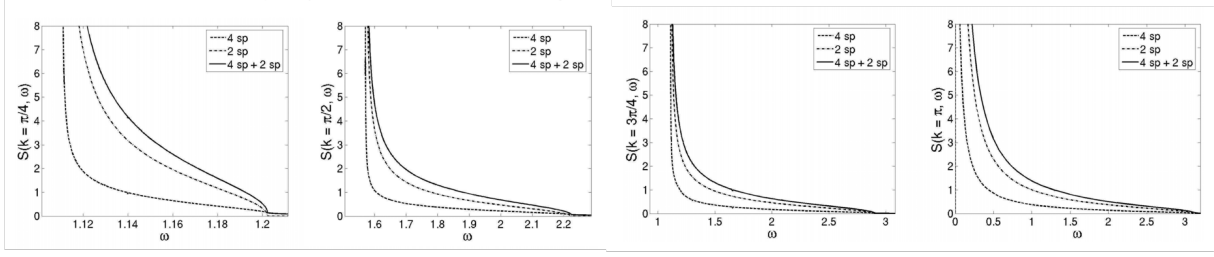
The lower boundary in Eq.3.1 was calculated by Des Cloizeaux and Pearson [43], and it is remarkable that it differs from classical AFM spin-wave dispersion relation $E(k) = J|\sin(k)|$ by a factor of $\pi/2$. As a consequence, it was assumed that for a larger spin value, the Heisenberg model converges to the classical limit. However, in 1983 Haldane [42] discovered that the ground state of spin chains strongly depends on the spin value but in another sense – it is different for integer and half-integer spins. Namely, for integer spins, the lowest-lying excitations are separated from the ground state by an energy gap (Haldane gap), and its spin-spin correlations are decaying exponentially: $\langle S_0^\alpha \cdot S_r^\alpha \rangle = \frac{(-1)^r}{\sqrt{r}} \exp^{-r/\xi}$, where ξ is a correlation length.

A big step forward was done by Müller et al. in the series of work (e.g. [44]), where they gave the expression for the spectral weight for the dynamical structure factor of spin-1/2 antiferromagnetic Heisenberg chain in zero field:

$$S^{zz}(q, \omega) = \frac{A}{\sqrt{\omega^2 - \epsilon_1^2(q)}} \Theta(\omega - \epsilon_1(q)) \Theta(\epsilon_2(q) - \omega),$$

where A is the amplitude, ϵ_1 and ϵ_2 are lower and upper boundaries of the two-spinon continuum given by Eq.3.1 and Eq. 3.2 respectively. However, for several materials [7, 45–47] it has been observed that two-spinon states given by Müller ansatz underestimate the total spectral weight observed in the inelastic spectra. Those discrepancies are related to four-spinon states. Two- and four-spinon dynamical structure factor has been calculated by Caux in [48], where it has been shown that four-spinon states carry approximately 30% of the total spectral weight (Fig.3.1), and later on showed a remarkable agreement with the most recent neutron experiments [49].

In zero field, the ground state is a singlet, and therefore the transverse and longitudinal fluctuations are equivalent. In contrary, once the magnetic field is applied ($\mathbf{H} \parallel \hat{\mathbf{z}}$), one has to treat the longitudinal fluctuations S^{zz} and the transverse fluctuation $S^{xx} = S^{yy}$ separately. In [44], authors demonstrated that the splitting of the two-spinon continuum into many continua associated with incommensurate soft modes is a striking aspect of the model's dynamics in intermediate field. Their positions change with the applied field so that the incommensurate wave vector q is directly proportional to the magnetization m via $q = 2\pi m$ (Fig.3.2). In 1997, the incommensurate positions of the soft modes were first measured in Copper Benzoate [47].


FIGURE 3.1

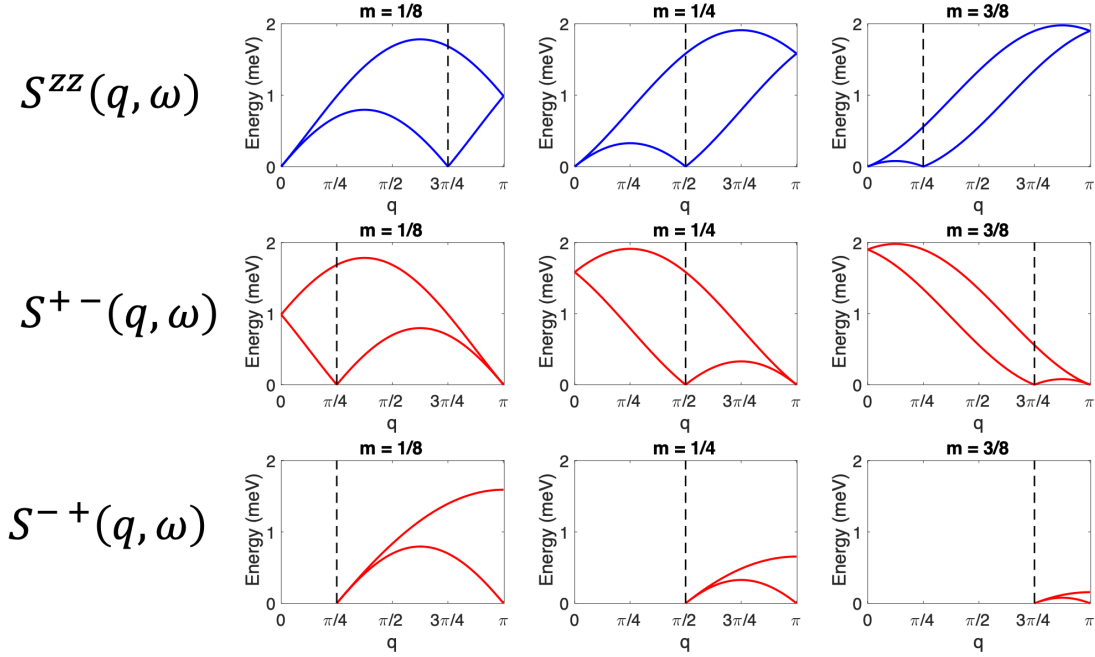
Plots of the two- and four-spinon parts of the dynamical structure factor at momenta $k = \pi/4$, $\pi/2$, $3\pi/4$ and π . Adapted from [48].

The identification of quasiparticles governing the spectra in the applied magnetic field was done by Karbach et al [50, 51]. Their central idea is to reconfigure the Bethe ansatz ground state into a new "quasiparticle vacuum". This new state connects continuously the zero field spinon vacuum and the saturation field magnon vacuum. Those quasiparticles that govern the low-energy part of the excitation spectrum were termed as psinon ψ and antipsinon ψ^* . Similar to spinons, they are fractional excitations with spin $S^z = 1/2$ and $S^z = -1/2$ respectively and are created in an even number by inelastic neutron scattering, so that the spectrum appears to be continuous. In [51], dominant excitations were identified, carrying the maximum spectral weight. However, a significant part of the spectral weight, which lies at higher energies, in S^{+-} dynamical structure factor could not be explained in terms of two-psinon 2ψ or psinon-antipsinon $\psi\psi^*$ continua. The missing spectral weight has been attributed to Bethe n -strings [52], which can be regarded as n -magnon bound state.

Using Bethe ansatz solutions, M. Kohno has calculated [52] the dynamical structure factors $S^{+-}(k, \omega)$, $S^{-+}(k, \omega)$, and $S^{zz}(k, \omega)$ for spin-1/2 Heisenberg antiferromagnetic spin chain. Considering a chain of $L = 320$ spins, he has considered the excitations up to $2\psi 2\psi^*$, which correspond to the four-spinon states in zero-field and satisfy 90% of the $S^{-+}(k, \omega)$ sum rules.

Figure 3.3 shows the dynamical structure factors for a finite $L = 320$ spin chain. Each column with $S^{+-}(k, \omega)$, $S^{-+}(k, \omega)$, and $S^{zz}(k, \omega)$ corresponds to an individual M value, which represents the number of down spins in the chain and is directly linked with magnetization $m = 1/2 - M/320$ and magnetic field. Therefore, a larger M corresponds to the smaller applied magnetic field. Now, we will look how the dynamical structure factor evolves with the applied magnetic field.

For the $S^{+-}(k, \omega)$, a significant part of the continuum is attributed to 2-strings solutions with $\psi\psi^*$ and 3-string solutions with 2ψ . The higher-energy continuum ($\omega/J > 2$) is mainly associated with so-called 2-string solutions with ψ . By increasing the magnetic field, this high-energy continuum separates from the low-energy continuum with the spectral weight gradually lost and reduces to a two-magnon state above the saturation field. The low-energy incommensurate mode


FIGURE 3.2

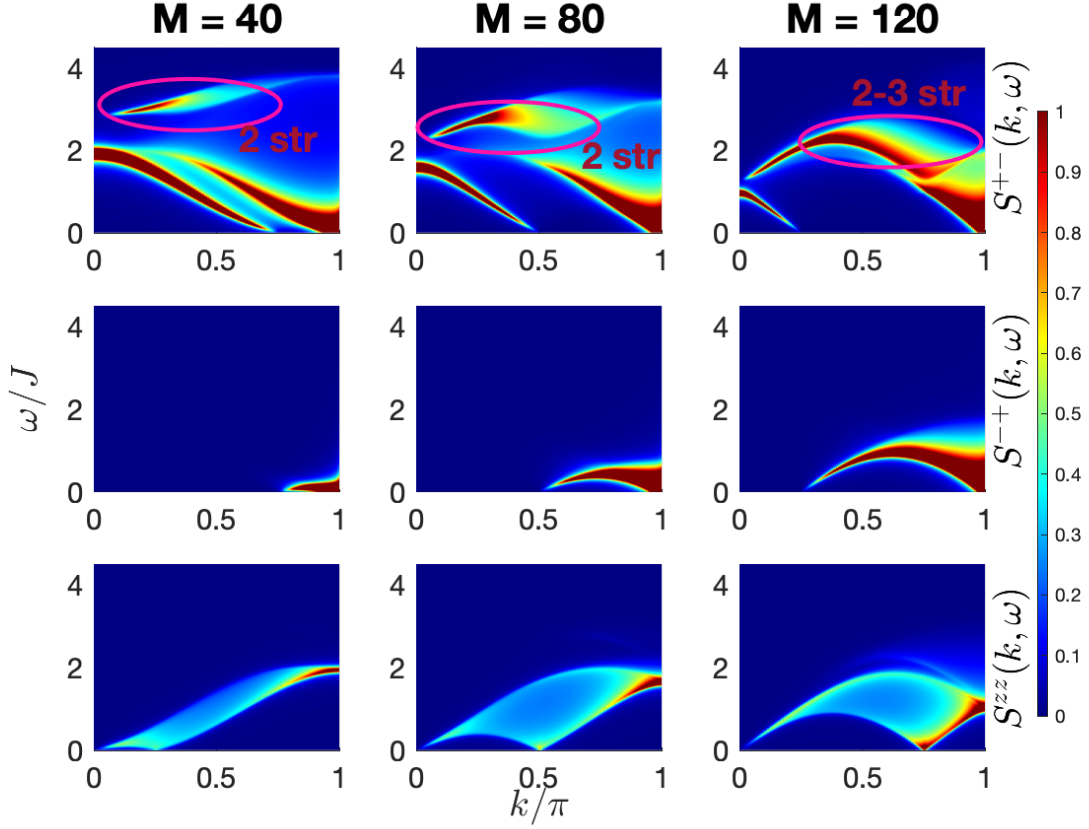
Lineshapes of dynamical structure factors $S^{zz}(q, \omega)$, $S^{+-}(q, \omega)$, $S^{-+}(q, \omega)$ of spin-1/2 Heisenberg antiferromagnetic spin chain calculated for different magnetization values (from left to right).

arising at $k = 0$ and extending up to $k = 2\pi m$ at zero energy transfer is related to two-antipsinon continuum, of which one moving antipsinon is the dominant part. Overall, solutions up to $2\psi 2\psi^*$ together with 2-strings with ψ , 2-strings solution with $\psi\psi^*$ and 3-strings with 2ψ saturate the $S^{+-}(k, \omega)$ sum rule by 80%.

For the $S^{zz}(k, \omega)$, the main contribution is attributed to $\psi\psi^*$ excitations. At the same time, at lower fields, one has to take into account 2-string solutions together with 2ψ , which are responsible for the appearance of higher-energy continuum centered at $k = \pi$ together with all solutions up to $2\psi 2\psi^*$ to favor more than 90% of the sum rules.

Finally, for the $S^{-+}(k, \omega)$, one can observe only one continuum associated mainly with dominant 2ψ excitations, and consideration of higher-order particles satisfy the sum rule of more than 90%.

Experimentally, Bethe strings are observed to constitute the excitation spectrum in various materials such as $\text{SrCo}_2\text{V}_2\text{O}_8$ [53], $\text{BaCo}_2\text{V}_2\text{O}_8$ [54], and YbAlO_3 [55]. However, none of those compounds belongs to the "pure" more like Heisenberg systems: first two belongs to the Heisenberg-Ising chains with $\Delta \approx 2$, the latter has a large spin-orbital contribution to the magnetic moment. Below we present a more prominent example of model one-dimensional Heisenberg $s = 1/2$ system.

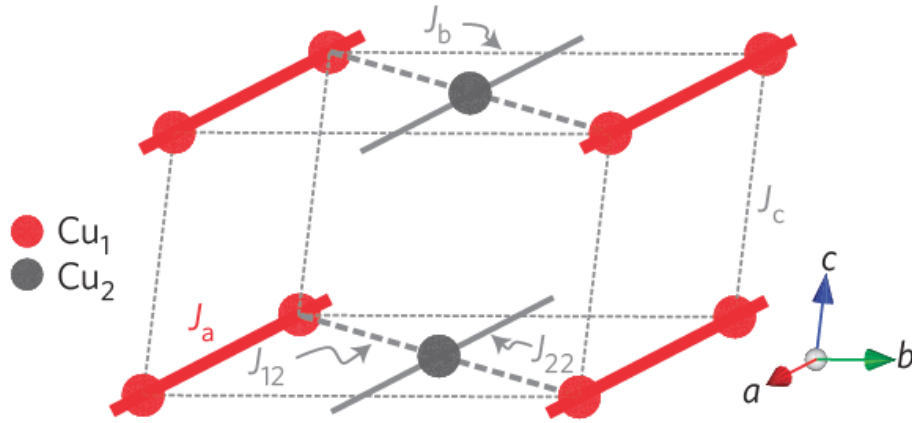

FIGURE 3.3

Dynamical structure factor calculated by M. Kohno [52] for $M = 40, 80, 120$. The definition of M is presented in the text.

3.2 STATE OF THE ART $\text{CuSO}_4 \cdot 5\text{D}_2\text{O}$

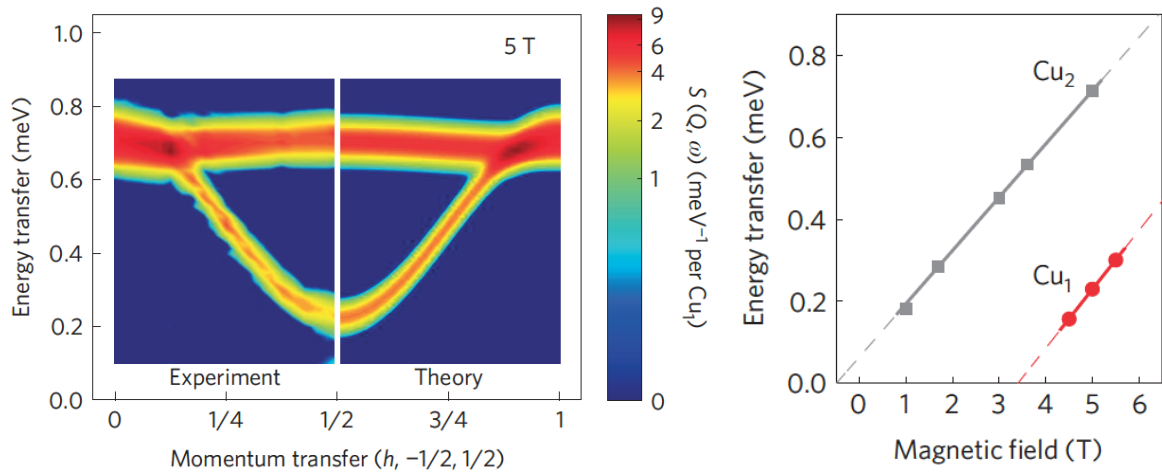
$\text{CuSO}_4 \cdot 5\text{D}_2\text{O}$ belongs to the model example of the 1D AFM quantum Heisenberg system. Its crystal structure is triclinic and was firstly published in [56]. By means of inelastic neutron scattering, M. Mourigal et al. [49] have demonstrated excellent one-dimensionality of $\text{CuSO}_4 \cdot 5\text{D}_2\text{O}$. There are two copper Cu^{2+} ions in the unit cell, which constitute two different magnetic subsystems: Cu_1 ions at (0,0,0) form one dimensional chain along a -direction with $J = 0.252(17)$ meV, and Cu_2 ions at (0.5,0.5,0) ferromagnetically coupled with $J_{22} = -0.012(18)$ meV Fig. 3.4. The interaction between two different sites, Cu_1 and Cu_2 , is found to be $J_{12} = -0.020(22)$ meV, which is less than $0.1J$.

In [49], they have started from spin dynamics in fully polarized state $H = 5$ T, where the excitation spectrum is correctly described by linear spin-wave theory (Fig.3.5 *left*). Two modes are expected and observed: the cosine-shape branch corresponds to the Cu_1 chain atom, and the flat mode corresponds to the almost isolated Cu_2 atom. By measuring magnon energies as a function of field (Fig.3.5 *right*), they obtained g -tensors for each Cu-site: the dispersive branch


FIGURE 3.4

Magnetic unit cell and interactions scheme of $\text{CuSO}_4 \cdot 5\text{D}_2\text{O}$: red balls correspond to chain ions Cu_1^{2+} , grey balls correspond to isolated sites of Cu_2^{2+} . Adapted from [49].

emerges at zero field at saturation field value $H_s \approx 3.6$ T, whereas the flat mode is directly proportional to the magnetic field strength. The straight line fits correspond to $g_1 = 2.49(6)$, $g_2 = 2.25(5)$.


FIGURE 3.5

Left: Excitation spectrum of $\text{CuSO}_4 \cdot 5\text{D}_2\text{O}$ in the fully polarized state; *right:* magnon energies of two different copper sites as a function of magnetic field. Adapted from [49].

In zero field, they have concluded that two- and four-spinon excitations need to be considered to match 98(8)% of the spectral weight, where 30% relate to four-spinon states.

3.3 TIME-OF-FLIGHT EXPERIMENT

To have a full overview of chain dynamics in the applied magnetic field, we have performed an inelastic neutron experiment on time-of-flight (TOF) spectrometer IN5 (ILL, Grenoble), which is shown in Fig. 2.4.

3.3.1 EXPERIMENTAL DETAILS

$\text{CuSO}_4 \cdot 5\text{D}_2\text{O}$ sample (Fig. 3.6) was glued to a Cu holder, thus ensuring a good thermalization and inserted into a vertical cryomagnet reaching up to 10T together with a dilution fridge. An experiment was performed at $T = 100$ mK above the Néel temperature T_N [57]. Incident neutron wavelength was $\lambda = 6$ Å with chopper speed 12000 rpm, thus providing energy resolution of 0.048 meV FWHM at zero energy transfer.

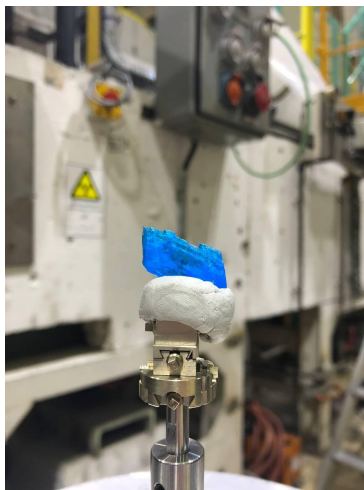


FIGURE 3.6
Aligned $\text{CuSO}_4 \cdot 5\text{D}_2\text{O}$ sample used for the IN5@ILL experiment.

3.3.2 DATA REDUCTION IN MANTID

Data reduction was carried out in Mantid [58]. Raw data were prepared for the analysis as follows:

- 1) detector counts are normalized to the monitor, which reflects the number of incident neutrons;
- 2) mask has been applied, based on a list of "noisy" (defective) detector tubes, a value of the spectrum integral, and accessible angles;
- 3) normalization by vanadium to correct for detector efficiency;
- 4) convert units from time-of-flight to energy transfer ΔE ;

- 5) $\frac{k_i}{k_f}$ correction in order to transform differential cross-section into dynamic structure factor;
- 6) rebinning of the energy axis.

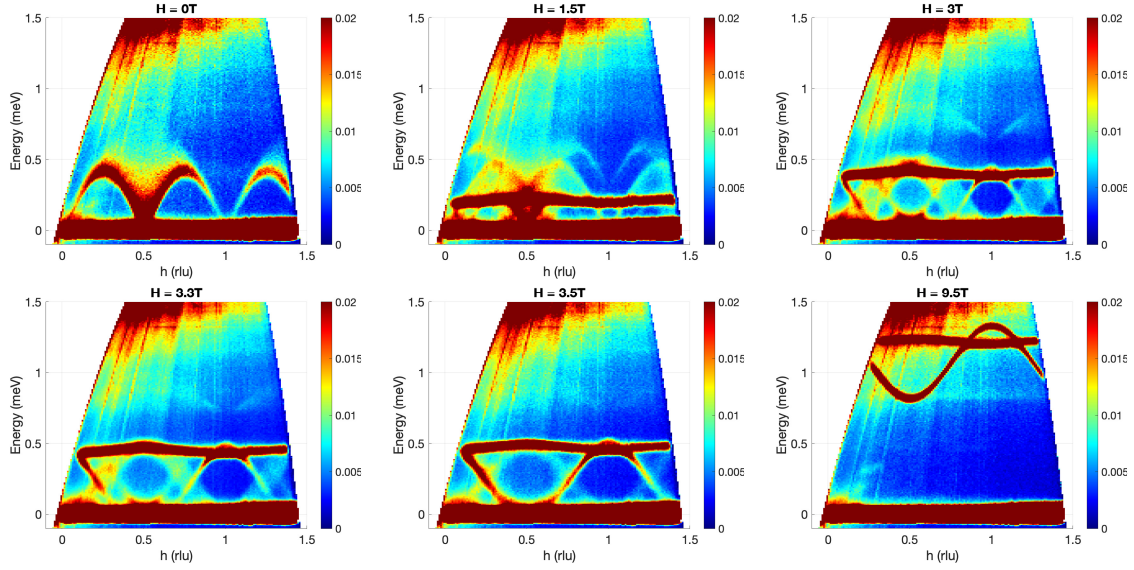
The output of the above mentioned steps is resolution-convoluted structure factor $S(\omega)$ and its errors for each detector; detector position and size information, stored along with the crystal orientation angle Ψ and the incident energy E_i .

3.3.3 CRYSTAL ORIENTATION

A sample was aligned with two reciprocal axes $(1\ 0\ 0)$ and $(0\ 1\ 1)$ in the scattering plane. The choice of this scattering plane is due to that $q_{1D} = (1 - 0.3877 - 0.2953)$ axis is very close to the scattering plane (2.8° out).

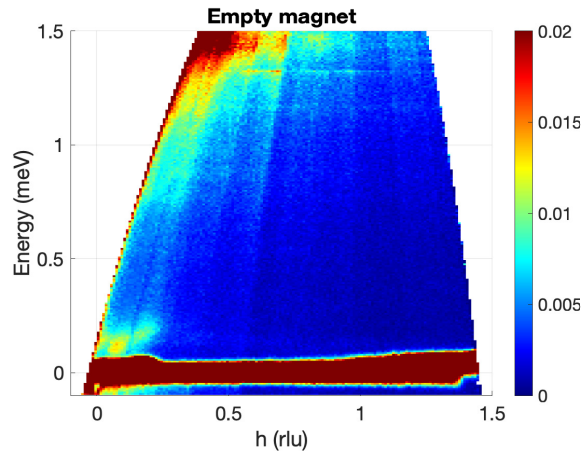
We have used Horace' [59] software to manipulate four-dimensional experimental dynamical structure factor $S(\mathbf{Q}, \omega)$. First, we had to check the crystal orientation. Corrections for crystal tilt relative to the scattering plane were performed as an iterative procedure, which included consideration of 1) peaked-feature widths, shapes, and intensities (in constant $\mathbf{Q}(h)$ cuts); 2) positions of those peaks in h -space with constant energy cuts in order to have a symmetric profile around $h = 0.5$ rlu and $h = 1$ rlu. In short, the lattice parameter a , the angle responsible for tilts under real a direction, and the angle responsible for misorientations about a vector perpendicular to the scattering plane, were the parameters to vary. As model spectra, cuts of 0 T and 9.5 T data were only taken into account, since it is well-known [49], what has to be observed. Overall, we refined only $a = 6.072(11)$ Å lattice parameter, while keeping the rest as they were published in literature [56]: $b = 10.736$ Å, $c = 5.986$ Å, $\alpha = 82.267^\circ$, $\beta = 107.433^\circ$, $\gamma = 102.667^\circ$. According to the refined a parameter, the orientation axes were redetermined as $u = (1\ -0.3149\ -0.3149)$, $v = (0\ 1\ 1)$, and $w = u \times v$. In addition, a tilt of 0.31° of the vertical w axis was found. Once the orientation and lattice constants were set, detector positions were converted to Q_u, Q_v, Q_w momentum transfer coordinates.

The data after this step is shown in Fig. 3.7 and contain several different features. The magnetic signal is clearly distinguishable in the energy region of $0.1 < E < 1$ meV. A flat dispersion-less mode is observed due to the second Cu^{2+} ion at different energies depending on the strength of the magnetic field. A large elastic signal at zero energy transfer is seen mainly due to incoherent scattering from the sample.


FIGURE 3.7

Measured dynamic structure factor $S(Q, \omega)$ along chain direction in vertical magnetic fields $H = 0, 1.5, 3, 3.3, 3.5, 9.5$ T.

An additional field-independent scattering can be found at the top $0.75 < E < 1.6$ meV and at the lower part $E < 0.75$ meV in low- h region $h < 0.3$ rlu of each spectrum. We can observe a similar scattering in the spectrum of an empty magnet in Fig.3.8, thus we conclude that these features are not from the sample and related to the sample environment and will be treated as a background.


FIGURE 3.8

Measured dynamic structure factor $S(Q, E)$ of an empty magnet.

Therefore, data preparation consists of the following steps. From each data-set, one has to subtract 1) background scattering, which is related to the sample environment; 2) incoherent scattering, and 3) multiple scattering. In addition, one has to correct data with the Cu^{2+} magnetic

form-factor.

3.3.4 BACKGROUND SUBTRACTION

Despite that we have measured an empty magnet at the same incident energy at the cryostat base temperature, the measured spectrum was not sufficient (Fig.3.8) to reproduce all sample environment scattering features since the dilution insert with the sample was already extracted. Therefore, one of the ways to describe the background would be a combination of 9.5 T and 0 T data.

In a fully polarized state at 9.5 T, two modes are expected, corresponding to the Cu_1^{2+} and Cu_2^{2+} ions in the unit cell. Since the interaction within the chain is antiferromagnetic, the minimum of the dispersion is observed at $h = 0.5$. According to [49], the corresponding Zeeman shift and the bandwidth are $\Delta = g\mu_B H/2S = 1.36(3)$ meV and $2J = 0.517(9)$ meV respectively. Therefore, taking into account IN5 energy resolution $\sigma_\omega = 0.02$ meV, the minimum of the dispersion is expected in the energy range $\Delta - 2J - \sigma_\omega = 0.82(5) < E_{\min} < \Delta - 2J + \sigma_\omega = 0.86(5)$ meV. For zero field, the upper band of spinon continuum is given by Eq.3.2, so that $E_{\text{up}} = 0.804(3)$ meV. Therefore, we expect the upper band of the spinon continuum in the energy range $0.784(4) < E_{\text{up}} < 0.824(3)$ meV. Hence, the following energy intervals, above $E > 0.83$ meV at $H = 0$ T and below $E < 0.77$ meV at $H = 9.5$ T should be free of any excitations and thus can be taken as a background. From constant energy cuts in Fig. 3.9, we can estimate when the chain dispersive contribution starts. Obviously, the peak-feature at constant energy transfer $E = 0.78$ meV at $h = 0.5$ rlu corresponds to the magnon intensity, whereas below $E < 0.78$ meV no additional intensity around $h = 0.5$ rlu is observed.

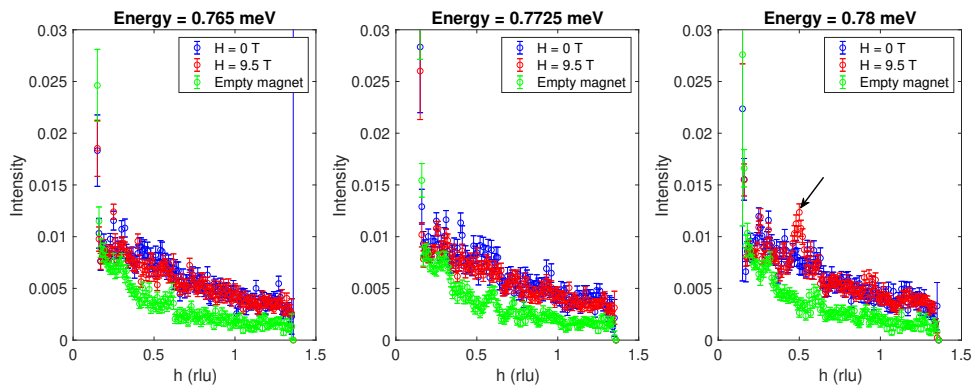


FIGURE 3.9

Several constant energy cuts showing absence of spin-wave excitations at energies below 0.78 meV at 9.5 T. The arrow on the *right* figure indicates its appearance.

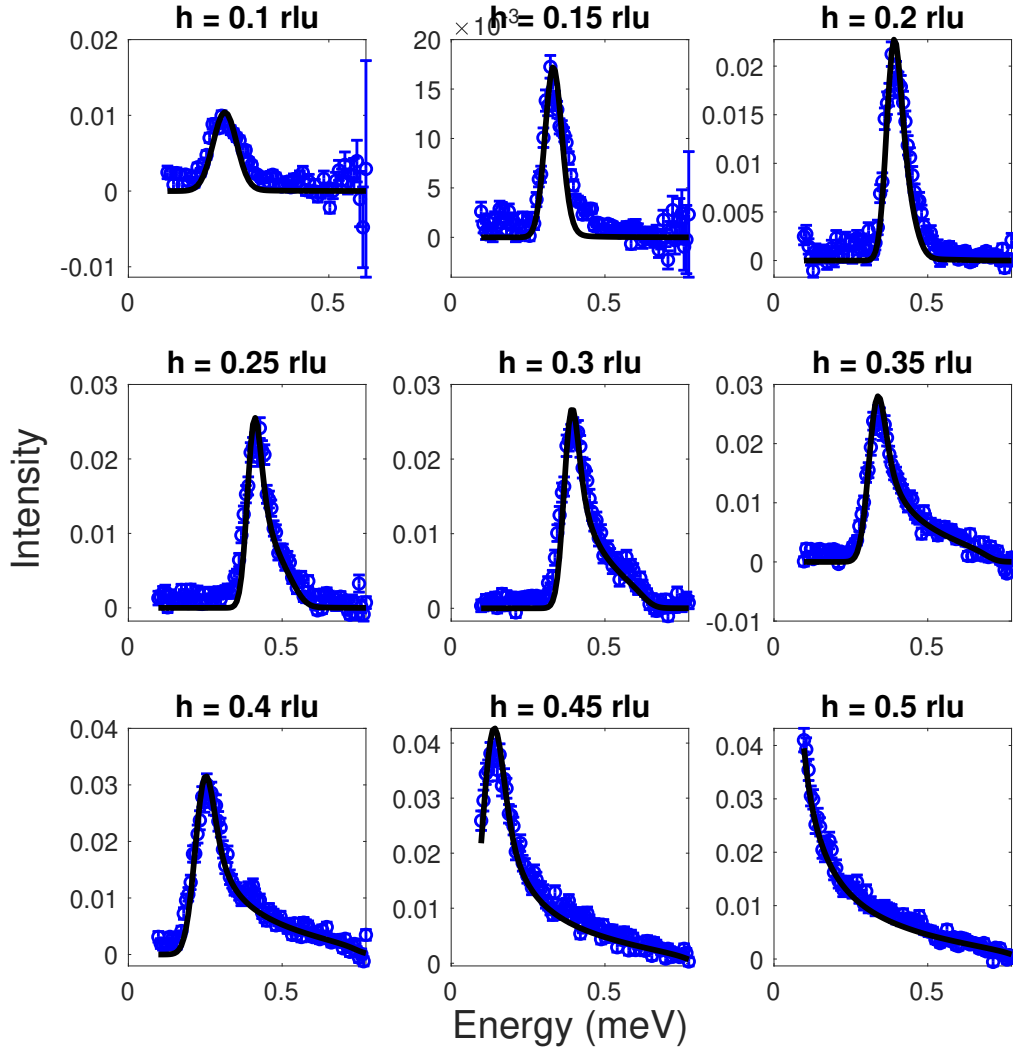
For the remaining region in between $0.78 < E < 0.83$ meV we estimated the background as follows from $H = 0$ T data. In this energy interval, the upper part of 2-4 spinon continua

still might be in. To avoid possible oversubtraction, we fit 0 T data with Caux [48] $S^{2+4}(h, \omega)$ dynamic structure factor and add this contribution for energies above $E \geq 0.78$ meV.

Note that for an isotropic ground state in zero field, we have $S^{xx}(h, \omega) = S^{yy}(h, \omega) = S^{zz}(h, \omega)$. However, only $S^{yy}(h, \omega) + S^{zz}(h, \omega) = 2S^{yy}(h, \omega)$ contribute to the inelastic neutron scattering cross-section. We have fitted experimental excitation spectrum in the energy range $0.1 < E < 0.78$ meV with the following function

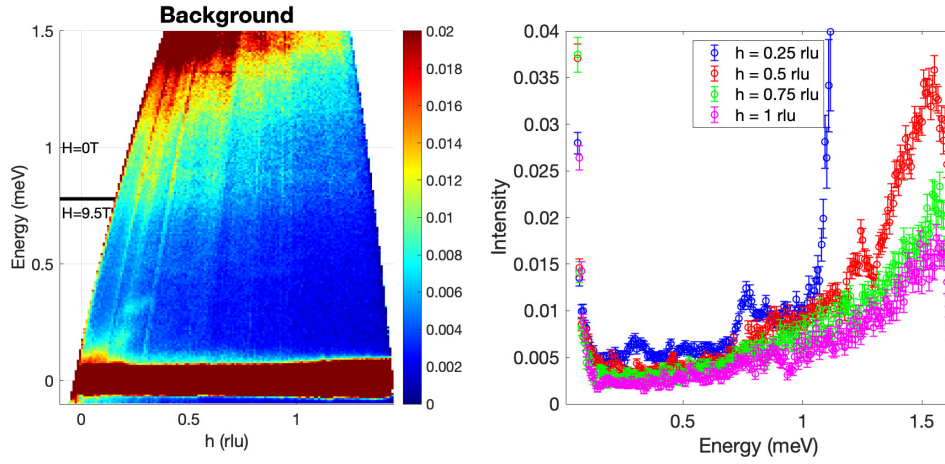
$$S_{exp}(h, \omega) = \frac{2}{3} A_{Caux} C_{Caux} \int_0^1 \int_0^{2\pi J} S^{2+4}(h', \omega') R(h' - h, \omega' - \omega) dh' d\omega', \quad (3.3)$$

where $\frac{2}{3}$ reflects the contribution to the neutron cross-section, C_{Caux} is a sum rules normalization to the total spin $S(S + 1)$, A_{Caux} is an overall scale factor between Caux and experiment, J is an exchange coupling within the chain, $R(h, \omega) = \frac{1}{\sqrt{2\pi}\sigma_h} \frac{1}{\sqrt{2\pi}\sigma_\omega} \exp\left(-\frac{h^2}{2\sigma_h^2}\right) \exp\left(-\frac{\omega^2}{2\sigma_\omega^2}\right)$ is the simplified resolution function in both ω and h directions with $\sigma_\omega = 0.02$ meV and $\sigma_h = 0.01$ rlu. Simultaneous fit of constant momentum transfer cuts in the energy range $0.1 < E < 0.78$ meV provided the following parameters: $A_{Caux} = 0.0054(3)$ and $J = 0.254(1)$ meV, and the corresponding lineplots with experimental data are shown in Fig.3.10. As one can see, the experimental data is in good agreement with Caux theoretical lineshapes [48], and exchange parameter J is in accordance with previously published data [49].


FIGURE 3.10

Experimental constant momentum transfer cuts (blue markers) with Caux lineplots (black solid line). The parameters for Eq.3.3 are specified in the text above.

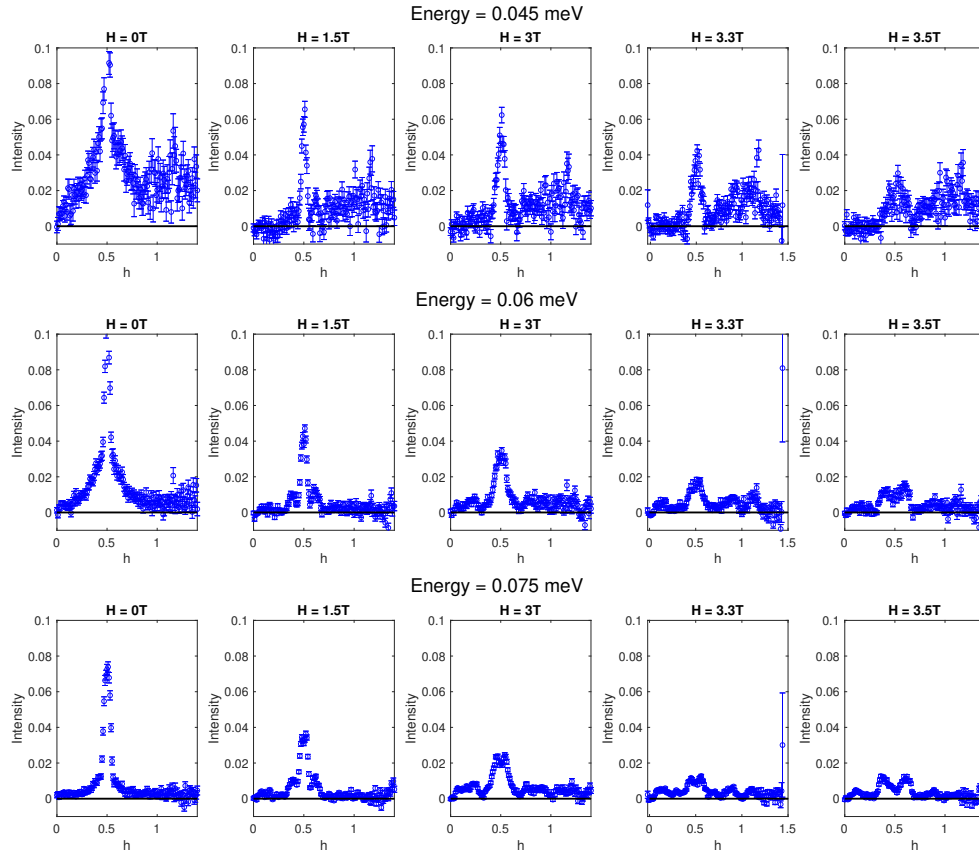
By combining spinon-subtracted $H = 0$ T above $E \geq 0.78$ meV and $H = 9.5$ T below $E < 0.78$ meV, we have obtained the background colormap shown in Fig.3.11 *left*. On the right side of Figure, one can see selected constant h lineplots, showing the complexity of the background function. Thus, we would need to perform point-by-point background subtraction since no analytical function would describe the background as good as it is in Fig.3.11.


FIGURE 3.11

Background associated with scattering from the sample environment. Solid black lines indicate the energy region in which the corresponding $H = 0$ T and $H = 9.5$ T were used, as explained in the text. Note that the region of the elastic line at zero energy transfer will be treated separately in the Section below.

3.3.5 INCOHERENT SCATTERING

Assuming that incoherent scattering should be field independent, $H = 9.5$ T data-set is supposed to be an ideal candidate as an incoherent scattering estimate since no excitations are expected below $E < 0.78$ meV. First, we checked, whether the simple subtraction works for constant energy cuts in Fig.3.12. In order to choose the energy below which we would fit the elastic line and afterward subtract it from the spectra, one can prepare constant energy cuts assuming if we would subtract the background as it is in Fig.3.11, that is using the elastic line of 9.5 T data. Obviously, the simple 9.5 T subtraction down to $\text{FWHM} = 0.048$ meV of the elastic line works fine, whereas below $E < 0.048$ meV a substantial part of the field spectra start to be oversubtracted. However, the additional scattering at zero field should not confuse the reader since the flat mode at zero energy is expected.


FIGURE 3.12

Constant energy cuts $E = [0.045, 0.06, 0.075]$ meV (from top to bottom) for each field $H =$ with prior subtraction of $H = 9.5$ T data.

Assuming that elastic line takes a form of a simple Gaussian function, we have performed a fit for all field values and for each h . The peak widths remained unchanged for all field data. However, the difference in the centers between intermediate field data and high field data increased linearly with h . Overall, by adapting the amplitudes and the peak positions of the 9.5 T elastic line, we obtained the spectra shown in Fig. 3.13;

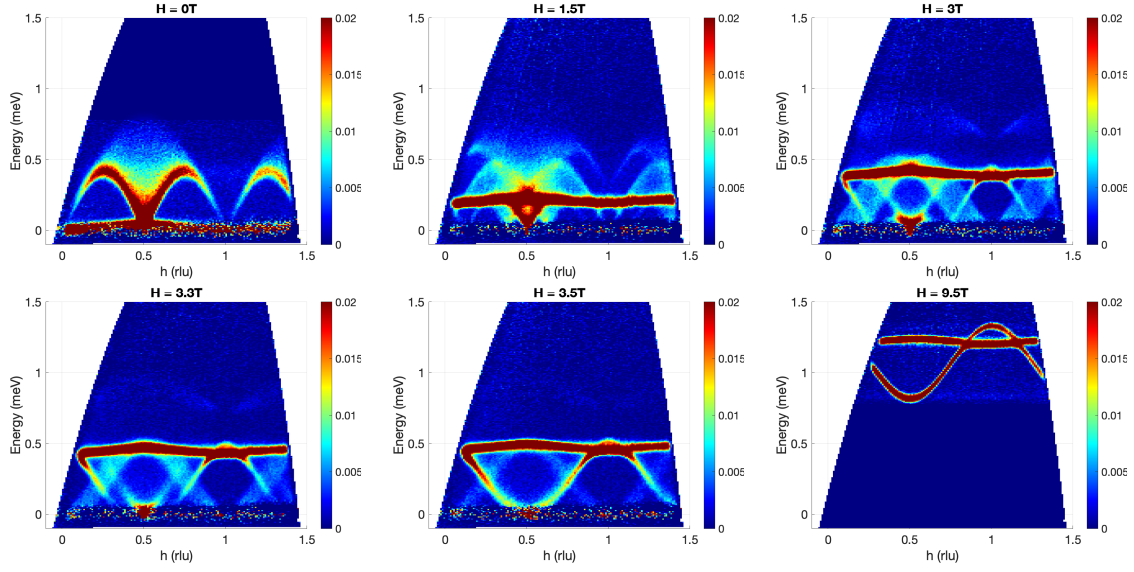


FIGURE 3.13
TOF Experimental maps before multiple scattering correction

3.3.6 MAGNETIC FORM-FACTOR

Since we are dealing with the magnetic neutron scattering, one has to reconstruct the effective magnetic form-factor. Since each pixel has its own Q coordinates (Q_u, Q_v, Q_w), one could calculate $|Q| = \sqrt{Q_u^2 + Q_v^2 + Q_w^2}$, and hence $s = \frac{|Q|}{4\pi}$, and then substitute it to P.J. Brown's [60] analytical approximation for the magnetic form-factor of Cu^{2+} :

$$\langle j_0(s) \rangle = A \exp(-as^2) + B \exp(-bs^2) + C \exp(-cs^2) + D, \quad (3.4)$$

where $A = 0.0232, a = 34.9686, B = 0.4023, b = 11.5640, C = 0.5882, c = 3.8428, D = -0.0137$. By projecting this 4D structure to an a -axis, one can obtain the effective form-factor (Fig.3.14).

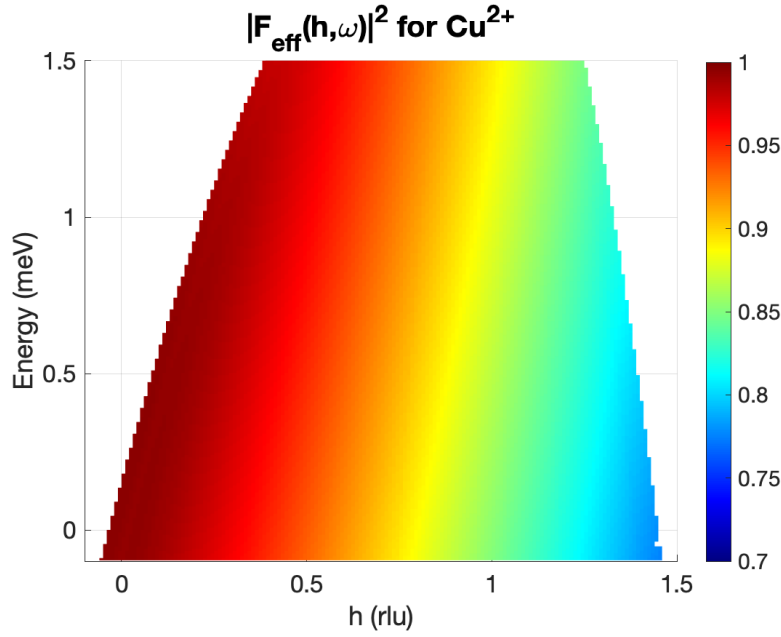
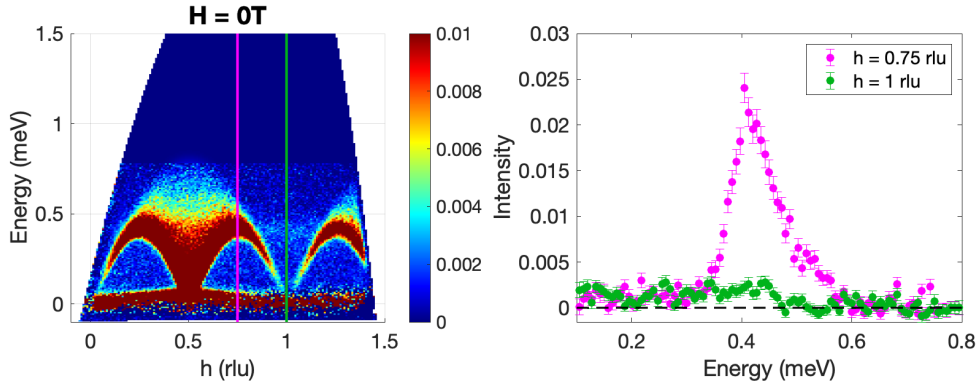


FIGURE 3.14
Effective magnetic form-factor of Cu^{2+} for TOF experiment

Note that we apply the magnetic form-factor correction to the experimental data at the end of Section 3.3. However, we would need this result for multiple scattering correction introduced in the following Section.

3.3.7 MULTIPLE SCATTERING

Due to hydrogen-deuterium exchange in the sample, strong incoherent elastic scattering, which is independent of \mathbf{Q} , is observed in experimental data. In the simplistic case assuming double-scattering process, multiple scattering involves the strong incoherent elastic scattering of the sample and excitations of the two modes. Therefore, the incoherent inelastic scattering is proportional to the density of states of the two copper modes in addition to coherent inelastic scattering of the single scattering process. It can be clearly observed on the $H = 0$ T experimental map in Fig.3.15 *left* as a stripe around $E \approx 0.42$ meV in the region of the zone boundary $h = 1$ rlu. The size of this multiple scattering compare to a real magnetic signal is somewhat around 10% Fig.3.15 *right*. To get rid of this additional effect, we must first determine how it manifests itself in the obtained experimental spectra.


FIGURE 3.15

Left: Dynamical structure factor of $H = 0$ T. Additional stripe-like scattering can be observed in the energy region of $E \approx 0.42$ meV. Solid magenta and green lines show the constant h -cuts at $h = 0.75$ and 1 rlu, respectively, in the *right* figure.

Initially, each experimental map (we define it $\Theta(h, \omega)$) shown in Fig.3.13 was obtained by summing up the intensities of each contributing pixel n : $\Theta(h, \omega) = \frac{1}{N} \sum_{n=1}^N \Theta_n(h, \omega)$. To take into account that after incoherent elastic scattering event, the system undergoes the second scattering event $\mu(\omega)$ with certain probability α together with single scattering event, which is a dynamical structure factor of two modes $S_n(h, \omega) + S_{n,PM}(h, \omega)$ multiplied by magnetic form-factor squared $|F(|Q_n|)|^2$, we can write:

$$\begin{aligned} \Theta(h, \omega) &= \frac{1}{N} \sum_{n=1}^N \alpha \mu(\omega) + \frac{1}{N} \sum_{n=1}^N |F(|Q_n|)|^2 [S_n(h, \omega) + S_{n,PM}(h, \omega)] = \\ &= \alpha \mu(\omega) + \frac{1}{N} \sum_{n=1}^N |F_n(h, \omega)|^2 [S_n(h, \omega) + S_{n,PM}(h, \omega)]. \end{aligned}$$

When one integrates along h the experimental data-set, which in the simplistic picture already contains multiple scattering:

$$\frac{1}{N_h} \sum_h \Theta(h, \omega) = \alpha \mu(\omega) + \mu(\omega) = (1 + \alpha) \mu(\omega). \quad (3.5)$$

From the other hand, by integrating along h theoretical dynamical structure factor one gets:

$$\mu(\omega) = \frac{1}{N_h \cdot N} \sum_{n_h} \sum_{n=1}^N |F_n(h, \omega)|^2 [S_n(h, \omega) + S_{n,PM}(h, \omega)]. \quad (3.6)$$

First, one needs to obtain multiple scattering probability α . This can be found using $H = 0$ T data-set. The choice of these experimental data is explained by the fact that the dynamic structure

factor is known [49] and, in contrast to the data in a field above the saturation $H = 9.5$ T (where one also can obtain the dynamical structure factor by LSWT), the paramagnetic mode overlaps with the spinon continuum only at zero energy transfer and may be neglected, so that we define $\mu(\omega) = \frac{1}{N_h \cdot N} \sum_{n_h} \sum_{n=1}^N |F_n(h, \omega)|^2 \cdot S_{\text{Caux}}^{2+4}(h, \omega)$ (Fig.3.16). Note that in a latter expression, the Caux dynamical structure factor is convoluted with instrumental resolution, and all the parameters were obtained earlier in Section 3.3.4.

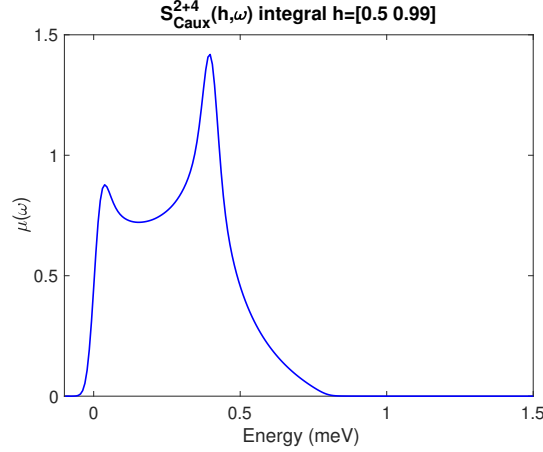


FIGURE 3.16

Multiple scattering function $\mu(\omega)$ obtained by integrating $|F(h, \omega)|^2 \cdot S_{\text{Caux}}^{2+4}(h, \omega)$ along $h = [0.5, 0.99]$, thus covering half of a Brillouin zone.

Finally, we fit each constant $h = h_i$ cut of $H = 0$ T data-set with the following expression

$$\Theta(h = h_i, \omega) = A [|F(h = h_i, \omega)|^2 \cdot S_{\text{Caux}}^{2+4}(h = h_i, \omega) + \alpha \mu(\omega)] ,$$

where A and α are fitting parameters. We have obtained $A = 0.005(1)$ and $\alpha = 0.196(2)$. In order to check the values and goodness of fitting, we have subtracted multiple scattering from $H = 0$ T data-set. In Fig.3.17, the signs of spectra improvement are distinctly visible.

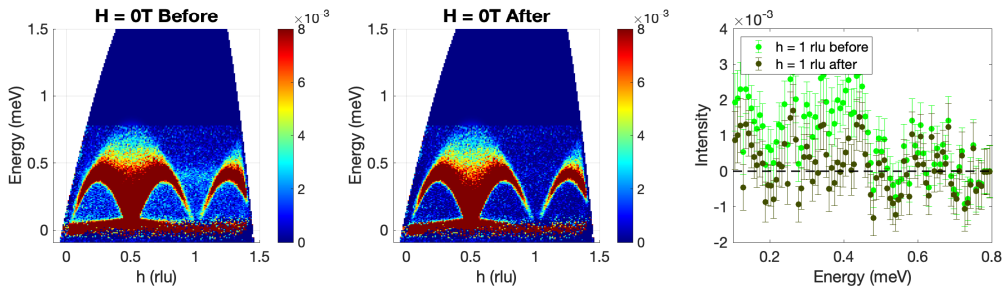


FIGURE 3.17

Comparison of original and multiple scattering subtracted $H = 0$ T data-sets.

Once multiple scattering probability is found, we can subtract multiple scattering from the other data-sets using the approach expressed in Eq.3.5. This basically means that integrated along h experimental data is a multiple scattering function multiplied by a prefactor $(1 + \alpha)$, expressing that experimental data already contains multiple scattering. Another illustrative example of how this approach works is 9.5 T data-set in Fig.3.18. One can notice an additional stripe-like scattering appearing at $E \approx 0.8$ meV, which was successfully removed by subtracting $\frac{\alpha}{1+\alpha} \mu(\omega)_{9.5\text{T}}$.

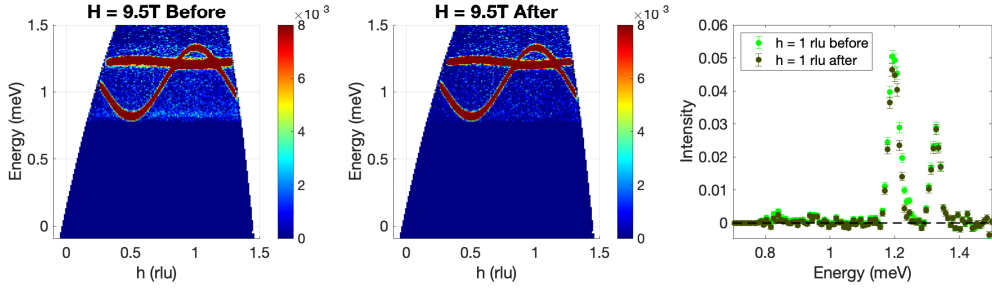


FIGURE 3.18

Comparison of original and multiple scattering subtracted $H = 9.5$ T data-sets.

Finally, after multiple scattering subtraction, we have applied the effective magnetic form-factor introduced in Section 3.3.6 to the data, and the result is shown in Fig.3.19.

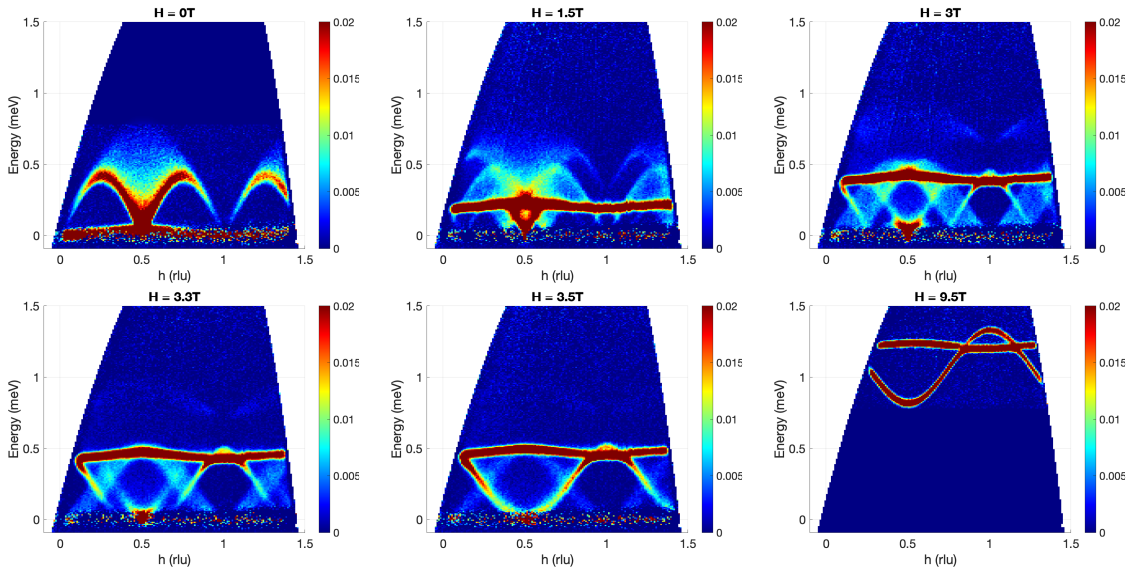


FIGURE 3.19

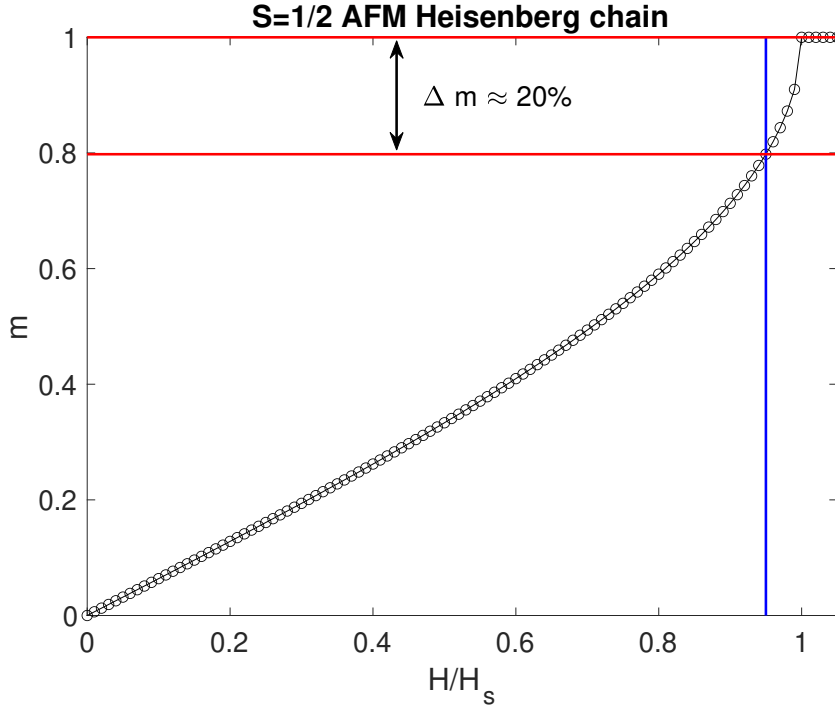
Dynamical structure factors $S(h, \omega)$ for different field values $H = 0, 1.5, 3, 3.3, 3.5, 9.5$ T with applied magnetic form-factor correction and subtracted background, incoherent and multiple scattering.

3.3.8 MAGNETIZATION VALUES

In order to compare the experimental dynamical structure factor with theory, one has to know the magnetization value (Section 3.1) for each data-set. From ESR [61], it is known that the gyromagnetic tensors of both copper atoms are anisotropic. They provide precise values:

$$\mathbf{g}_1 = \begin{pmatrix} 2.080 & 0 & 0 \\ 0 & 2.080 & 0 \\ 0 & 0 & 2.4286 \end{pmatrix} \text{ and } \mathbf{g}_2 = \begin{pmatrix} 2.080 & 0 & 0 \\ 0 & 2.080 & 0 \\ 0 & 0 & 2.4046 \end{pmatrix} \quad (3.7)$$

for Cu_1^{2+} chain and Cu_2^{2+} isolated ions respectively. Note that g_\perp , $g_{1\parallel}$ and $g_{2\parallel}$ are given with respect to the principle axes of copper octahedra in the tetragonal coordinate system. When magnetic field \mathbf{H} is perpendicular to the scattering plane, its direction is $[0,1,-1]$ in real triclinic space, so that effective gyromagnetic tensors are $g_{1eff} = |\mathbf{g}_1 \cdot \hat{\mathbf{H}}| = 2.38$, $g_{2eff} = |\mathbf{g}_2 \cdot \hat{\mathbf{H}}| = 2.17$. Those values are $\approx 5\%$ smaller than they were previously reported in [49]. This uncertainty therefore, leads to an uncertainty in saturation field determination H_s . Using Müller's approximation [44] of a magnetization curve for $S = 1/2$ antiferromagnetic Heisenberg spin chain, we can see that at fields close to the saturation when the dynamic properties of the chain evolve quite fast, 5% variation of H_s explicitly leads to a $\approx 20\%$ variation (Fig.3.20) of the magnetization value. Therefore, one would need to find a complementary approach to avoid those uncertainties related to the anisotropic gyromagnetic g -tensor.


FIGURE 3.20

Magnetization curve (black circles) for $S = 1/2$ antiferromagnetic Heisenberg spin chain using approximation given in [44]. The solid blue lines correspond to a confidence interval of a saturation field value H_s . The solid red lines correspond to a confidence interval of a magnetization value m .

It is known [44] that in the applied magnetic field, the incommensurate mode emerges in the spectrum and is directly proportional to magnetization $k = 2\pi m$ at zero energy transfer. Moreover, there is an almost linear dependence in the low-energy region according to $S^{+-}(k, \omega)$ in the first row of Fig. 3.3. Below, the analysis only for $H = 1.5$ T is shown, other fields were treated in the same way.

Initially, at our disposal, we had $S^{+-}(h, \omega)$, $S^{-+}(h, \omega)$ and $S^{zz}(h, \omega)$ calculated by M. Kohno for $M = 120$ and $M = 126$ down spins for a finite $L = 320$ spin chain, which we convoluted with experimental resolution. For simplicity, and just for the purpose of estimating the Cu_1^{2+} magnetization, we compare experimental dynamical structure factor with $S^{av}(h, \omega) = \frac{1}{4}(S^{+-}(h, \omega) + S^{-+}(h, \omega)) + S^{zz}(h, \omega)$ [52]. The corresponding colormaps are shown in Fig. 3.21.

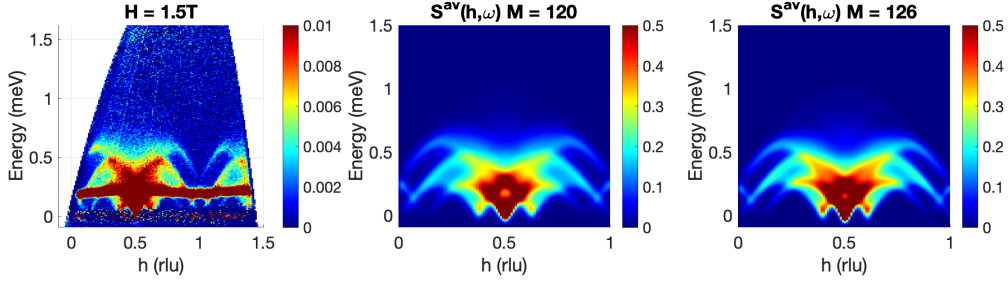


FIGURE 3.21

Left: Experimental data-set for $H = 1.5$ T; *middle:* $S^{av}(h, \omega)$ for $M = 120$; *right:* $S^{av}(h, \omega)$ for $M = 126$

We compare constant energy cuts, where the incommensurate mode occurs as the second sharp feature, for the energies below $E \approx 0.15$ meV in order to avoid overlapping with paramagnetic mode (Fig.3.22). We fit (solid black lines) the position of the incommensurate mode for the experimental data and Kohno's $M = 120$ and $M = 126$ dynamical structure factors with Gauss function. Note that at this step, Kohno's data were scaled by a number in order to have intensities more or less at the same scale.

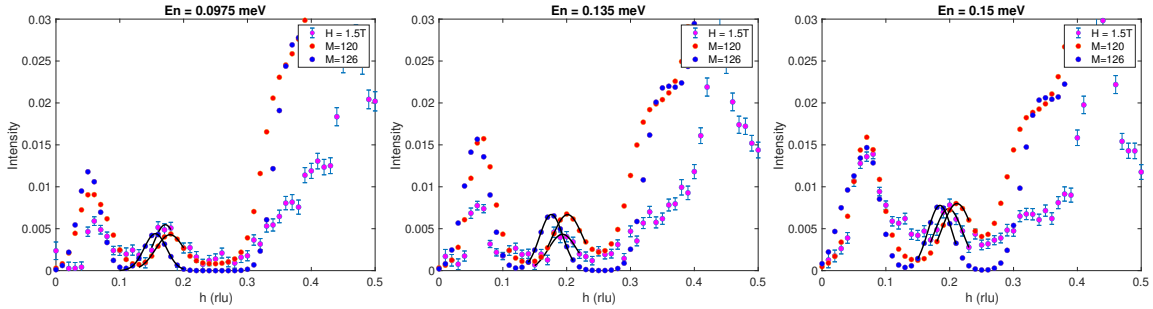
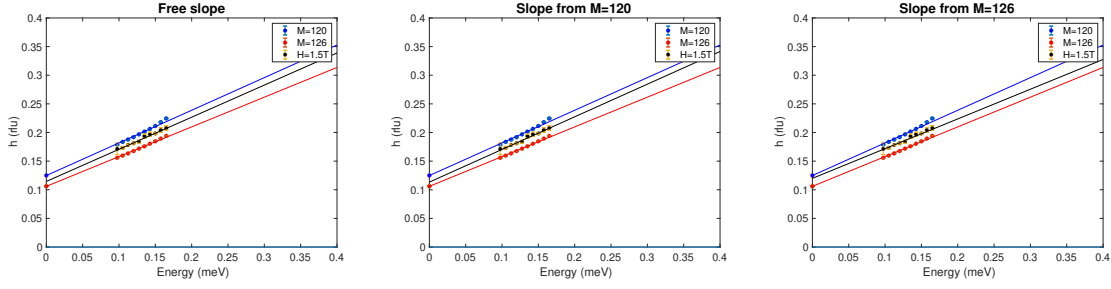


FIGURE 3.22

Several constant energy cuts. Magenta filled circles correspond to the experimental $H = 1.5$ T data, red – $M = 120$, blue – $M = 126$. Solid black lines show the fit with Gauss.

The result of sequential fittings is shown in Fig.3.23. Since we know that at zero energy transfer the incommensurate mode has a position $h = m = 1/2 - M/320$, we can add those points for calculated theory data. Without any quantitative analysis, one can see that experimental data falls somewhere in between $M = 120$ and $M = 126$. Using linear approximation, we find the slopes for experimental data (black), $M = 120$ (blue) and $M = 126$ (red). With free slope, experimental data cross zero energy transfer at $h = 0.1146$, which corresponds to $M = 123.328$. With $M = 120$ slope, the data extrapolates to $h = 0.1134$, which is $M = 123.7$. Finally, with $M = 126$ slope, the data extrapolates to $h = 0.1199$, which is $M = 121.6$. Assuming that we have to provide theoretician with integer number M , which corresponds to the number of down spins, for the current data-set of $H = 1.5$ T, we would like to have dynamical structure factor $M = 123$.


FIGURE 3.23

Results of sequential fitting explained above. *Left*: Free slope; *middle*: slope from $M = 120$; *right*: slope from $M = 126$.

In the same manner, the other data-sets were treated. In Table 3.1, we present corresponding M -values for each field, according to the data that was available at the moment of analysis. One can notice that for $H = 3.5$ T (which is very close to the saturation field) we had only one calculated dynamical structure factor for $M = 18$. Nevertheless, we were able to estimate the corresponding M -value using the relation $\Delta h \cdot 320 = \Delta M$.

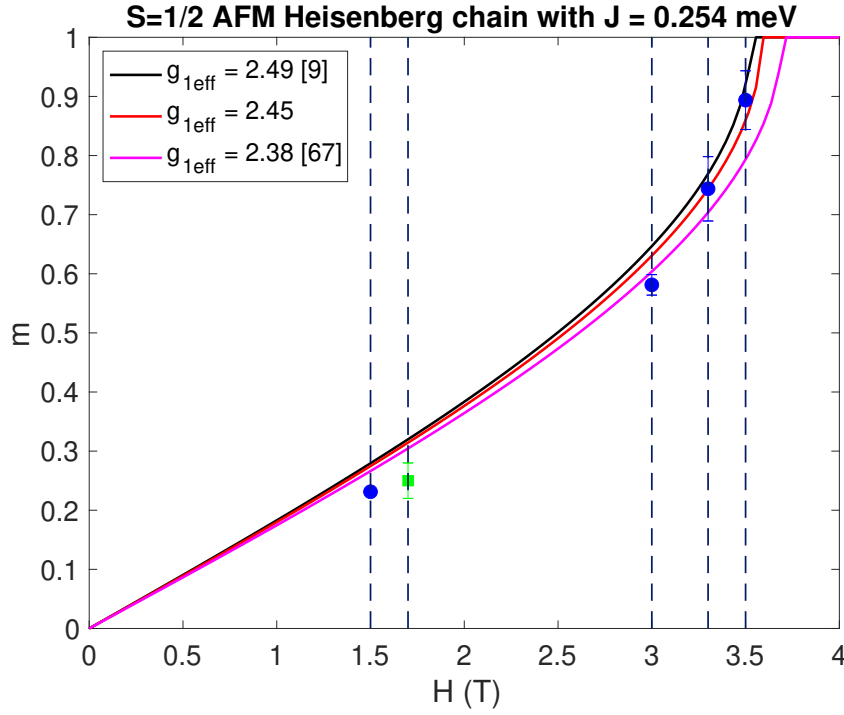
It will be more convenient to rewrite Müller's approximation $m = \frac{2}{\pi} \arcsin \frac{H}{H_s}$ in terms of applied magnetic field:

$$m(H) = \frac{2}{\pi} \arcsin \left(\frac{\mu_B}{2J} g_{\text{eff}} H \right). \quad (3.8)$$

For Fig.3.24, we have converted number of down spins (3rd column in Tab.3.1) to the magnetization values $m(H)$ and presented the obtained results considering different values of the gyromagnetic g -tensor. It can be concluded that the corresponding magnetization values qualitatively follow the trend of Müller's approximation [44], however, not lying on the curve perfectly. One of the reasons could be the influence of the isolated Cu_2^{2+} ions, which create an additional field in which Cu_1^{2+} ions should be considered.

Field value	Available theory	Estimated M value	Compared M value
1.5 T	$M = 120, M = 126$	$M = 123$	$M = 120$
3 T	$M = 80, M = 66$	$M = 67$	$M = 66$
3.3 T	$M = 40, M = 48$	$M = 41$	$M = 40$
3.5 T	$M = 18$	$M = 17$	$M = 18$

TABLE 3.1
Field value estimation.


FIGURE 3.24

Magnetization values obtained from IN5@ILL experiment (blue markers). Solid lines correspond to Müller's approximation given in [44] for different values of g -tensor.

In the next section, we will present a comparison of experimental data with calculations for the closest M -value (4th column of Table 3.1).

3.3.9 PROPER AVERAGE FOR UNPOLARIZED NEUTRONS

For unpolarized neutrons, in vertical field geometry, when the quantization \mathbf{z} -axis is set since $\vec{H} \parallel \mathbf{z}$, $S^{xx} = S^{yy} \neq S^{zz}$. According to Eq.2.6, the measured dynamic structure factor takes the form:

$$\begin{aligned} S_{unpol}(\mathbf{Q}, \omega) &= \sum_{\alpha} (1 - \hat{Q}^{\alpha^2}) S^{\alpha\alpha}(\mathbf{Q}, \omega) = \\ &= (1 - \hat{Q}^{x^2}) S^{xx}(\mathbf{Q}, \omega) + (1 - \hat{Q}^{y^2}) S^{yy}(\mathbf{Q}, \omega) + (1 - \hat{Q}^{z^2}) S^{zz}(\mathbf{Q}, \omega), \end{aligned}$$

where $(1 - \hat{Q}^{\alpha^2})$ is a consequence of the integration over the vertical detector.

Using $S^{xx} = S^{yy} = \frac{1}{4}(S^{+-} + S^{-+})$ and $\hat{Q}^{x^2} + \hat{Q}^{y^2} + \hat{Q}^{z^2} = 1$ we rewrite:

$$S_{unpol}(\mathbf{Q}, \omega) = (1 + \hat{Q}^{z^2}) \cdot \frac{1}{4} [S^{+-}(\mathbf{Q}, \omega) + S^{-+}(\mathbf{Q}, \omega)] + (1 - \hat{Q}^{z^2}) S^{zz}(\mathbf{Q}, \omega). \quad (3.9)$$

Therefore, to have an accurate comparison of the experimental data with theory, we have to multiply Kohno's dynamical structure factors $S^{+-}(h, \omega)$, $S^{-+}(h, \omega)$, and $S^{zz}(h, \omega)$ with corresponding prefactors in Eq.3.9. Since we have four-dimensional data-sets, we have to reconstruct those prefactors according to our projections specified in Section 3.3.3. In Horace [59] notations, $\hat{Q}^{z^2} = \frac{Q_w^2}{Q_u^2 + Q_v^2 + Q_w^2}$. Finally, the projected prefactors are shown in Fig.3.25. As one can see, those prefactors vary significantly for each h and energy. As a consequence, this will directly affect the observed intensities.

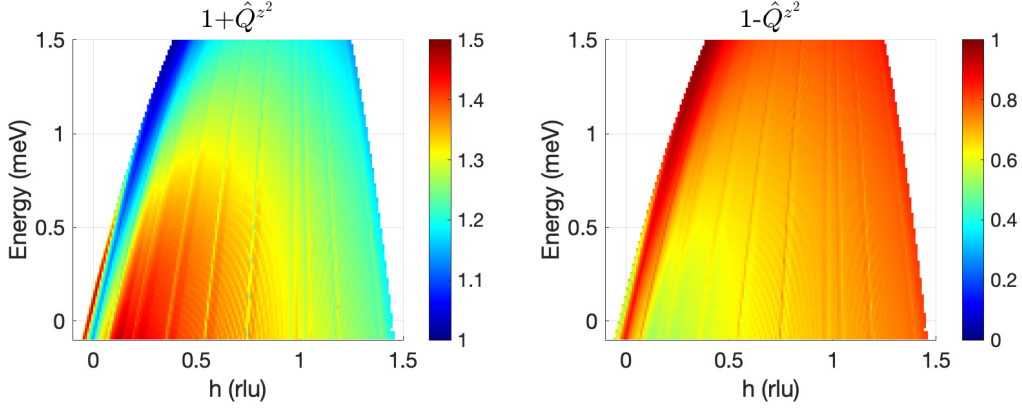
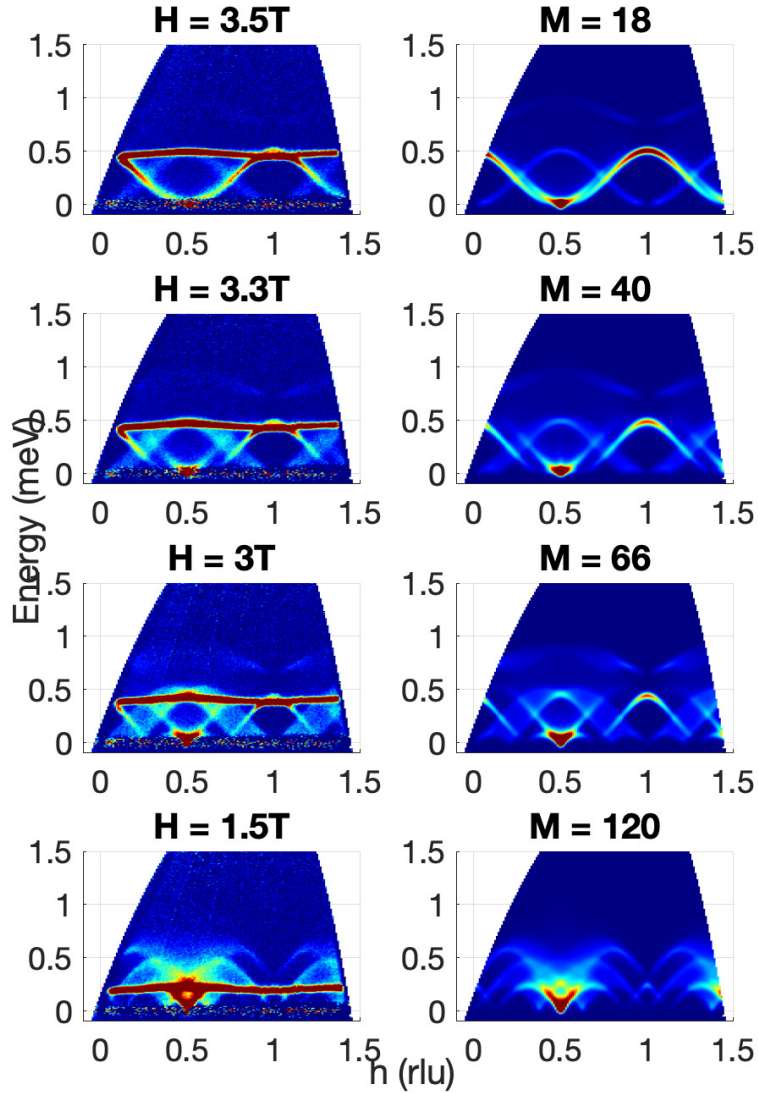


FIGURE 3.25

Colormaps of the projected prefactors $(1 + \hat{Q}^{z^2})$ (left) and $(1 - \hat{Q}^{z^2})$ (right).

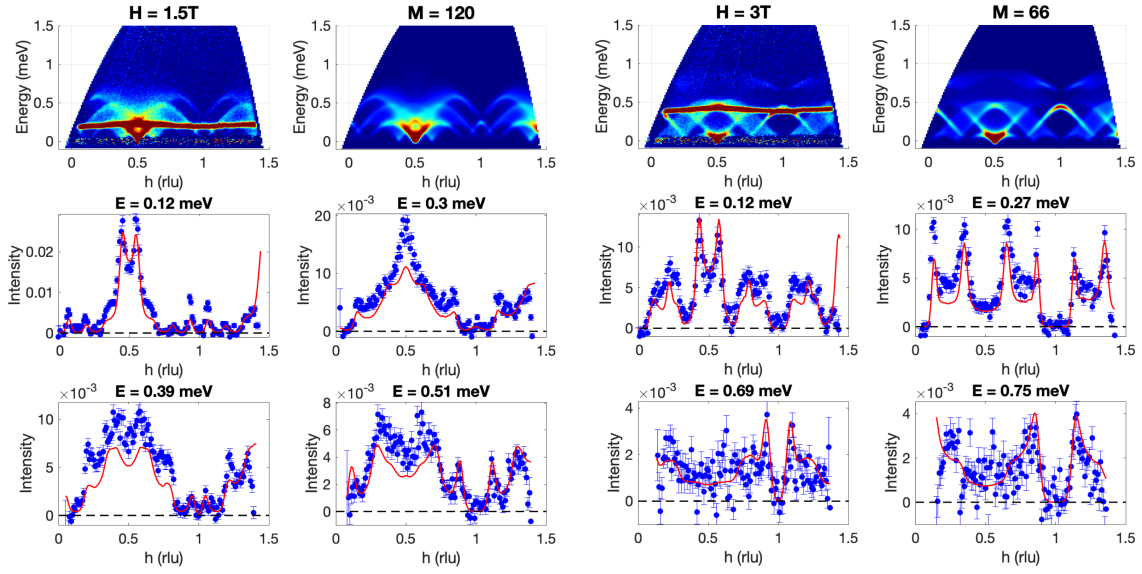
3.3.10 COMPARISON WITH THEORY

The colormaps of experimental dynamical structure factors and corresponding theoretical calculations indicated in the fourth column of Table 3.1 are shown in Fig.3.26. One can see that except for the dispersion-less flat paramagnetic mode, the results are in a great qualitative agreement, so that all the main features are well captured in the experimental data. As the field is lowered and the density of spin down particles increases, we observe a splitting of the cosine mode as well as an appearance of a new mode at higher energies ($E \approx 0.8$ meV), which comes from Bethe ansatz string solutions. The gap between two-strings and incommensurate mode reduces with decreasing the field, as well as the contribution from $S^{zz}(h, \omega)$ and $S^{-+}(h, \omega)$ channels start to be more pronounced.


FIGURE 3.26

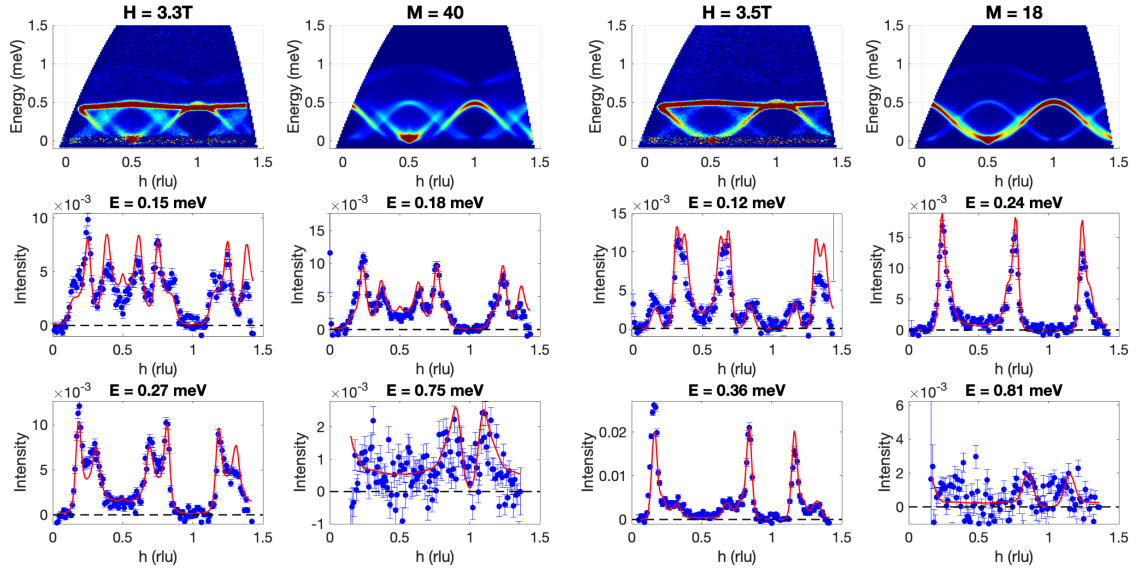
Experimental dynamical structure factors (*left column*) and corresponding Kohno's theoretical calculations (*right column*).

Now we move to the quantitative analysis of the observed scattering. In order to have a consistency with zero-field dynamics, we have applied Caux amplitude A_{Caux} to all numerical data-sets. As a reminder, the theoretical calculations were convoluted with instrument resolution, as well as the prefactors shown in Fig.3.25 were applied. Below, in Fig.3.27 - 3.28], we present several constant energy cuts for each field. Blue markers correspond to the experimental data, solid red lines – scaled theory. For each field, we demonstrate the low-energy regions far enough from the paramagnetic mode, and high-energy regions where Bethe strings scattering is expected.


FIGURE 3.27

Constant energy cuts for $H = 1.5$ T *left* and $H = 3$ T *right* and its comparison with corresponding theoretical calculations.

From the first glance, it may be seen (Fig.3.27 *left*) that the applied amplitude A_{Caux} is systematically underestimated, and is not sufficient to describe the experimental intensities for $H = 1.5$ T, although the high-energy features are perfectly described by the theory. The reason to that is clear and small discrepancies in peak positions at $H = 1.5$ T of the incommensurate modes are related to the fact that we are comparing data with "real" magnetization value $M \approx 123$ with theory calculated for $M = 120$. Apart from that, the ratio between $S^{+-}(h, \omega) + S^{-+}(h, \omega)$ and $S^{zz}(h, \omega)$ seems to work quite well, and no additional parameter is required. The experimental data reproduce all the features presented in the theoretical data, including sometimes non-trivial peak shapes. For the higher fields (Fig.3.27 *right* and Fig.3.28), the agreement is indeed perfect, meaning that Kohno's consideration of up to 4-spinon states plus Bethe strings saturates the sum rules as good as does Caux [48] at zero field, so that by 99%.


FIGURE 3.28

Constant energy cuts for $H = 3.3$ T *left* and $H = 3.5$ T *right* and its comparison with corresponding theoretical calculations.

To have a better overview of those high energy excitations represented by two- and three-strings solutions, we present constant momentum transfer cuts in Fig.3.29. To gain the statistics, we have integrated over a certain Q range. Solid lines correspond to theoretical calculations integrated in the same way. One can see that by increasing the field, string excitations shift in energy, and starting from $H = 3$ T the string continua is well separated from the low-energy psinon (antipsinon) pair excitations. As well as we can observe, that increasing the magnetic field, while the energy increases, the spectral weight is gradually vanishes. Overall, the experimental results are in a very good qualitative and quantitative agreement with Bethe-ansatz calculations.

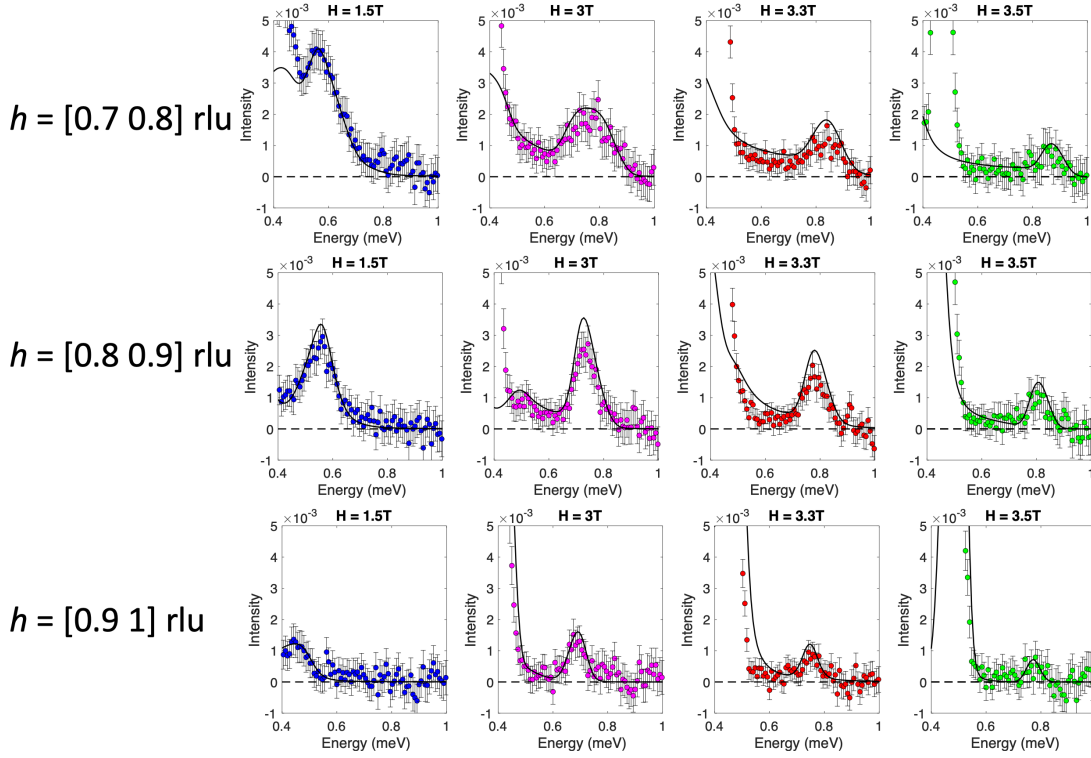


FIGURE 3.29

Constant momentum transfer cuts integrated along selected h regions for intermediate applied magnetic fields.

3.4 POLARIZATION ANALYSIS

As stated in Section 2.1.3, polarization analysis helps to distinguish scattering terms with respect to their structural and/or magnetic origins. Despite the results demonstrated in a previous Section 3.3, the intriguing scattering from Bethe-strings remains very weak (Fig.3.30) and, for some fields, overlaps with the other multi-particle continua since we were working with unpolarized neutrons, where the total cross-section is a sum of all contributions S^{+-} , S^{-+} and S^{zz} . Therefore, we are interested in distinguishing those parts and having a more detailed picture of the dynamics in the Heisenberg spin-1/2 chain. The experiments presented in this Section were performed prior to this thesis [29] and have been reanalyzed in the thesis. For the experiment with vertical field and polarization analysis, we present the comparison with theoretical calculations. For the experiment with horizontal field in half-polarized mode, we subtracted paramagnetic mode contribution assuming anisotropic g -tensor and compared with theory provided by [52] for $S^{+-}(k, \omega)$ and $S^{-+}(k, \omega)$ dynamical structure factors.

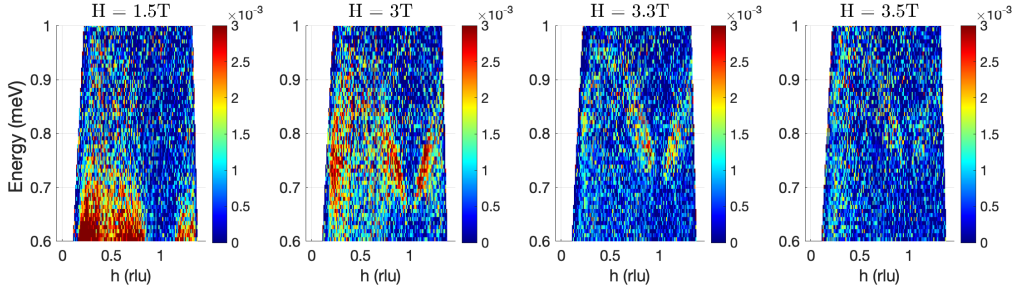
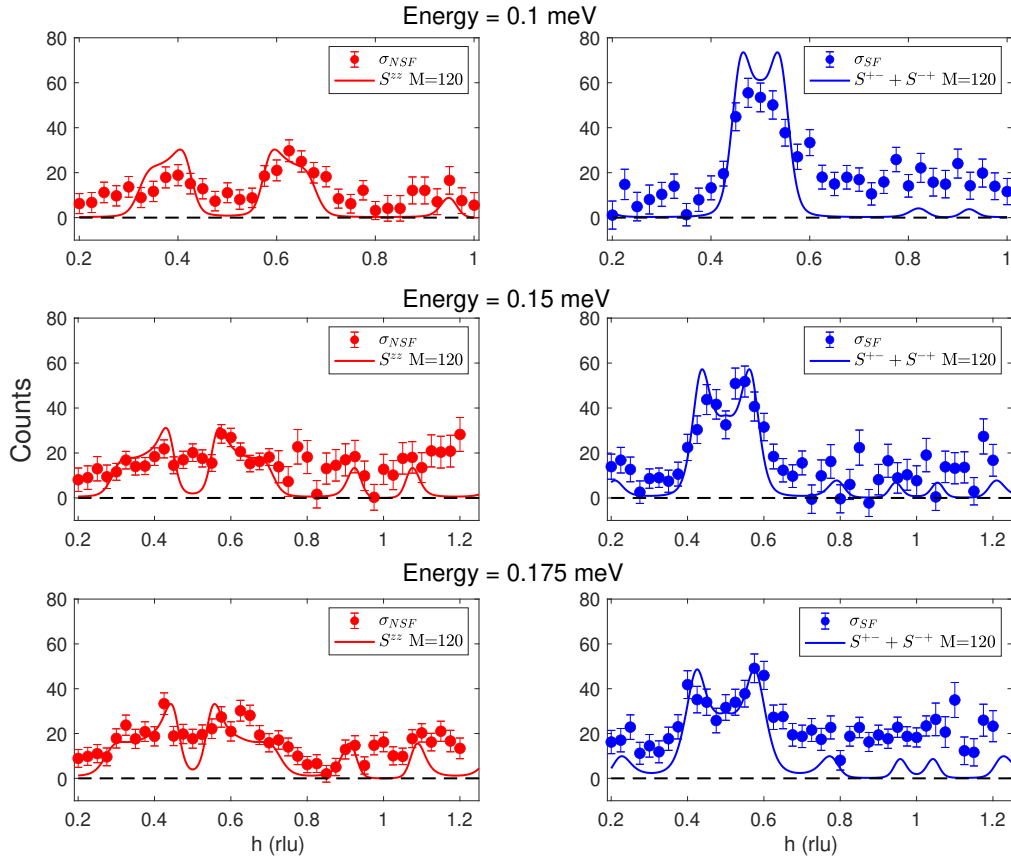


FIGURE 3.30
Bethe strings observed in IN5@ILL experiment.

3.4.1 VERTICAL MAGNETIC FIELD

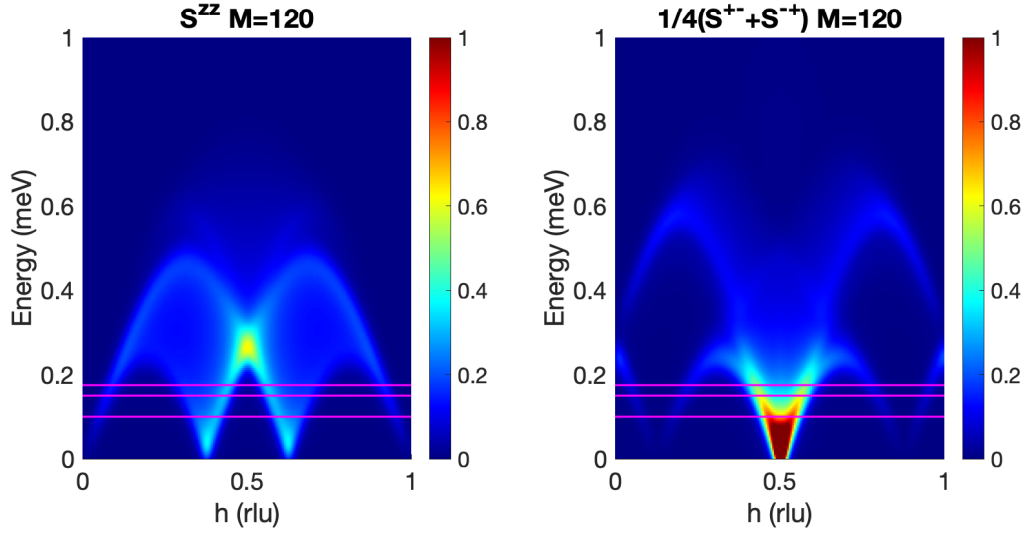
By applying vertical magnetic field together with polarization analysis, one can distinguish longitudinal and transverse excitations, so that with flipper off one measures $\sigma^{\bar{z}z} \propto \frac{1}{4}(S^{+-} + S^{-+}) + \text{spin-incoherent}$, and with flipper on one obtains $\sigma^{zz} \propto S^{zz} + \text{spin-incoherent}$. The experiment was performed at triple-axis spectrometer IN14@ILL, and the sample was mounted on a Cu-holder with triclinic axes $(1 - 1 - 1)$ and $(1 0 0)$ in the scattering plane. All measurements were carried out at $T \approx 0.42$ K in the CEA 12T magnet equipped with a dilution stick.

We present here (Fig.3.31) the results of the measurements for $H = 1.7$ T vertical magnetic field. For this field, the paramagnetic mode is observed at $E \approx 0.25$ meV so that the constant energy scans were performed at $E = 0.1, 0.125$, and 0.175 meV. The background was subtracted separately for each channel σ_{NSF} and σ_{SF} and for each constant energy according to the data measured at $H = 7$ T, where the magnon dispersion is observed for the high-energy region so that the low-energy region is free of excitations. We have compared those constant energy scans with $M = 120$ data (Fig.3.32) convoluted with an energy resolution of FWHM $45 \mu\text{eV}$ obtained from the vanadium measurements, convoluted with momentum transfer resolution $\sigma_h = 0.01$ rlu, and multiplied with the same scale factor for all energies and polarization channels. We chose theoretical calculations corresponding to $M = 120$ based on a previous TOF experiment, where for vertical $H = 1.5$ T, the estimated value was $M = 123$. At lower fields, the magnetization curve does not change rapidly as for the fields close to saturation, as shown in Fig.3.20. Therefore, since in this experiment the value of the vertical field was $H = 1.7$ T so that the closest theoretical M value would be $M = 120$.


FIGURE 3.31

Longitudinal (*red*) and transverse (*blue*) cross-sections measured with applied vertical field $H = 1.7$ T at different energies $E = 0.1, 0.15, 0.175$ meV (from top to bottom). The corresponding solid lines show theoretical calculations for $M = 120$.

Even though we are limited to a low-energy region, all data is in good agreement with Bethe-ansatz calculations. In the S^{zz} channel, one clearly observes two distinct branches, which extrapolate to $0.5 - h_{inc}$ and $0.5 + h_{inc}$ at zero energy transfer related to the incommensurate modes. Moreover, at higher energies, one can notice clear evidence of the psinon-antipsinon continuum. In the spin-flip channel, at higher energies, two intensive branches can be seen, which are indistinguishable at $E = 0.1$ meV.


FIGURE 3.32

$S^{zz}(h, \omega)$ (left) and $\frac{1}{4}(S^{+-}(h, \omega) + S^{-+}(h, \omega))$ (right) obtained by Kohno for $M = 120$. Magenta solid lines correspond to the constant energy cuts that have been measured during the experiment.

The experimental data cover all even low-intensity features of the theoretical spectrum. Moreover, the theoretical M-value seems to be very close to the "real" one, which corresponds to $H = 1.7$ T. Therefore, we can update the previous magnetization curve (Fig.3.24) by including $H = 1.7$ T data point in Fig.3.33. The resulting point (green marker) tends to follow the overall trend.

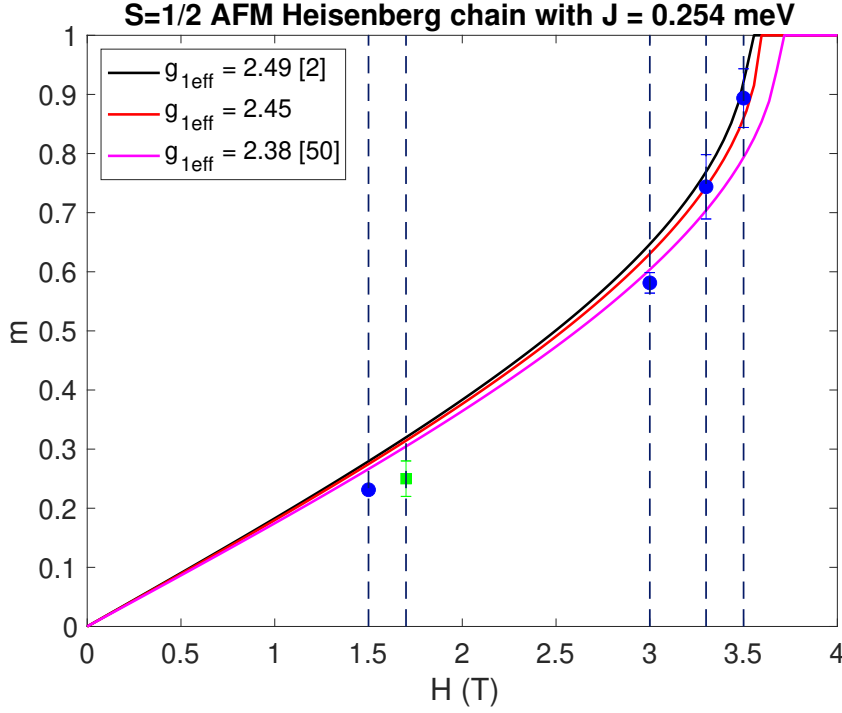


FIGURE 3.33

Magnetization curve obtained from IN5@ILL experiment (blue markers) and IN14@ILL experiment with vertical field geometry (green marker). Solid lines correspond to Müller's approximation given in [44] for different g -tensors.

3.4.2 HORIZONTAL MAGNETIC FIELD

In this last section, we review the results of horizontal field experiment. The aim of this experiment is to distinguish between S^{+-} and S^{-+} transverse excitations and therefore trace the polarization of Bethe-strings. This can be done by applying the magnetic field in the scattering plane $\mathbf{H} \parallel \mathbf{Q}$. The experiment was performed on triple-axis spectrometer IN14@ILL using the half-polarized mode, so that the beam was polarized before scattering on the sample and the polarization of the scattered neutrons was not analyzed. Therefore, the measured cross-sections are $\sigma_{x0} \propto S^{-+} + \text{spin-incoherent}$ and $\sigma_{\bar{x}0} \propto S^{+-} + \text{spin-incoherent}$. The measurements were done at dilution temperature $T = 0.1$ K, allowing direct comparison of experiment and calculations.

While applying the magnetic field in the scattering plane, one has to face the fact that the effective magnetic field changes for each \mathbf{Q} value since the g -tensor is anisotropic [61]. In vertical field geometry, $|\mathbf{g} \cdot \mathbf{H}|$ remains constant for each \mathbf{Q} . According to 3.7, we can calculate effective horizontal g -tensor for each Cu^{2+} magnetic system as follows: $g_{1(2)hor} = |\mathbf{g}_{1(2)} \cdot \hat{\mathbf{H}}_{\parallel \mathbf{Q}}|$, where $\hat{\mathbf{H}}_{\parallel \mathbf{Q}}$ is a unitary magnetic field vector parallel to the scattering plane. Constant energy scans were performed at $H = 1.7$ T and $H = 3.4$ T horizontal magnetic fields with varying $h = [-0.5..1.2]$ rlu in $\mathbf{Q} = (h, -1/2, -1/2)$.

The effective horizontal g -tensor for both copper sites is shown in Fig.3.34 *left*. As one can see, for a given momentum transfer range, effective g -tensor changes significantly, giving bandwidth of $\Delta g_{1hor} = 0.0569$ for chain Cu_1^{2+} ions, and $\Delta g_{2hor} = 0.2448$ for isolated Cu_2^{2+} ions. To evaluate how this tensor variation will affect the magnetic Cu_1^{2+} chain subsystem and determine which theoretical calculations we should compare experimental data-sets, it is more convenient to rewrite Eq.3.8 in terms of M -value:

$$M(H) = 160 - \frac{320}{\pi} \arcsin \left(\frac{\mu_B}{2J} g_{1hor} H \right). \quad (3.10)$$

We present the obtained (according to Eq.3.10) M -curve for the chain Cu_1^{2+} ion assuming the minimal $g_{1hor}^{min} = 2.0796$ and maximal $g_{1hor}^{max} = 2.1365$ horizontal g -tensors in Fig.3.34 *right*. As ticks on the M -axis, we have specified available theoretical calculations; for the H -axis, we have indicated the measured horizontal magnetic fields. The average of a horizontal g -tensor for Cu_1^{2+} magnetic system is $g_{1hor}^{av} = 2.1080 \pm 0.0285$. The variation of 1.4% from the average value leads to overall variation of M -value $\Delta M \approx 5$ for $H = 3.4$ T, and $\Delta M \approx 1$ for the lower field $H = 1.7$ T. Therefore, if theoretical M -value is close enough to the experimental M -value, at $H = 1.7$ T we will not see any variation in \mathbf{Q} due to anisotropic g -tensor. Most likely that we will not see any difference at $H = 3.4$ T too since in the TOF experiment we observed very small discrepancies at $H = 1.5$ T where $\Delta M = 3$, and indeed the resolution of IN5@ILL is better than it was at IN14@ILL. According to the available theory calculations, experimental $H = 1.7$ T magnetic field is closer to the theoretical $M = 120$ value, whereas $H = 3.4$ T magnetic field is closer to $M = 66$.

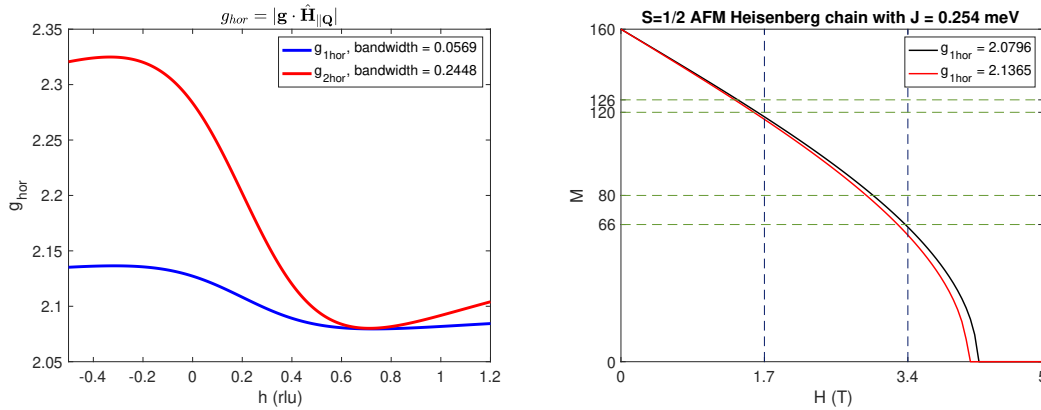


FIGURE 3.34

Left: Variation of an effective horizontal g -tensor for two copper magnetic subsystems when magnetic field is parallel to the scattering plane; *right:* field dependent M -value for maximal and minimal horizontal g -tensors for chain Cu_1^{2+} ions. Vertical lines correspond to the measured fields; horizontal lines correspond to the available theoretical calculations.

DATA PREPARATION

Before proceeding to the comparison of experimental data with theoretical calculations, it is necessary to make several corrections. In order to reduce the influence of the strong paramagnetic mode, the scans with constant energy transfer were performed. However, as we saw in the previous Section 3.3, the residuals of the paramagnetic still could be present in those spectra. Moreover, its effective g -tensor variation with \mathbf{Q} is not negligible compared to chain Cu_1^{2+} ions (Fig.3.34 *left*) and must be taken into account in the following calculations. With linear spin-wave theory, one can exactly calculate the magnon dispersion in the fully polarized state. We have reproduced the linear spin-wave calculations in SpinW [33] as they were previously reported in [49], applying $H = 5$ T magnetic field perpendicular Fig.3.35 *left* and parallel Fig.3.35 *right* to the scattering plane. The exchange parameters were taken as $J_a = 0.254$ meV, $J_{12} = -0.02$ meV, $J_{22} = -0.012$ meV, $J_b + J_c = 0.004$ meV as they are shown in Fig.3.5. The anisotropic g -tensor from [61] was taken into account for two inequivalent copper positions. Cosine-dispersion corresponds to the magnon dispersion of the chain Cu^{2+} ion, and the flat mode corresponds to the paramagnetic contribution.

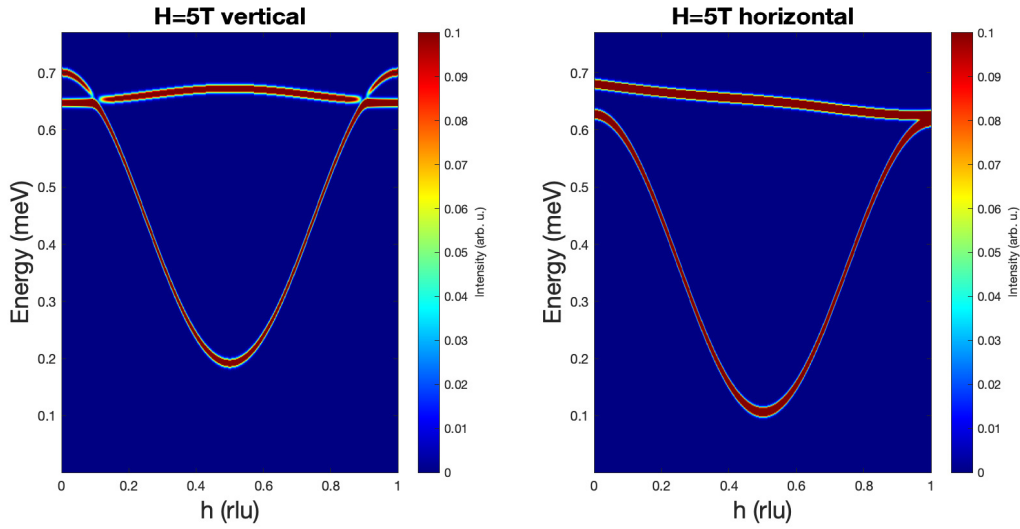


FIGURE 3.35

Intensity maps of the theoretical magnon dispersion in fully polarized state with vertical (*left*) and horizontal (*right*) magnetic field of $H = 5$ T. Exchange parameters were taken from [49]. A finite arbitrary energy resolution of FWHM = 0.01 meV has been applied.

As was expected, the energy-momentum relation of the paramagnetic modes changes drastically in the horizontal field geometry and has to be taken into account in further analysis. Since the chain mode has its lowest energy at $h = 0.5$ rlu, we are able to distinguish between chain and paramagnetic modes as they are well separated. For this purpose, constant h -scans have been performed at $h = 0, 0.5$, and 1 rlu Fig.3.36 *left* with $H = 3.4$ T horizontal magnetic field

applied. At those Q values, one can observe a sharp peak feature together with the incoherent scattering. We have fitted the tail of the incoherent scattering with Voigt function (solid green line in Fig.3.36 *left*) using only $h = 0$ and $h = 1$ rlu data-sets since $h = 0.5$ rlu data-set contains chain-mode scattering at lower energies as expected Fig.3.35. The result of the incoherent scattering subtraction is shown in Fig.3.36 *right*. We have fitted the peak at $h = 0.5$ rlu scan with Voigt function (solid blue line). At $h = 0(1)$ rlu (Fig.3.35 *right*), the chain and paramagnetic modes have almost the same energy (exactly the same energy) so that in the experimental data, we observe only one broadened peak with higher amplitude. We have fixed the amplitude and width of the $h = 0.5$ rlu Voigt function, and then fit $h = 0$ and $h = 1$ rlu with two Voigt functions the results of which are shown with red and blue solid lines, respectively. As one can see, both contributions are well described, so that we can use those parameters for the paramagnetic mode description in the following.

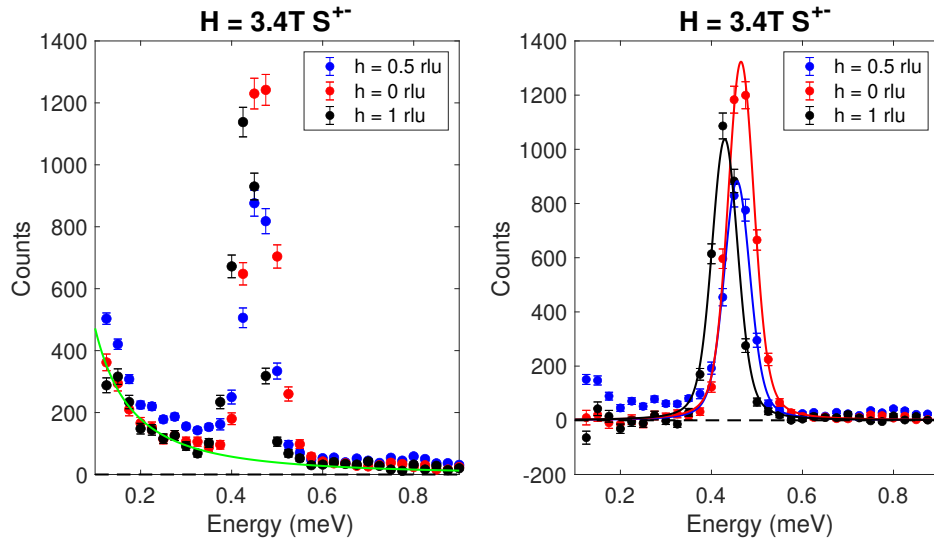
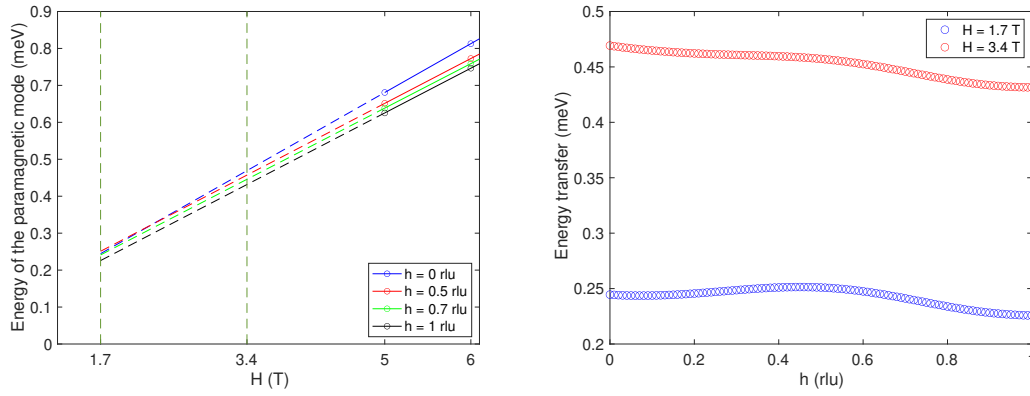


FIGURE 3.36

Left: Constant h -scans measured in horizontal magnetic field $H = 3.4$ T in spin-flip channel. Solid green line represents the fit of the incoherent tail; *right:* same h -scans with incoherent scattering subtracted. Solid lines show the fitting of the magnetic signal, as explained in the text above.

Using linear spin-wave theory with the same exchange and anisotropy parameters, we performed calculations for different horizontal field values in order to obtain the field dependence of the paramagnetic mode energy. The results of those calculations are shown in Fig.3.37. As one can notice, for different h values, the corresponding $E(H)$ dependence is perfectly linear, allowing to extrapolate those curves to $H = 1.7$ T and $H = 3.4$ T magnetic fields for each h independently in order to obtain the paramagnetic mode energies.


FIGURE 3.37

Left: Energy-field $E(H)$ dependence for paramagnetic mode at different h values in $\mathbf{Q} = (h, -1/2, -1/2)$ obtained from LSWT. Vertical dashed lines indicate experimental $H = 1.7$ T and $H = 3.4$ T horizontal field values; *right:* dispersion of the paramagnetic mode at $H = 1.7$ T and $H = 3.4$ T obtained by extrapolation of linear spin-wave calculations.

In addition, from the fitting with Voigt functions in Fig.3.36, we were able to obtain the peak positions for the corresponding chain and paramagnetic modes. To summarize, we present in Table 3.2 the fitted positions of two modes with Voigt function (2nd and 3rd columns) and extrapolated positions from the LSWT (4th column). We also present the energy difference between fits and calculations in column 5. Overall, the discrepancies with calculations are less than 1%, and will not be taken into account in the following.

h (rlu)	E (meV) para	E (meV) chain	E (meV) para expected	Δ (meV) para
0	0.47(1)	0.462(6)	0.4693	0.0007
0.5	0.456(2)	—	0.4572	0.0012
1	0.4294(1)	0.4294(2)	0.4317	0.0023

TABLE 3.2

Energy of the paramagnetic and chain modes obtained from the fitting (Fig.3.36) with Voigt function for different h values in columns 2 and 3 respectively. Expected energy values for paramagnetic mode obtained from by extrapolation of LSWT results in column 4. The difference between fitted energy and expected energy is specified in column 5.

As was shown in Fig.3.34, the bandwidth of the effective horizontal g -tensor for the isolated Cu atoms is 0.2448. Its averaged value $g_{2hor}^{av} = 2.2025 \pm 0.1224$. Therefore, if one uses the averaged value, it will explicitly provide 5% uncertainty in energy determination. For this reason, in the following we will keep anisotropic g -tensor for Cu^{2+} isolated ions.

COMPARISON WITH THEORY

In Fig.3.38, we present dynamical structure factors $S^{-+}(h, \omega)$ and $S^{+-}(h, \omega)$ for $M = 120$ (top) and $M = 66$ (bottom) together with LSWT calculated paramagnetic mode contribution, which appears only in $S^{+-}(h, \omega)$. In addition, by solid magenta lines we indicated the constant energy scans that have been performed during the experiment in order to see how big could be the influence of the paramagnetic mode. For $M = 120$, which corresponds to $H = 1.7$ T, the h -scan with energy $E = 0.3$ meV is very close to the paramagnetic mode, which could affect the observed intensities due to uncertainties explained above. Apart from the paramagnetic mode subtraction and incoherent scattering, no corrections were applied to the data, neither multiple scattering correction nor magnetic form-factor correction.

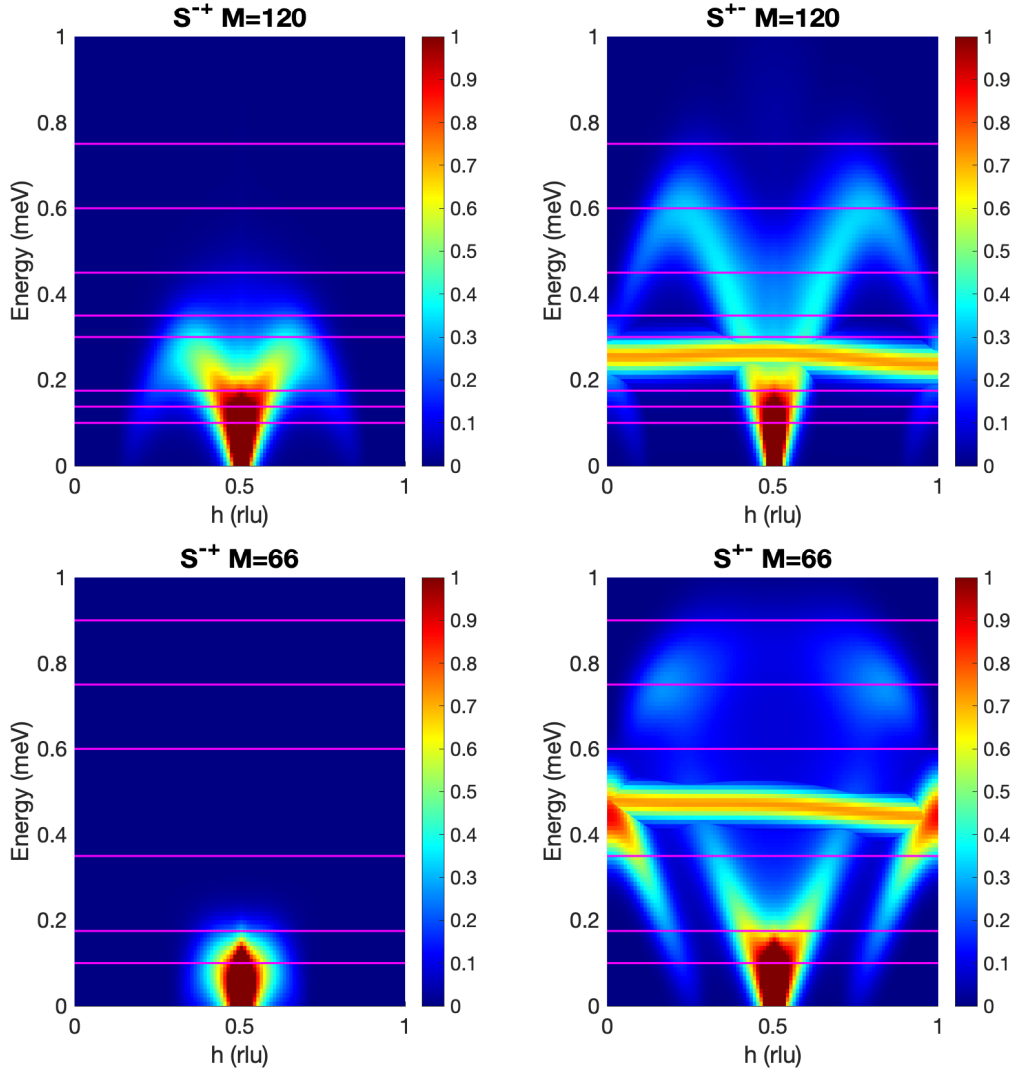


FIGURE 3.38

Dynamical structure factors $S^{-+}(h, \omega)$ and $S^{+-}(h, \omega)$ obtained by Kohno for $M = 120$ and $M = 66$. In addition, we have added paramagnetic mode scattering to the spin-flip polarization channel.

The results of comparison are shown in Fig.3.39 – 3.40 for $H = 1.7$ T, and in Fig.3.41 – 3.42 for $H = 3.4$ T. We have convoluted theoretical spectra with finite energy $\sigma_\omega = 0.034$ meV and momentum transfer $\sigma_h = 0.01$ rlu resolution and multiplied it with the same amplitude for both fields in order to match the experimental data. As was expected for $H = 1.7$ T, anisotropic g -tensor of Cu_1^{2+} chain ions does not affect the observed experimental data a lot so that all sharp features are quite symmetric in h . For $H = 3.4$ T, it is hard to judge since the constant energy scans are "shorter" in h in addition to obvious peak position discrepancies between calculations and experiment, which is most likely related to a slightly different M -value. High-energy region $E \geq 0.6$ meV of S^{+-} dynamical structure factor (in which we are mostly interested in this experiment) is well captured for both horizontal fields displaying two-string excitations. For lower energies in both channels, the quantitative agreement is quite good. Unexpected discrepancies are observed at $E = 0.3$ meV for both channels at $H = 1.7$ T. Most likely, this is related to the paramagnetic mode since the constant energy scans were performed very close to the paramagnetic mode (Fig.3.38), and therefore slightly different value of a horizontal g -tensor for Cu_2^{2+} will affect this energy region a lot.

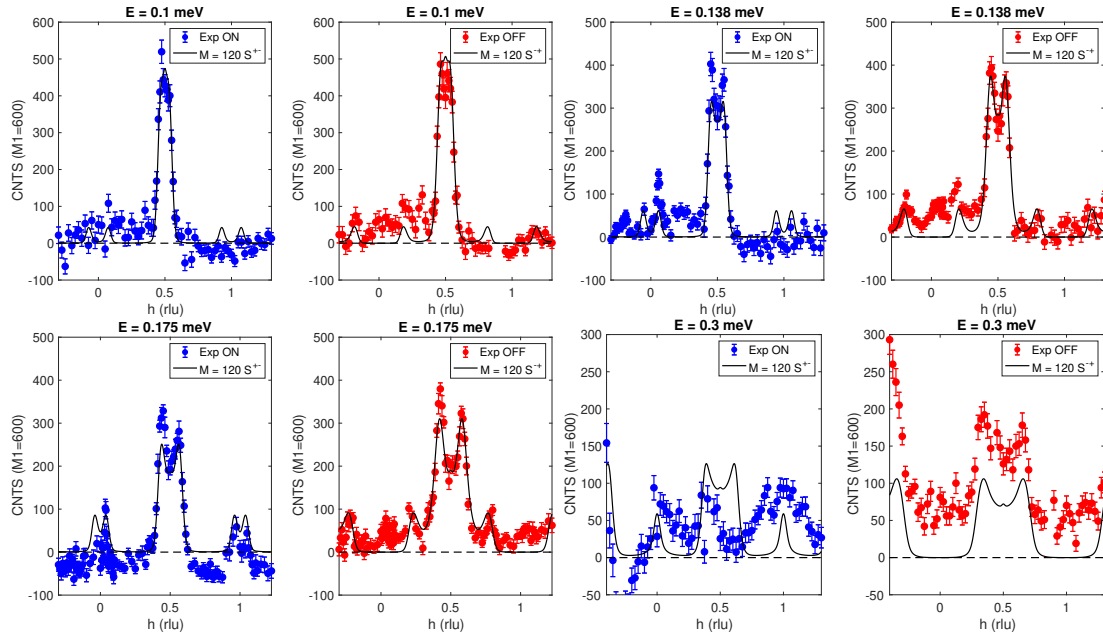
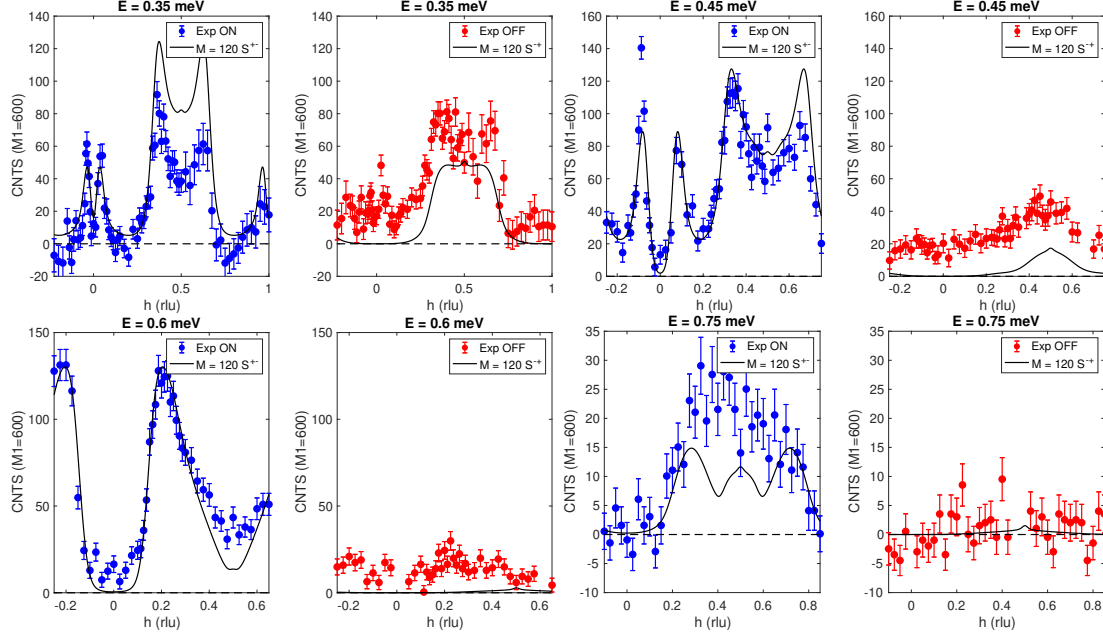
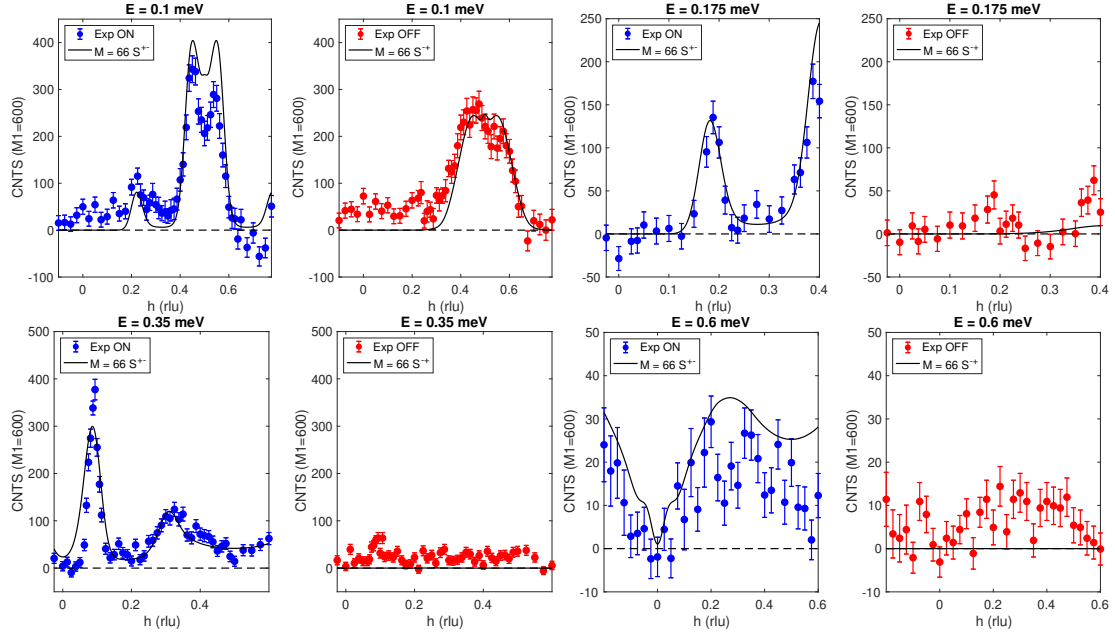


FIGURE 3.39

Comparison of $H = 1.7$ T $S^{+-}(h, \omega)$ and $S^{+-}(h, \omega)$ constant energy scans with theoretical $M = 120$ dynamical structure factors.


FIGURE 3.40

Comparison of $H = 1.7 \text{ T } S^{+-}(h)$ and $S^{+-}(h)$ constant energy scans with theoretical $M = 120$ dynamical structure factors (continuation).


FIGURE 3.41

Comparison of $H = 3.4 \text{ T } S^{+-}(h)$ and $S^{+-}(h)$ constant energy scans with theoretical $M = 66$ dynamical structure factors.

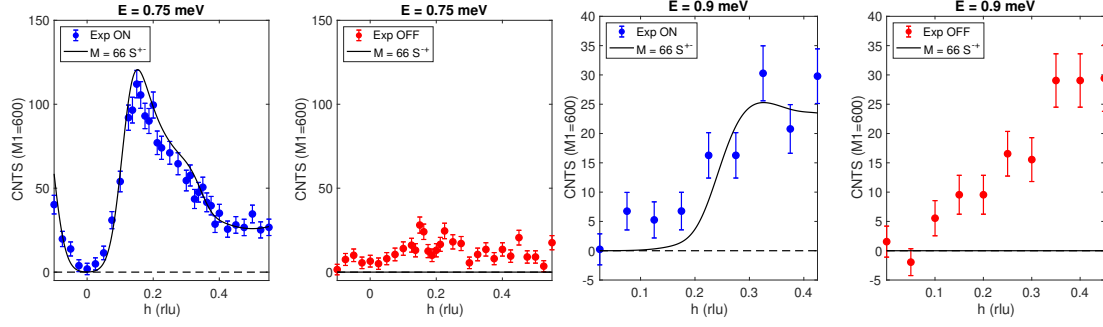


FIGURE 3.42

Comparison of $H = 3.4 \text{ T } S^{+-}(h)$ and $S^{+-}(h)$ constant energy scans with theoretical $M = 66$ dynamical structure factors (continuation).

3.5 SUMMARY

This chapter mainly focused on quantitative data analysis of the field-dependent dynamics features in $\text{CuSO}_4 \cdot 5\text{D}_2\text{O}$. Together with polarization analysis, we were able to observe excitations from the new quasiparticles, like psinons, antipsinons, and Bethe strings. We showed a qualitatively and quantitatively great agreement with the Bethe-ansatz calculations, thus confirming that $\text{CuSO}_4 \cdot 5\text{D}_2\text{O}$ belongs to the model example of one-dimensional spin-1/2 Heisenberg chain.

The incommensurate modes were already observed in copper benzoate [47], azurite [62], and $\text{BaCu}_2\text{Si}_2\text{O}_7$ [63]. However, the observed excitations were not fully described with Heisenberg $S = 1/2$ antiferromagnetic spin chain model due to additional interactions. For CPC [64] and pyrazine [46] the comparison between Bethe-ansatz calculations and experiment was demonstrated in [52]. However, due to the large values of main exchange coupling, the higher energy regions have not been studied. For $\text{BaCo}_2\text{V}_2\text{O}_8$ [54] and $\text{SrCo}_2\text{V}_2\text{O}_8$ [53], recent studies have presented observation of Bethe-strings and psinon continua. However, these materials belong to XXZ Heisenberg-Ising $S = 1/2$ spin chain antiferromagnets with $\Delta \approx 2$. Moreover, due to the additional interactions present in the $\text{SrCo}_2\text{V}_2\text{O}_8$, the corresponding theoretical Bethe lineplots do not agree with experimental data perfectly.

In addition, we have presented an first experimental verification of the polarization (chirality) of Bethe strings, and contrary to [65], polarization analysis was applied to study excitations in a longitudinal magnetic field. The results are in perfect agreement with Bethe-ansatz calculations that include solutions up to $2\psi 2\psi^*$, which are equivalent to two- and four-spinon continuum in zero field, and saturate sum rules by 99%.

CHAPTER 4

QUANTUM NATURE OF MAGNETIC EXCITATIONS IN $\text{Cu}_6[\text{Si}_6\text{O}_{18}] \cdot 6\text{H}_2\text{O}$

The gemstone mineral green diopside, $\text{Cu}_6[\text{Si}_6\text{O}_{18}] \cdot 6\text{H}_2\text{O}$, crystallizes in the space group $R\bar{3}$. Hexagonal rings of silica tetrahedra interconnect the magnetic Cu^{2+} ions with spin-1/2. The Cu^{2+} are surrounded by axially-elongated oxygen octahedra. The copper-oxygen network forms corner-sharing spirals along the hexagonal three-fold c -axis, where neighbouring coppers are displaced by $c/3$. The spiral chains have a honeycomb arrangement in the ab -plane.

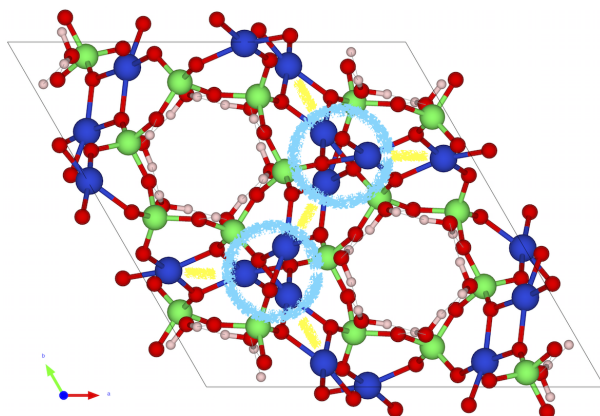


FIGURE 4.1

Projection of the structure of green diopside along the hexagonal c -axis (blue Cu, green Si, red O, rose H). The Cu spiral chains along c are encircled in light blue, the interchain bonds are indicated in yellow [66],[67].

4.1 A SEA OF CONFLICTS

Numerous studies such as bulk susceptibility [68],[69], specific heat [70],[71], neutron diffraction [67] and NMR [72] point to an unfrustrated quasi-one-dimensional Heisenberg antiferromagnetic chain behaviour with the intrachain exchange of 74 K, and smaller ferromagnetic interchain coupling. In specific heat measurements, a sharp λ -anomaly was observed at $T_N = 14.5$ K, indicating the onset of long-range magnetic order. It contains only 2% of the entropy expected for the ordering of a $S = 1/2$ spin system. The AFM spin ordering with propagation vector $\mathbf{k} = (0, 0, 3/2)_{hex}$ at T_N has been confirmed by an unpolarized single-crystal neutron diffraction study [67]. The ordered Cu^{2+} moment was refined to $0.55(1) \mu_B$ at 1.5 K, which is significantly lower theoretical value of $M = gS = 1\mu_B$ for $S = 1/2$. Nearest Cu^{2+} spins within the spirals in c direction are inclined in the opposite direction by 13° with respect to the c -axis, while the ordering within hexagonal ab -plane remains ferromagnetic (FM) [67].

Recent neutron time-of-flight experiment [73] provided some clarity on the size and sign of exchange interactions, the question about which arose in the works [74] and [75]. The inelastic spectra [73] were modelled with linear spin-wave theory of a strictly collinear magnetic structure with antiferromagnetic nearest-neighbour interaction $J_c = 10.6(1)$ meV, ferromagnetic interchain coupling $J_{ab} = -1.2(1)$ meV and easy axis anisotropy on every Cu^{2+} ion $A = 0.14(1)$ meV shown in Fig.4.2. Larger bandwidth was observed for longitudinal excitations, reflecting $J_c > J_{ab}$. The observed spin-wave gap was reproduced by introducing single ion anisotropy term in Heisenberg Hamiltonian:

$$H = J_c \sum_{\langle i,j \rangle_c} \mathbf{S}_i \cdot \mathbf{S}_j + J_{ab} \sum_{\langle i,j \rangle_{ab}} \mathbf{S}_i \cdot \mathbf{S}_j - \sum_i A S_i^z{}^2. \quad (4.1)$$

The origin of anisotropy might be related to Jahn-Teller distortion [67], however difficult to reconcile with the small ordered moment. Moreover, the observed experimental spectra are extremely broadened and cannot be explained by the instrumental resolution.

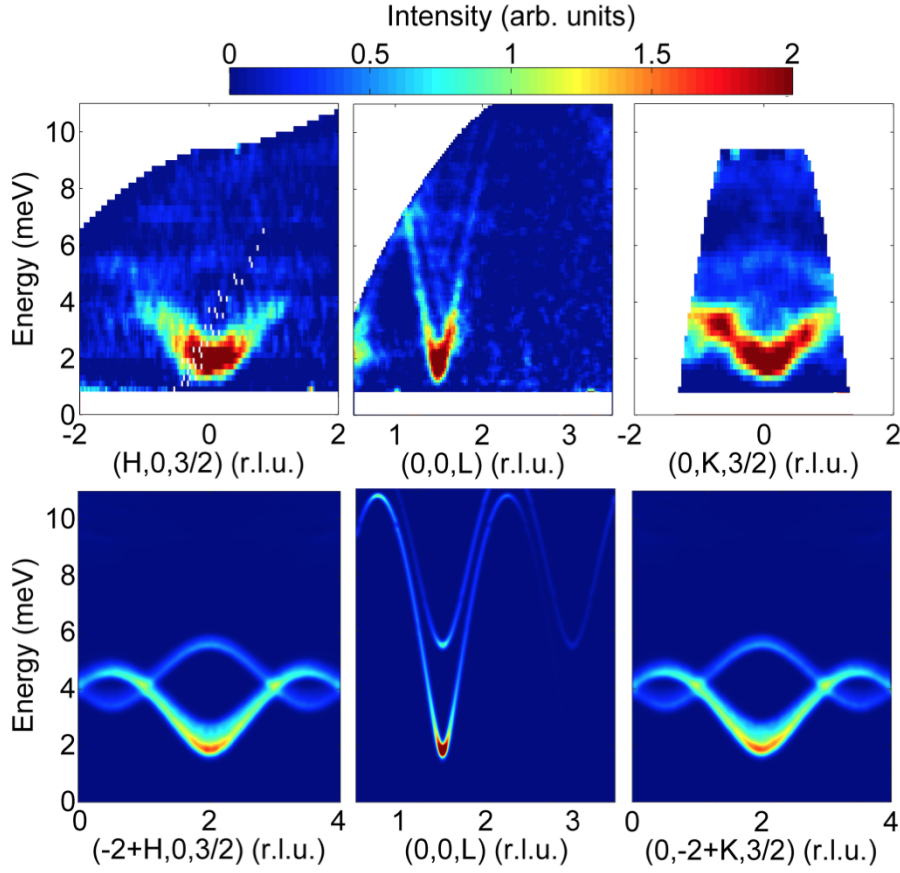


FIGURE 4.2

Top: Inelastic neutron spectra measured at time-of-flight CNCS@SNS in diopside at $T = 1.7$ K, showing the dispersion of magnetic excitations along high-symmetry directions. *Bottom:* LSWT calculations, based on the model Hamiltonian 4.1 convoluted with instrumental resolution. Adapted from [73].

To summarize, the ground state of green diopside proposed in [73] represents by spiral AFM spin chains along the hexagonal c -axis with ferromagnetic interchain coupling, which is supported by [75] and [72] and disagrees with [74], where AFM coupling between the chain was proposed. Their magnetization value obtained from LSWT yields $0.38 \mu_B$, which is not far from the value obtained in the diffraction study [67]. Overall, they attribute the reduced magnetic moment to quantum fluctuations of copper spins, which arise due to the low coordination number [75]. In contrast, muon studies [76] evidenced no quantum criticality above or below T_N . Instead, they propose only a three-dimensional Heisenberg coupling scheme below T_N .

Inspired by all the above contradictions, the first thing we did was LSWT calculations (Fig.4.3) based on the model in [73] with the inclination of a magnetic moment, which was observed in [67]. We have used exchange parameters as $J_c = 10.6(1)$ meV, $J_{ab} = -1.2(1)$ meV and $A = 0.14(1)$ meV and a collinear magnetic structure with a propagation vector $\mathbf{k} =$

$(0, 0, 1.5)$ for the left column in Fig.4.3. We define the direction of the magnetic moment \mathbf{m} as $m_x = \sin(\Theta) \cos(\phi)$, $m_y = \sin(\Theta) \sin(\phi)$, $m_z = \cos(\Theta)$, where Θ is an inclination of the magnetic moment from the c -axis, and ϕ – its orientation in ab -plane. For the last three figures, $J_c = 10.6(1)$ meV, $J_{ab} = -1.2(1)$ meV, and different directions of the magnetic moment were used. In addition, on each copper site, single ion anisotropy was introduced in accordance with the magnetic moment direction. However, the larger value of anisotropy was needed $A = 1$ meV in order to stabilize the ground state. Obviously, the deviation from the collinear spin ordering strongly affects the calculated inelastic scattering spectra, and more intriguing, it can lead to the broadening of the inelastic features observed in [73]. Therefore, an accurate determination of a magnetic structure would be our first task.

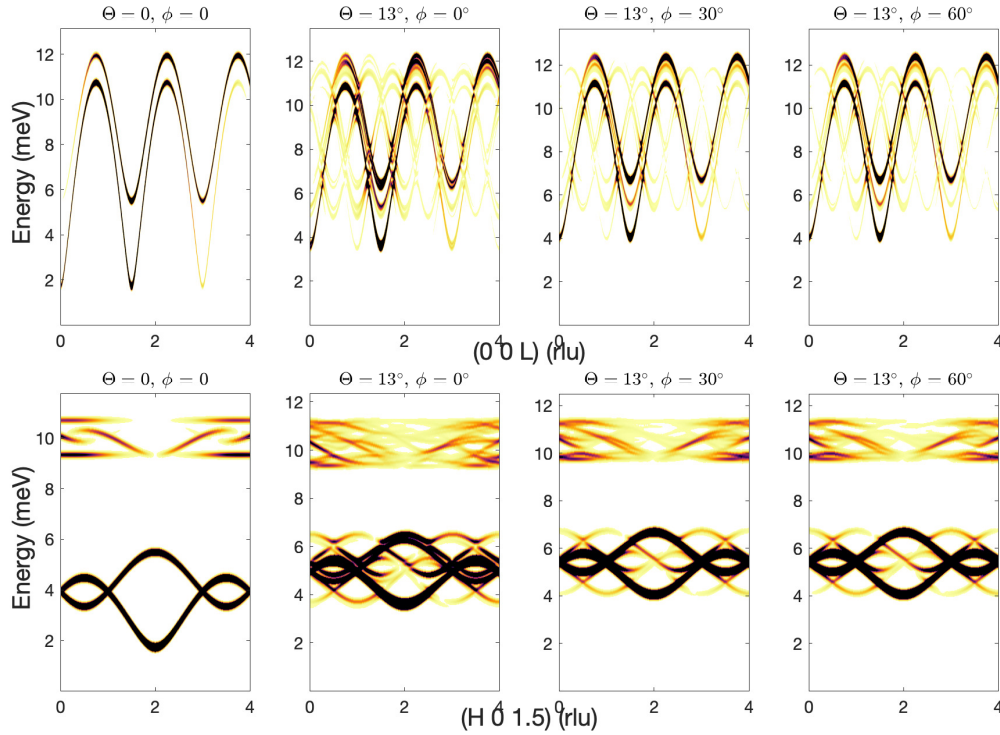


FIGURE 4.3

LSWT calculations for a model Heisenberg Hamiltonian from [73]. The first column of figure reproduces the calculations from [73] with non-inclined magnetic moments. Other figures represent excitations considering the tilt of 13° from the c -axis reported before by [67]. For the tilted configuration, different orientations of the magnetic moment in ab -plane are presented by changing ϕ -angle, the larger value of $A = 1$ meV was used.

4.2 MAGNETIC STRUCTURE DETERMINATION

SYMMETRY ANALYSIS

The crystallographic unit cell contains eighteen Cu^{2+} ions, which are all equivalent to the general 18f Wyckoff position in $R\bar{3}$ space group. The magnetic structure determined in [67] below T_N

can be described with propagation vector $\mathbf{k} = (0, 0, 1.5)$. Group representation theory can be used to identify the possible magnetic structures. According to symmetry analysis in BASIREPS [21], for the propagation vector \mathbf{k} and the space group $R\bar{3}$ there are six irreducible representations, including four with imaginary part $\Gamma_3, \Gamma_4, \Gamma_5$, and Γ_6 . Moreover, Γ_5 and Γ_6 are equivalent to Γ_3 and Γ_4 representations with the complex conjugate operation. Table 4.1 represents the symmetry relations for magnetic moments transformations for coupled Cu-ions inside the unit cell. In addition, since the interaction scheme is clear [73] [75], we conclude that Γ_1 should be sufficient to describe the magnetic structure, and we will use that in the following.

Atom	Symmetry	Γ_1	Γ_2	Γ_3	Γ_4
Cu_1	(x, y, z)	(u, v, w)	(u, v, w)	(u, v, w)	(u, v, w)
Cu_2	$(-y, x - y, z)$	$(-v, u - v, w)$	$(-v, u - v, w)$	$(v, -u + v, -w)$	$(v, -u + v, -w)$
Cu_3	$(-x + y, -x, z)$	$(-u + v, -u, w)$	$(-u + v, -u, w)$	$(u - v, u, -w)$	$(u - v, u, -w)$
Cu_4	$(-x, -y, -z)$	(u, v, w)	$(-u, -v, -w)$	(u, v, w)	$(-u, -v, -w)$
Cu_5	$(y, -x + y, -z)$	$(-v, u - v, w)$	$(v, -u + v, -w)$	$(v, -u + v, -w)$	$(-v, u - v, w)$
Cu_6	$(x - y, x, -z)$	$(-u + v, -u, w)$	$(u - v, u, -w)$	$(u - v, u, -w)$	$(-u + v, -u, w)$
In chain		AFM	AFM	FM	FM
Between the chains		FM	AFM	FM	AFM

TABLE 4.1

Irreducible representations and their symmetry operations according to the space group $R\bar{3}$ and propagation vector $\mathbf{k} = (0, 0, 1.5)$. The parameters u, v , and w are free parameters which are to be determined experimentally. The corresponding exchange interactions within and between chains are indicated in the two bottom rows.

POLARIZATION ANALYSIS WITH CRYOCRADLE

We have performed spherical neutron polarimetry (SNP) on the spin-polarized hot neutron diffractometer D3@ILL with a monochromatic and polarized neutron beam of wavelength $\lambda = 0.85 \text{ \AA}$. The CRYOPAD was used together with the Cryocradle setup in order to have access to several scattering planes. The sample was mounted with (hhl) scattering plane. The UB-matrix was determined according to the observed nuclear Bragg peaks. The nine channels of the polarization matrices at base temperature $T = 1.5 \text{ K}$ were obtained by measuring the initial and final neutron polarization after the scattering process. The standard local coordination system has been employed, where x is parallel to the scattering vector \mathbf{Q} , z is the vertical direction of the diffractometer, and y completes the right-handed coordination system). The final neutron polarization was analyzed using a ^3He spin filter, whose efficiency was tested regularly by measuring the P_{xx} element of a nuclear Bragg reflection $(1, 1, 0)$. The observed data were corrected for the time-dependent spin filter efficiency, and the initial neutron polarization of $p_0 = 0.91$ was taken into account for all calculations. For the selected magnetic Bragg peaks,

three points were measured: one at the top of the peak, and two others on opposite sides of the peak, which determined the background level.

For the refinement, five peaks in total were used, the choice of which was due to their intensity compared to the background. We present the results of the experiment in Table 4.2. On the left, one can see the measured polarization matrices for the specific \mathbf{Q} vectors. In addition, the experimental integrated intensity in counts is specified. We have refined polarization matrices with Mag2Pol software [77] assuming Γ_1 irreducible representation symmetry operations in order to obtain the inclination of the magnetic moment. The refined magnetic moment yields $\mathbf{m} = (0.017(2), -0.068(8), 0.997(1))$, and, in the right column of the table below, we present calculated polarization according to the obtained magnetic moment. Nonzero P_{yx}, P_{zx} channels could indicate the presence of magnetic chirality. However, in our case, they are most likely zero, especially considering the errorbars. Overall, the experimental data show a good agreement within the framework of Γ_1 irreducible representation, what also confirmed by a value of $\chi^2 = 8.40$.

Measured				Calculated		
$\mathbf{Q} = (0, 2, -0.5), I_{exp} = 1375$						
-0.88(2)	0.06(2)	-0.00(2)		-0.91	0	0
-0.067(2)	0.76(2)	0.38(2)		0	0.82	0.39
-0.01(2)	0.34(2)	-0.79(2)		0	0.39	-0.82
$\mathbf{Q} = (-1, 2, 1.5), I_{exp} = 445$						
-0.76(4)	0.01(4)	0.07(5)		-0.91	0	0
-0.04(5)	0.88(5)	0.09(5)		0	0.90	0.13
0.01(5)	0.09(5)	-0.71(5)		0	0.13	-0.90
$\mathbf{Q} = (2, -2, -0.5), I_{exp} = 2578$						
-0.87(1)	0.03(1)	0.00(1)		-0.91	0	0
0.02(1)	0.73(1)	-0.47(1)		0	0.76	-0.49
0.00(1)	-0.47(1)	-0.71(1)		0	-0.49	-0.76

$\mathbf{Q} = (2, -7, -1.5), I_{exp} = 207$						
-1.1(1)	0.12(9)	-0.1(1)		-0.91	0	0
0.04(9)	0.7(1)	0.2(1)		0	0.90	0.15
0.18(9)	0.3(1)	-1.0(1)		0	0.15	-0.90
$\mathbf{Q} = (2, -5, -0.5), I_{exp} = 345$						
-1.04(3)	0.02(3)	0.01(3)		-0.91	0	0
0.02(3)	0.85(3)	0.12(3)		0	0.91	0
0.02(3)	0.14(3)	-1.08(3)		0	0	-0.91

TABLE 4.2
Results of D3 experiment

From the D3 experiment, the refined value of a magnetic moment corresponds to a 5° tilt from the c -axis. We have calculated spin-wave spectra for tilted structure (Fig.4.4) for the same \mathbf{Q} directions as in [73]. We have used the following parameters: $J_c = 10.6(1)$ meV, $J_{ab} = -1.2(1)$ meV and $A = 0.14(1)$ meV and $\mathbf{m} = (0.017, -0.068, 0.997)$. Single ion anisotropy was applied on each copper spin in accordance with its direction, which is determined by Γ_1 irreducible representation. The calculated spectra show no evidence of additional mode splitting. Moreover, there is no hint for the broadening observed in [73].

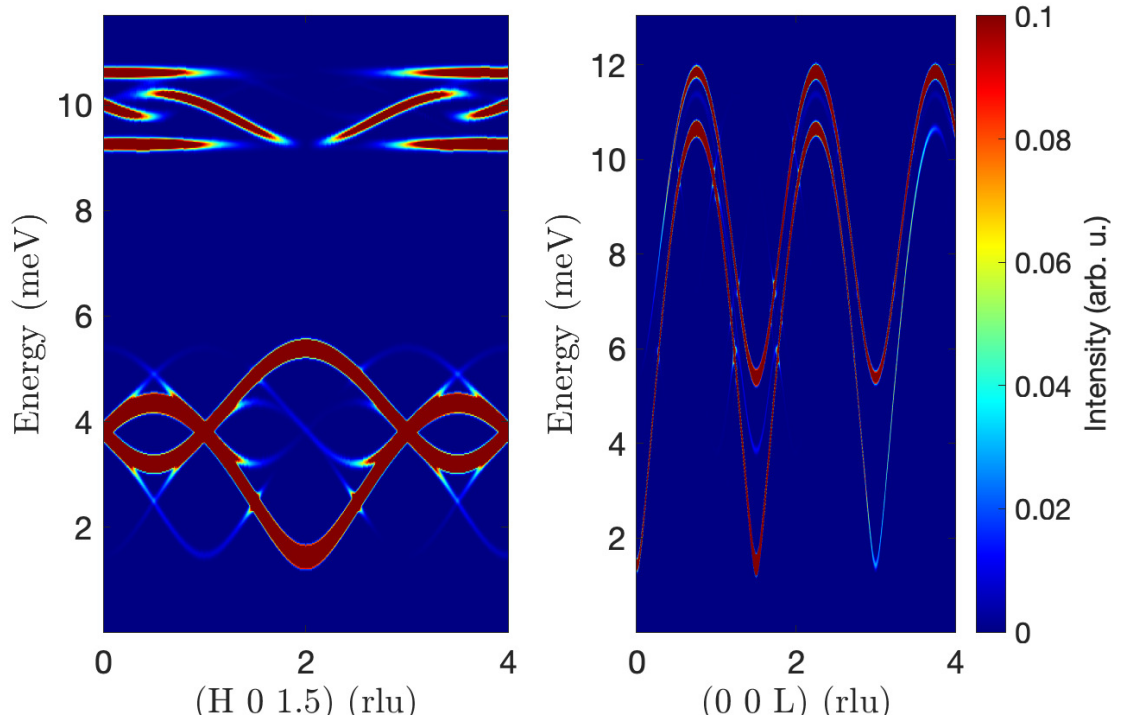


FIGURE 4.4
LSWT calculations for a model Heisenberg Hamiltonian from [73] taking into 5° tilt of the magnetic moment.

4.3 MAGNETIC EXCITATIONS IN ORDERED STATE

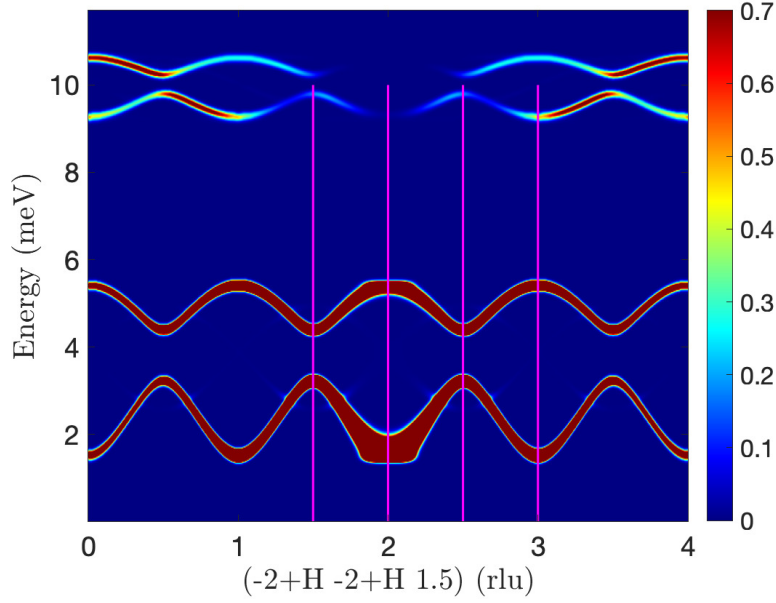
To verify that additional scattering observed in [73] is of magnetic origin, we performed a polarized inelastic ThALES@ILL experiment.

The spectrometer was used with Helmholtz coils in order to perform XYZ polarization analysis. Polarized neutrons were produced and analyzed by a horizontally focused Heusler(111) monochromator and analyzer with $k_f = 1.5 \text{ \AA}^{-1}$. No collimation was used. The sample was mounted with (hhl) scattering plane. The measurements were carried out below T_N at base temperature $T = 1.5 \text{ K}$ of a standard Orange cryostat.

With a linear combination of different spin-flip (SF) and non spin-flip (NSF) cross-sections, one can obtain a pure magnetic scattering free of any background:

$$|\mathbf{M}_\perp|^2 = \sigma_{NSF}^{yy} + \sigma_{NSF}^{zz} - 2\sigma_{NSF}^{xx} = 2\sigma_{SF}^{xx} - \sigma_{SF}^{yy} - \sigma_{SF}^{zz}. \quad (4.2)$$

In order to understand which scans we have to perform, we did LSWT calculations for a given scattering plane and applied finite energy $\Delta E = 0.13 \text{ meV}$ and momentum transfer $\Delta Q = 0.01 \text{ rlu}$ resolution, the results of which is shown in Fig.4.5. As for magnetic structure, we used spin directions according to the moment obtained in the D3 experiment and Γ_1 irreducible representation. For the exchange parameters and anisotropies, we have used $J_c = 10.6(1) \text{ meV}$, $J_{ab} = -1.2(1) \text{ meV}$ and $A = 0.14(1) \text{ meV}$. Single ion anisotropy was applied on each copper site in accordance with its direction. Since there are two distinct branches expected at $E = 2 \text{ meV}$ and $E = 5 \text{ meV}$, we decided to perform constant \mathbf{Q} cuts in order to have an idea of an energy gap size and bandwidths for both dispersion modes.


FIGURE 4.5

LSWT calculations for a model Heisenberg Hamiltonian from [73] for (hhl) scattering plane taking into account the tilt of 5° from the c -axis. Magenta solid lines indicate the constant Q cuts measured during ThALES experiment. Finite energy resolution $\Delta E = 0.13$ meV and momentum transfer $\Delta Q = 0.01$ rlu are applied. All LSWT calculations were scaled with the same parameter A , which was chosen according to $Q = (0, 0, 1.5)$ data-set.

The results of the experiment are shown in Fig.4.6. We present only the magnetic scattering part obtained with Eq.4.2. Due to the experimental time available and magnetic scattering intensity, different data-sets were measured with different statistics as evidenced by various errorbars, although they were normalized to the same monitor. In addition, we have included LSWT calculations for each Q value obtained with the collinear structure and parameters from [73] (in green) and LSWT calculations for the tilted structure (in blue). It has to be noted that for our calculations, we have adapted single ion anisotropy value $A = 0.151$ meV to match the experimental signal with the theory. However, this adjustment worked only for the low-energy region $E \leq 3$ meV, whereas for the high-energy region, the calculations are systematically shifted in energy. Moreover, theoretical spectra obtained using exchange parameters given in [73] do not match the experimental data at all. A proper fit of exchange parameters and different types of anisotropy requires a verification of the stability of the ground state. This has not been attempted. However, on the other hand, for every Q value, we see very broad features that are not described in terms of spin-wave excitations. By including finite energy resolution $\Delta E = 0.13$ meV and momentum transfer resolution $\Delta Q = 0.01$ rlu, one naturally observes the broadening of the spectrum, however still not enough to describe the whole shape. The first thought that comes to mind since we are dealing with a quasi-one-dimensional system (we cannot exclude this since the interaction between the chains is still small compared to the main

interaction within the chain), consisting of copper $S = 1/2$ atoms, the remaining scattering can be a feature of a spinon continuum, and to prove that, we need to perform measurements above T_N . This will be a subject of the following Section.

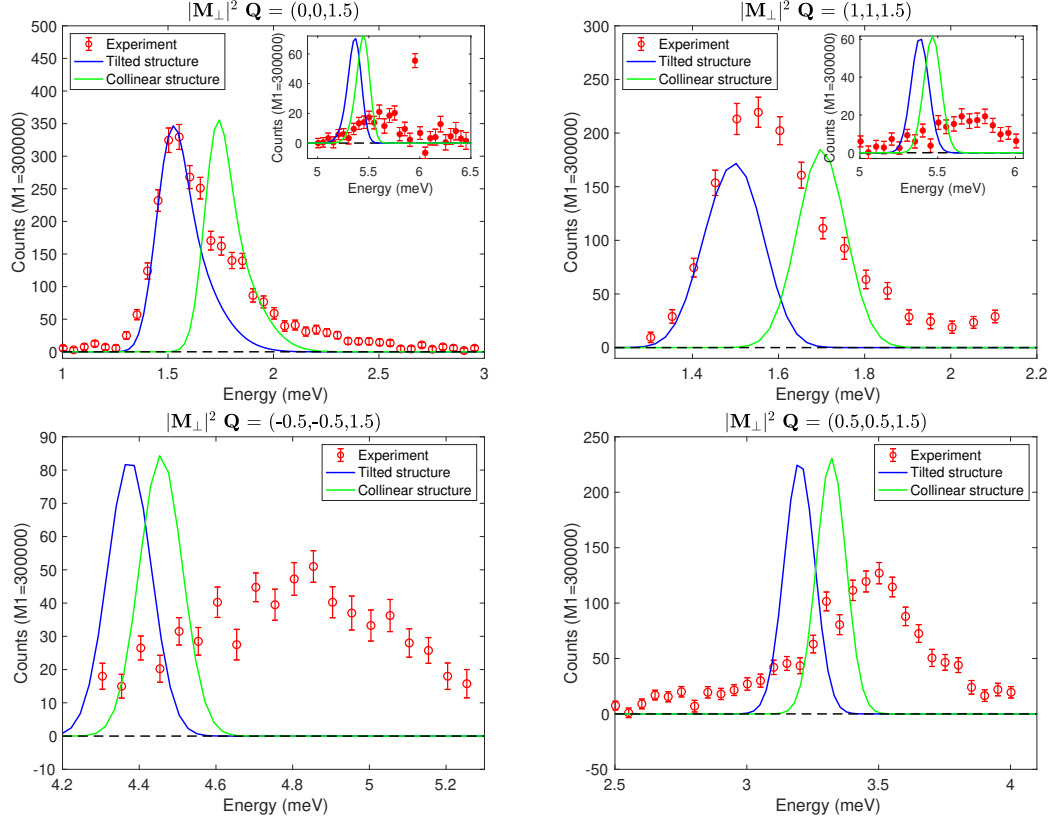


FIGURE 4.6

Experimental magnetic scattering $|\mathbf{M}_\perp|^2$ measured at different \mathbf{Q} vectors at ThALES instrument. Solid green line corresponds to the LSWT calculations according to the parameters given in [73]. Solid blue line corresponds to the LSWT calculations according to the direction of the magnetic moment obtained in D3 experiment.

4.4 EVIDENCE OF QUANTUM FLUCTUATIONS ABOVE AND BELOW T_N

In order to show that observed broad excitations could be related to spinon excitations, we have performed IN20@ILL experiment. The experimental setup was equipped with Helmholtz coils for the XYZ polarization analysis. The spectrometer was used in W configuration. The neutron energy was selected by a horizontally focusing polarizing Heusler(111) monochromator and analyzed with Heusler(111) operating at fixed $k_f = 2.662 \text{ \AA}^{-1}$. A PG(002) filter was positioned at k_f . No collimation was used. The diaphragms were placed next to the sample. The sample was mounted into the Orange Cryostat, and the data were collected at $T = 1.5 \text{ K}$ and $T = 22 \text{ K}$.

We have used the (hhl) -oriented crystal previously used for the D3 and ThALES experiments. We measured spin-flip and non spin-flip xx , yy , zz cross-sections at the constant energy transfer $E = 7$ meV. The measured spectra, together with LSWT calculations, are shown in Fig.4.7. For the exchange parameters and anisotropies, we have used $J_c = 10.6(1)$ meV, $J_{ab} = -1.2(1)$ meV and $A = 0.14(1)$ meV. For the ground state, we have used spin directions according to the magnetic moment tilt obtained in the D3 experiment and Γ_1 irreducible representation. The single ion anisotropy was applied to each copper site in accordance with its magnetic moment direction.

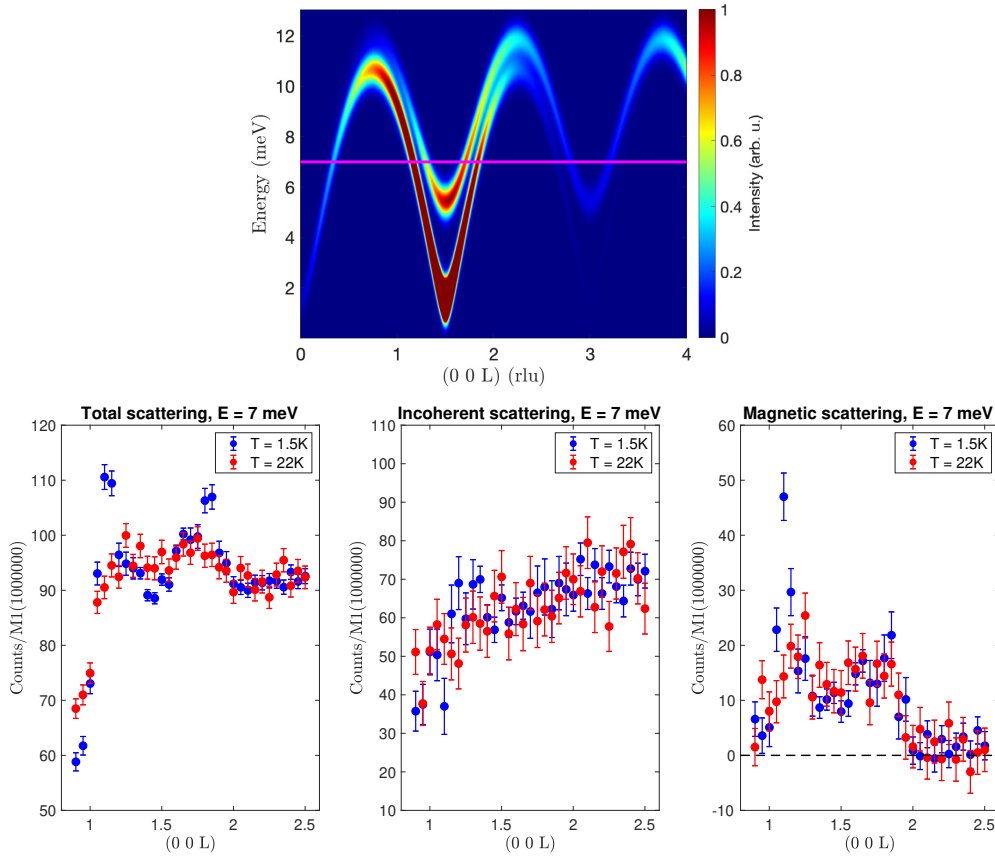


FIGURE 4.7

Top: Calculated spin-wave dispersion along $(00l)$ direction convoluted with energy $\Delta E = 1$ meV and momentum transfer $\Delta Q = 0.01$ rlu IN20 instrument resolution. *Bottom:* Inelastic spectra measured above (red) and below (blue) T_N . Three different contributions (total cross-section, incoherent cross-section and magnetic cross-section) are shown.

Since the sample contains hydrogen atoms that mainly scatter incoherently, magnetic signal makes a small contribution to total scattering, which is excellent distinguishable in experiments with polarization analysis. We see the redistributing of maximal intensity when we measure above T_N . The presence of the magnetic scattering at both temperatures near the AFM zone center $(0\ 0\ 1.5)$ and its absence above $(0\ 0\ 2)$ are not compatible with purely spin-wave excitations

and becoming a clear evidence quantum fluctuations like in [7]. Therefore, this material indeed requires further study and analysis and contrary to [76] we were able to observe quantum spin chain-like behaviour.

4.5 SUMMARY

In this chapter, we presented the first evidence of quantum fluctuations in the green mineral diopside $\text{Cu}_6[\text{Si}_6\text{O}_{18}] \cdot 6\text{H}_2\text{O}$. Despite the numerous studies about classical three-dimensional Néel antiferromagnet behaviour, we have shown by means of inelastic scattering that observed excitations are not only of "classical" spin-wave nature. We determined the magnetic structure using spherical neutron polarimetry and found an inclination of the magnetic moment of 5° from the c -axis. And given that the structure of an individual chain in the unit cell is chiral, this inclination might result, for example to a helicoidal magnetic ordering. We have to admit that a lot of analytical work is still needed, namely for resolving the exchange interaction scheme.

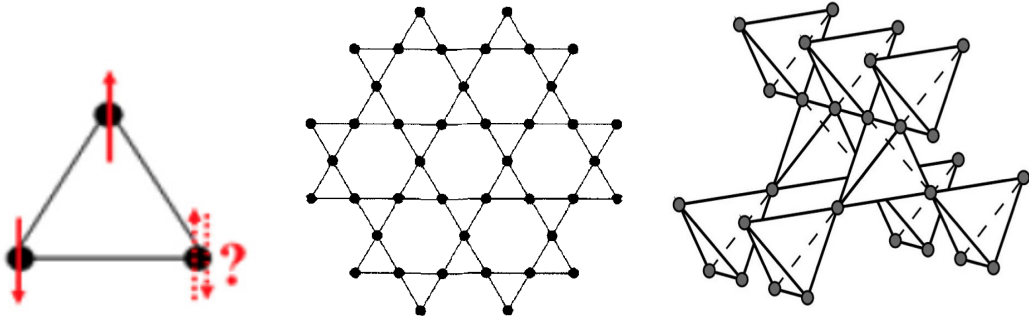
CHAPTER 5

DYNAMICS IN FRUSTRATED TRIANGULAR ANTIFERROMAGNET CuSb_2O_6

5.1 FRUSTRATION

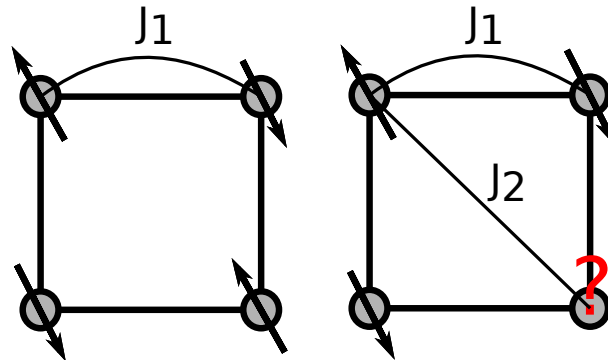
The inability of the system to satisfy all the magnetic interactions simultaneously, or in other words, the absence of a single state with minimal energy, can be related to the lattice or the competing magnetic interactions. Instead, there are variety of low-energies states realized, leading to the degeneracy of the ground state. The reason for such behaviour is frustration. The simplest realization of this effect is two-dimensional triangular lattice with only nearest-neighbour antiferromagnetic interactions (Fig.5.1 *left*). In fact, this is an example of geometrical frustration that implies the situation when a third spin cannot satisfy the condition to be antiparallel to each of its first neighbours. In this case, the system will possess the multiplicity of unsatisfied states [78].

The other example of geometrical frustration in two dimensions is the kagome lattice which is a triangular network of corner-sharing triangles, and in three dimensions – pyrochlore lattice with corner-share tetrahedra (Fig. 5.1 *middle* and *right*). These materials usually demonstrate the absence of the long-range magnetic ordering down to millikelvin temperatures and show non-trivial collective dynamics of spin fluctuations.


FIGURE 5.1

Left: Examples of geometrical frustration. *Left:* two-dimensional triangular lattice (adapted from [79]); *Middle:* two-dimensional kagome lattice (adapted from [78]); *Right:* three-dimensional pyrochlore lattice (adapted from [80])

Frustration may arise not only from the lattice geometry but from competing interactions. As an example, one can consider square lattice (Fig. 5.2) with nearest-neighbour antiferromagnetic interactions. Indeed, with only nearest-neighbour AFM interactions, the classical Néel state is realized. However, by adding AFM interactions along the diagonal bonds, the frustration arises and ultimately leads to entanglement of the ground state [81, 82].


FIGURE 5.2

Left: Frustration caused by competing interactions: square lattice. *Left:* classical Néel order, where J_1 stands for AFM interaction between neighbouring spins. *Right:* frustration on square lattice when adding another AFM interaction J_2 along the diagonals.

The same situation is observed for honeycomb lattice (Fig. 5.3). According to the Heisenberg $J_1 - J_2 - J_3$ model [83], depending on the sign and magnitude of the J_2/J_1 and J_3/J_1 ratios, nontrivial spin configurations can be realized, such as zigzag orderings, stripe orderings, various spiral structures etc.

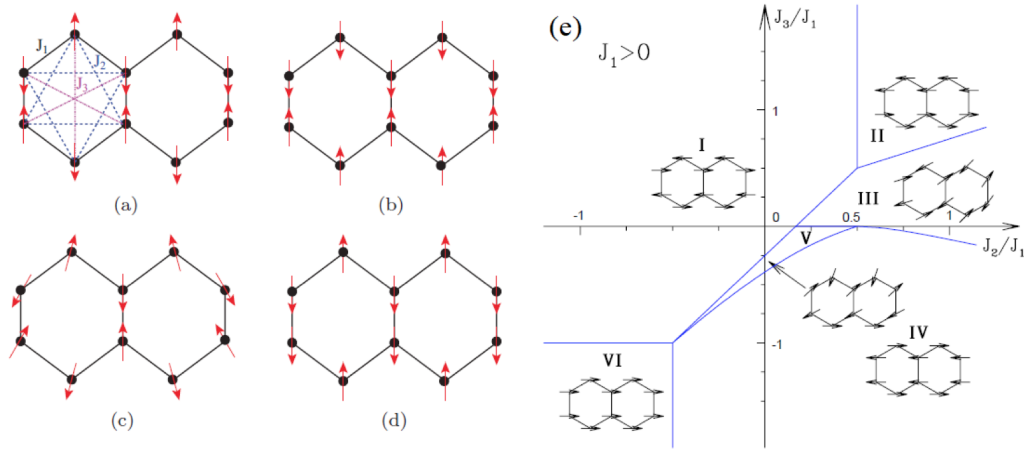


FIGURE 5.3

Left: Possible ground states for $J_1 - J_2 - J_3$ model. *a* classical Néel ordering, *b* zigzag-type structure, *c* spiral ordering, *d* stripe-type structure; *e* Phase diagram for $S = 1/2$ honeycomb structure and AFM nearest-neighbour interaction J_1 [84].

The situation of the competing interactions may be observed on the geometrically frustrated lattices. Moreover, in the real systems additional contributions to the Hamiltonian may be also important such as single ion anisotropy [85], dipolar interactions [86, 87], Dzyaloshinskii-Moriya interactions [88], magnetoelastic coupling [89], site dilution [90, 91] and exchange randomness [92]. In some cases, these terms may induce magnetic order or spin freezing.

One of the parameters which can somehow estimate the "degree" of frustration is defined as $f = |\Theta_{CW}|/T_C$, where Θ_{CW} – Curie-Weiss temperature, T_C – Néel temperature or spin freezing temperature if any. As one can see, in an ordered Néel-type magnet, the ratio f is of the order of 1, whereas for frustrated systems, f should be significantly larger given the absence of the ordered state.

With this small introduction, one can see that there is a variety of different cases in terms of frustration and its consequences. However, according to the scope of this chapter, I will consider only triangular lattices with dominant AFM interactions.

5.2 TRIANGULAR LATTICE

In order to link the lattice symmetry with the observed magnetic properties, one has to have a clear idea about the symmetry of the spin. It is essential to establish whether the spin direction is restricted and therefore has a discrete symmetry for Ising spins or continuous rotational symmetry for the Heisenberg spins.

ISING MODEL

Historically, the Ising model on the triangular net with nearest-neighbour antiferromagnetic interaction was exactly solved by Wannier [93]. The corresponding ground state is described by finite entropy at $T = 0$, and power-law decaying spin correlations with the critical exponent $\eta = 1/2$ [94] and shows the absence of any long-range magnetic order at any finite temperature. For the next 50 years, studies of the Ising triangular antiferromagnets had several trajectories. One of them was devoted to the general- S spin considerations. Numerous studies [95–99] showed that for the infinite spin $S \rightarrow \infty$ (or $S > \frac{11}{2}$ in [97]) the magnetic system tends to have an antiferromagnetic long-range order at finite temperature. In addition, the accompanying Monte Carlo simulations confirm the absence of a critical point for the spin $S = 1/2$. As the value of spin S increases and exceeds some critical value S_C , the critical exponent becomes zero, thereby confirming the presence of magnetic ordering at zero temperature. In these studies, by increasing the magnitude of spin variable S , the multiplicity of the local degrees of freedom is also increasing. The latter reduces the effect of frustration and induce the magnetic order.

Further-nearest neighbor interactions play a crucial role in this model. Depending on the next-nearest neighbor interaction sign, one can obtain different kinds of LRMO and corresponding ground state. FM coupling leads to the so-called $\sqrt{3} \times \sqrt{3}$ ordered structure, firstly demonstrated by Metcalf [100]. This structure is a three-sublattice ground state, where two sublattices have spin-up, and the third has spin down. By increasing the temperature, the system will occur first in Berezinskii-Kosterlitz-Thouless (BKT) phase [101–104], followed by high-temperature paramagnetic phase [105–108]. In contrast, next-nearest neighbor AFM interactions lead to another form of LRMO, namely to superantiferromagnetic (SAF) state where antiferromagnetically coupled spins in rows alternate [108] and no intermediate phase is expected. Both of the "unusual" ground states are demonstrated on the phase diagram Fig.5.4.

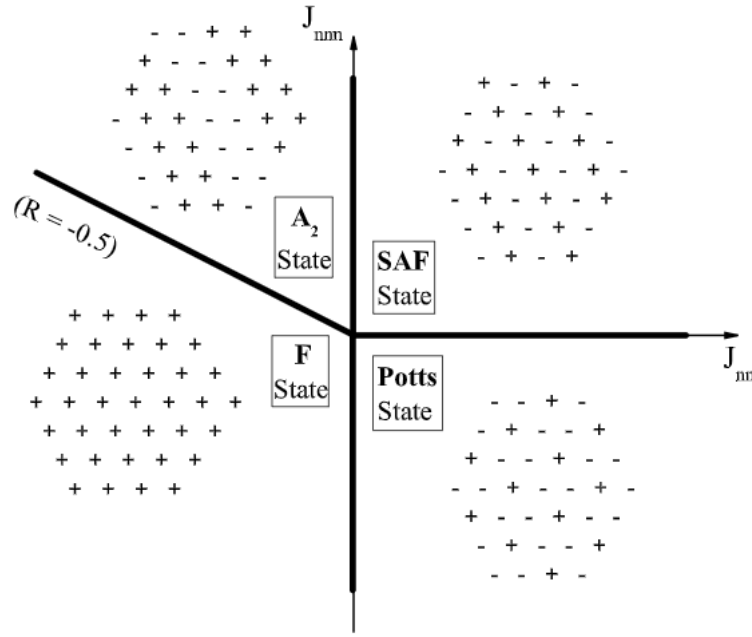


FIGURE 5.4

$T = 0$ K phase diagram of the triangular Ising model with nearest J_{nn} and next-nearest-neighbor J_{nnn} interactions. Plus "+" corresponds to the spin-down, minus "-" – spin-up. Positive values of J correspond to AFM interactions. The figure was adopted from [108]).

Although the experimental realizations of such ideal systems are extremely rare, one of the recent examples, TmMgGaO_4 , demonstrates very promising evidence [109] of BKT phase, which up to now has never been observed experimentally in 2D magnets.

XY MODEL

Increasing the symmetry of the spin, one would approach the XY model with continuous symmetry $SO(2)$. This model has attracted much interest since the 1980s due to its relevance to Josephson junction arrays in the applied magnetic field [110], helimagnetic materials [111], discotic liquid crystals [112] and many others [113].

Even though Mermin and Wagner [114] demonstrated that continuous symmetry cannot be broken for dimensions $d \leq 2$, another type of phase transition is possible – the one already mentioned and discovered independently by Berezinskii [101, 102] and by Kosterlitz and Thouless [103, 104]. This transition is not a transition in common sense since there is no local order parameter. No long-range magnetic order is expected, except the algebraic decay of the correlation function at low temperatures, leading to a quasi-long-range order associated with topological phase transition.

In contrast to the Ising-type triangular antiferromagnet, the ground state for the classical XY-model is the well-known – 120° coplanar structure. This ground state combines two types of

symmetry – continuous symmetry $U(1)$ according to the global rotation of spins, and discrete symmetry \mathbb{Z}_2 associated with chirality [115, 116]. Depending on the sense of spins rotation around each triangle (Fig. 5.5), clockwise or anticlockwise, two types of chirality are possible, which explains \mathbb{Z}_2 belonging to the Ising universality class and according to the discrete nature of \mathbb{Z}_2 symmetry, its breaking would induce long-range magnetic order.

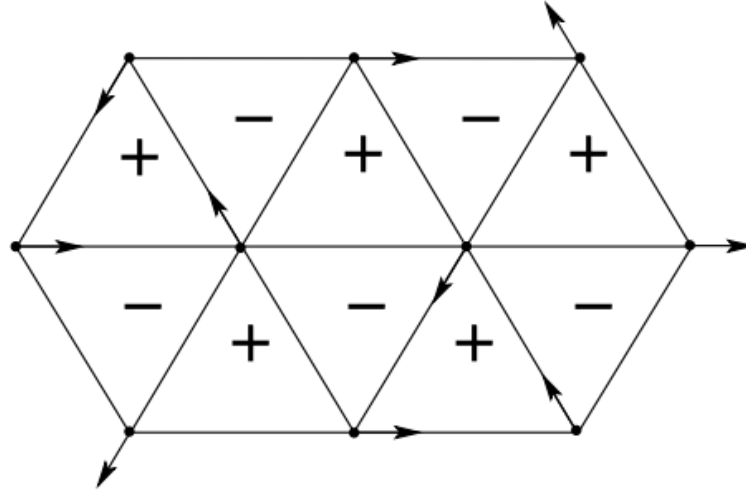


FIGURE 5.5

Ground state of the 2D antiferromagnetic XY model on the triangular lattice. Pluses "+" and minuses "-" stand for different chiralities.

As stated above, in this model, two types of symmetry can be broken through BKT phase transition and Ising-type phase transition. However, the questions about whether these transitions appear at the same temperature or they belong to one or another universality class are still under debate e.g., [117–119].

Less interest was devoted to the quantum XY model [120–123]. I would address that to the fact stated in [120] that "classical spins are really two-dimensional objects whereas the quantum spins are basically three-dimensional objects and third z spin component which is not present in the original Hamiltonian can be involved in "the low-temperature phase order" due to the commutation relations". Therefore, I will not discuss the quantum analog of the classical XY model in this thesis.

5.3 QUANTUM SPIN LIQUID CONCEPT

As for the Heisenberg system, in 1973, Philip Anderson theoretically proposed [9] an idea of the quantum spin liquid state considering the two-dimensional triangular arrangement of spins-1/2

in which neighboring spins are antiferromagnetically coupled and cause uncertainty in their directions (Fig. 2.1 *left*). In fact, this is an example of geometrical frustration, which implies the situation when a third spin cannot satisfy the condition to be antiparallel to each of its first neighbours. In the case of only nearest-neighbour Heisenberg interaction, there is a classical solution that avoids the frustration by 120° -structure realization and leads to the long-range magnetic order. Anderson suggested a resonating valence bond (RVB) model to describe the quantum state in which any two antiparallel spins pair up to form a spin singlet state with a total spin $S = 0$ and vanishing magnetic moment (Fig. 2.1 *right*). It should be noted that there is no strict arrangement of these singlets but a linear combination of all possible configurations.

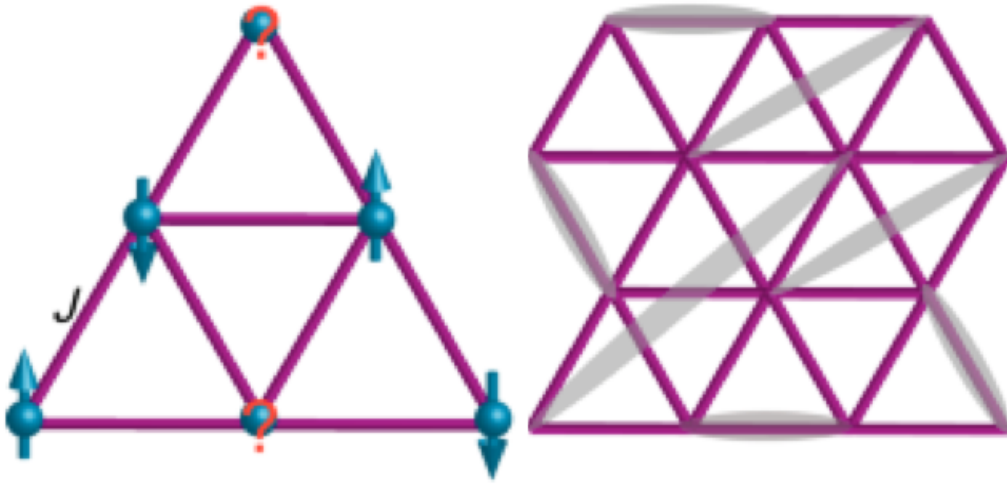


FIGURE 5.6

Left: Example of the triangular arrangement of spins. J stands for the Heisenberg exchange interaction; *Right:* Possible RVB state showing singlets with a total spin $S = 0$. Each singlet is formed by antiparallel pair of spins (the figure was adapted from [2]).

Since Anderson's work, many efforts have been done to explore deeper both theoretically and experimentally the QSL state. As for now, there are several requirements that need to be met in order to discuss this state. Small spin, absence of long-range order or spin freezing, long-range entanglement, and the associated fractional spin excitations. The main requirement for the material to be a QSL candidate is the absence of any magnetic phase transition even at $T = 0$ K. In this case, strong quantum spin fluctuations prevent any long-range magnetic order but remain the liquid-like dynamics.

This chapter presents a new potential QSL candidate, trigonal CuSb_2O_6 . The sample is available only in powder so we had to use experimental techniques adapted for polycrystalline samples.

5.4 SAMPLE CHARACTERIZATION

5.4.1 POWDER DIFFRACTION

Rosiaite-type CuSb_2O_6 crystallizes in the $P\bar{3}1m$ (No. 162) space group with $a = b = 5.05 \text{ \AA}$ and $c = 4.59 \text{ \AA}$. In this structure, the magnetic Cu^{2+} ions with $S = 1/2$ are arranged in trigonal layers. Since structural disorder and anisotropic spin interactions due to site mixing or lattice distortions in QSL candidates often result in a spin glass or magnetically ordered ground state, one has to have a clear idea of possible imperfections in a crystal structure.

Neutron powder diffraction at room temperature (RT) on CuSb_2O_6 was performed at D2B instrument with incident neutron wavelength of $\lambda = 1.594 \text{ \AA}$. All the observed Bragg peaks can be successfully indexed in the frame of $P\bar{3}1m$ (No. 162) space group, which implies the presence of crystallized rosiaite-type structure of CuSb_2O_6 . The following full-profile refinement by means of Rietveld method was performed in FullProf software [21]. The data demonstrate the presence of broad diffuse features at small-scattering angles similar to the previous lab x-ray, which are characteristic of an amorphous phase with short correlation length [124]. Additional background points were used in order to describe the observed diffuse features. Layered crystal structure of CuSb_2O_6 is represented by the stacking of trigonal layers with the magnetic Cu^{2+} ions divided by the non-magnetic Sb-contained layers (Fig.5.7 *right*). All cations are located in an octahedral oxygen environment. It should be noted that the diffraction pattern consists of broadened peaks compared to D2B resolution function, which suggests the presence of microstructural effects. Basically, the diffraction line broadening may occur due to two factors: crystalline size (finite coherent domain size of scattering grains) and/or local lattice strains. The isotropic strain model allowed us to sufficiently describe the peak broadening in the CuSb_2O_6 diffraction pattern. On one hand, strain-type broadening can be caused by crystal imperfections, such as lattice dislocation or stacking faults. There are other sources of strain, which are the grain boundary triple junction, coherency stresses, contact or sinter stresses, etc [125]. The refined parameters are shown in Table 5.1.

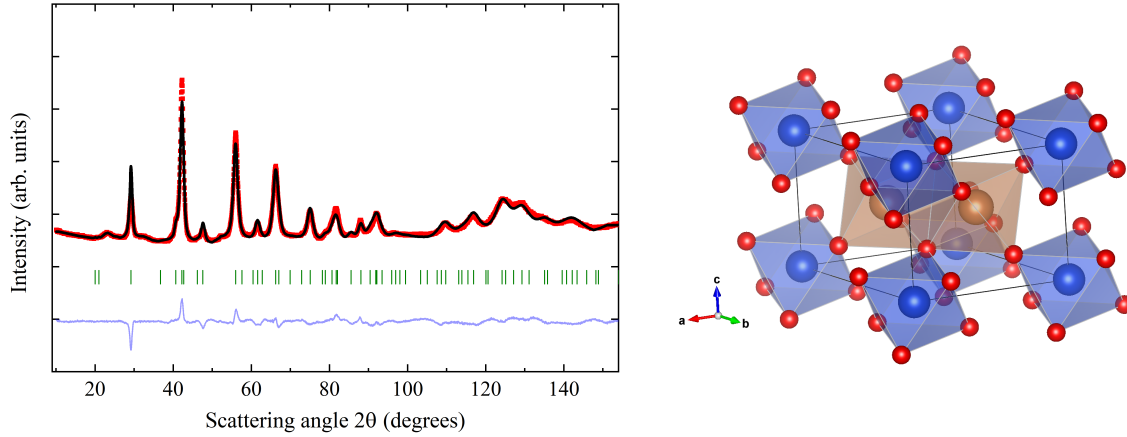


FIGURE 5.7
RT powder neutron diffraction pattern measured at D2B@ILL.

TABLE 5.1

Crystallographic data of CuSb_2O_6 within the framework of the P-31m (No. 162) space group at RT observed using neutron powder diffraction (D2B, $\lambda = 1.594 \text{ \AA}$) data refinement. Lattice parameters are $a = b = 5.0562(4) \text{ \AA}$ and $c = 4.5888(5) \text{ \AA}$. Global $\chi^2 = 2.96$. Agreement factors are $R_p = 4.04$, $R_{wp} = 5.41$, and $R_{exp} = 3.14$.

Atom	Site	x/a	y/b	z/c	Occupancy
Cu	1a	0	0	0	1
Sb	2d	1/3	2/3	1/2	1
O	6k	0.337(2)	0	0.243(1)	1

We understand that the crystal structure is not ideal and may contain microstructural defects such as stacking faults and/or lattice dislocations. However, for us, the main result from powder diffraction is that the measured powder sample contains a highly-symmetric triangular arrangement of Cu^{2+} ions, what makes this material interesting for research.

5.4.2 DC SUSCEPTIBILITY

As was mentioned in Section 2.4, one of the methods, which can be used for sample characterization is a dc susceptibility, which can be well adapted for powder samples. We have performed temperature dependence of magnetic susceptibility on the PPMS instrument down to $T = 2 \text{ K}$. The results are presented in Fig. 5.8 *left*. Temperature dependence of the magnetic susceptibility does not show any anomaly or peaked feature down to 2 K, which supports the absence of the long-range magnetic order.

The data were fitted to the Curie-Weiss equation $\chi = \chi_0 + \frac{C}{T-\Theta}$ to obtain the effective paramagnetic moment μ_{eff} and Θ . The Curie constant C yields an effective paramagnetic moment following the expression $\mu_{eff} = \sqrt{3k_B C / N_A}$, Weiss temperature $\Theta = -\frac{S(S+1) \sum_{j=1}^z J_{ij}}{3k_B}$ stands for the strength and nature of the magnetic interactions, and χ_0 is temperature-independent susceptibility (background) term. By varying the fitted temperature range (changing T_{min}), one can observe a plateau starting from $T_{min} \approx 110$ K (Fig. 5.8 right). Therefore, for the fitted values $C = 0.51 \pm 0.01 \frac{\text{emu} \cdot \text{K}}{\text{mol} \cdot \text{Oe}}$, $\Theta = -24 \pm 1$ K, $\chi_0 = (0.38 \pm 0.01) \cdot 10^{-3} \frac{\text{emu}}{\text{mol} \cdot \text{Oe}}$, the mean values in the temperature range $T = 110 - 290$ K were taken, and the corresponding error bars were estimated as its divergence from the mean value in the same temperature range. The effective magnetic moment per Cu^{2+} ion obtained from Curie constant C is $\mu_{eff} = 2\mu_B$. The spin-only magnetic moment is given by $\mu_S = g\sqrt{S(S+1)}$ and equals 1.73 for Cu^{2+} considering $g = 2$. The deviation of the μ_{eff} from the spin-only value naturally occurs from the larger value of g -factor $g = 2.196$, which was reported in [124], and thus gives the value of $\mu_{eff} = 1.9\mu_B$. The inverse dc susceptibility diverges from Curie-Weiss law below 50 K. The negative sign of Weiss temperature indicates dominant AFM interactions. The absence of zero-field cooled (ZFC) and field cooled (FC) splitting in Fig. 5.8 inset rules out any spin freezing down to 2 K.

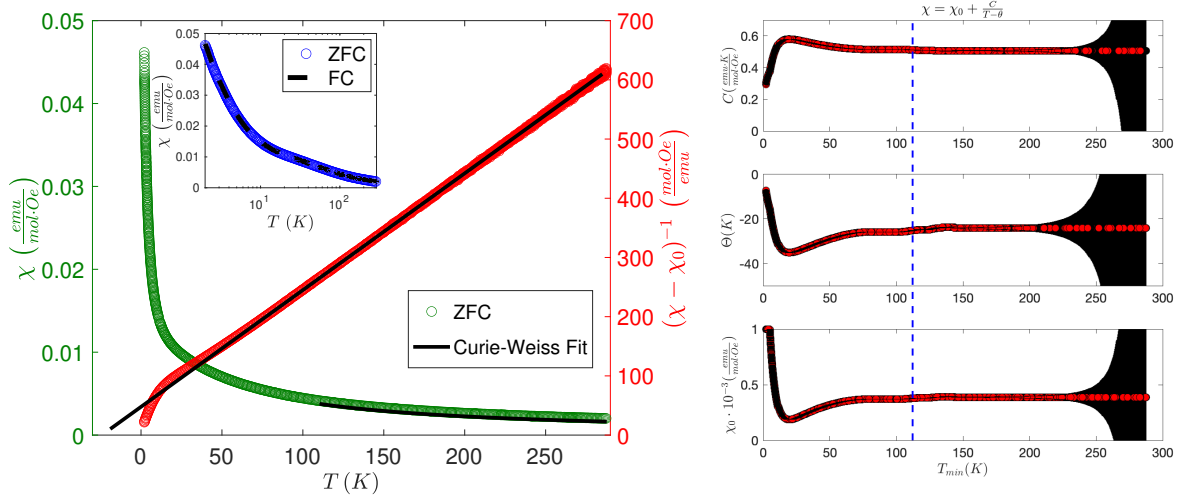


FIGURE 5.8

Left: Temperature dependence of the magnetic susceptibility of CuSb_2O_6 measured at $B = 0.1$ T; *Inset:* The dependencies of magnetic susceptibility measured in the field cooled and zero-field cooled regimes. *Right:* Fitted parameters C , Θ , χ_0 from Curie-Weiss law vs T_{min} (explained in the text).

With the same instrument, we measured field dependence of magnetization $M(H)$ up to 14 T. As it is evident from Fig. 5.10, at the lowest temperature $T = 1.7$ K, there is no hint of a plateau that would indicate a transition of the sample to a ferromagnetic state, thus this is further evidence of significant antiferromagnetic interactions. At 8 K, magnetization isotherms start to show a curvature, which becomes prominent at lower temperatures. The 50 K data-set is in agreement

with susceptibility data, which at 50 K follows Curie-Weiss law. Measured magnetic isotherms in the temperature range 1.7-8 K were analyzed within the framework of the following equation:

$$M(H, T) = \chi(T)H + N_A \mu_B f_{imp} S_{imp} g_{imp} B_S \left(\frac{g_{imp} S_{imp} H \mu_B}{k_B (T - \Theta_{imp})} \right), \quad (5.1)$$

where $\chi(T)$ represents the intrinsic susceptibility which we assume to be the same in the certain temperature range, f_{imp} , g_{imp} , S_{imp} , and Θ_{imp} denote the impurity/disorder concentration, the Lande g -factor, spin, and correlation temperature for impurity spins. The symbols H , N_A , k_B , μ_B , and B_S refer to the magnetic field, the Avogadro number, the Boltzmann constant, the Bohr magneton, and the Brillouin function, respectively.

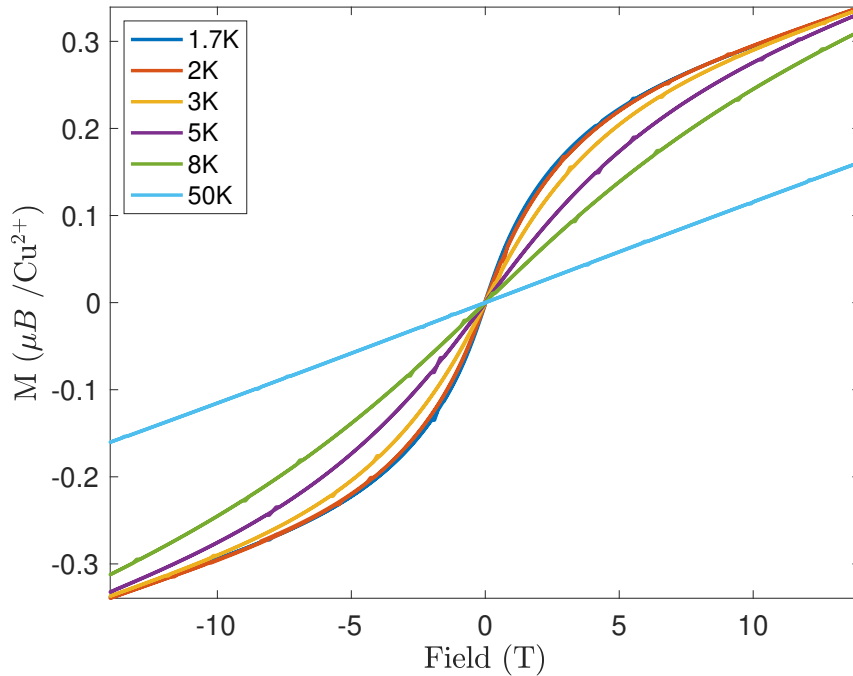


FIGURE 5.9

The magnetization isotherms measured in the field range (-14 – 14 T) and in the temperature range 1.7 – 50 K.

There are five parameters to be varied, and a simultaneous fitting of these parameters gives non-physical values. Additionally, by fixing S_{imp} to 1/2 and let the other four parameters be free, one obtains a high g -factor value. Since there is still a doubt about the actual value of g -factor, we have fixed the values to 2.3 and 2.2 in different series of fitting. The result of different fittings is presented in Table 5.2, where (f) denotes the fixed parameter. The temperature range in the first column defines the number of data sets fitted simultaneously. As a result, the value of Θ_{imp} is almost zero, which suggests the absence of magnetic correlation among impurity spins so one can treat them as purely paramagnetic. The obtained free-spin concentration is around 3%

and remains stable during different fitting configurations and in the following analysis will be neglected.

Temp range	S_{imp}	g_{imp}	$\chi(T)$	Θ_{imp}	f_{imp}
1.7 – 8K	1/2 (f)	2.5028	0.0113	-0.58	0.0257
1.7 – 5K	1/2 (f)	2.6531	0.0117	-0.66	0.0236
1.7 – 3K	1/2 (f)	2.8864	0.0121	-0.84	0.0213
1.7 – 2K	1/2 (f)	3.8756	0.0122	-1.76	0.0158
1.7 – 8K	1/2 (f)	2.3 (f)	0.0119	-0.24	0.0271
1.7 – 5K	1/2 (f)	2.3 (f)	0.0121	-0.20	0.0267
1.7 – 3K	1/2 (f)	2.3 (f)	0.0121	-0.24	0.0267
1.7 – 2K	1/2 (f)	2.3 (f)	0.0122	-0.29	0.0266
1.7 – 8K	1/2 (f)	2.2 (f)	0.0122	-0.08	0.0279
1.7 – 5K	1/2 (f)	2.2 (f)	0.0122	-0.07	0.0277
1.7 – 3K	1/2 (f)	2.2 (f)	0.0121	-0.14	0.0279
1.7 – 2K	1/2 (f)	2.2 (f)	0.0122	-0.19	0.0278

TABLE 5.2

Results of various fits to the magnetization curve with Eq.5.1.

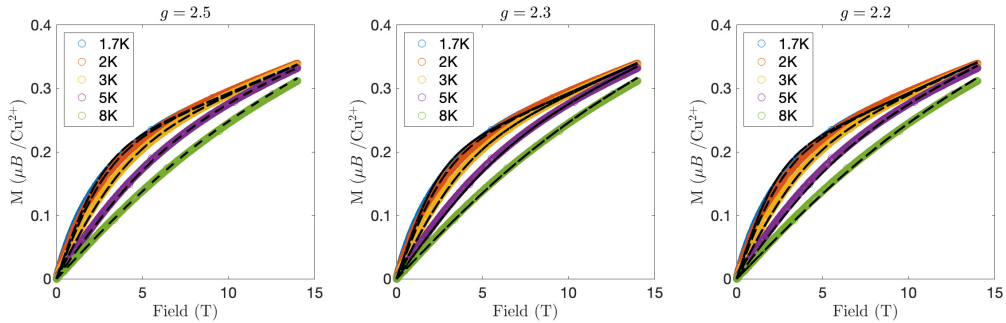


FIGURE 5.10

The magnetization isotherms measured in the field range (0 – 14 T) and in the temperature range 1.7 – 8 K are shown. The dashed lines are fits to an equation described in the text. *Left*: Simultaneous fitting of 1.7 – 8 K data-sets with only $S_{imp} = 1/2$ fixed; *middle*: simultaneous fitting of 1.7 – 8 K data-sets with $S_{imp} = 1/2$ and $g_{imp} = 2.3$ fixed; *right*: simultaneous fitting of 1.7 – 8 K data-sets with $S_{imp} = 1/2$ and $g_{imp} = 2.2$ fixed;

5.4.3 SPECIFIC HEAT

Another important bulk characteristic to measure (Section 2.5) is specific heat, which is a sum of all the fluctuations present in the system. The $C_p(T)$ data, specific heat at constant pressure, obtained in the temperature range 2 – 200 K in zero field and in 14 T magnetic field is shown in

5.11. The $C_p(T)$ above 80 K for both fields is essentially the same, increasing monotonically with increasing temperature. None of the curves show a peak like feature (or λ -anomaly), which in turn again indicates the absence of long-range magnetic ordering.

In the absence of non-magnetic analogue of CuSb_2O_6 , in order to extract the magnetic contribution of the specific heat $C_m(T)$ and to deduce the corresponding entropy S_m , we simulated the lattice contribution from the high temperature data by taking into account Debye (C_D) and Einstein ($C_{E,i}$) contributions $C_p = C_D + \sum_i C_{E,i}$ with:

$$C_D = 9n_D R \left(\frac{T}{\Theta_D} \right)^3 \int_0^{x_D} \frac{x^4 e^x}{(e^x - 1)^2} dx,$$

$$C_E = 3n_E R \left(\frac{\Theta_E}{T} \right)^2 \frac{\exp\left(\frac{\Theta_E}{T}\right)}{\left(\exp\left(\frac{\Theta_E}{T}\right) - 1\right)^2},$$

where R is the gas constant, Θ_D and Θ_E are Debye and Einstein temperatures respectively, and n_D and n_E are the numbers of corresponding modes; the sum $n_D + n_E$ is the total number of atoms per formula unit. The best fit to zero-field data was obtained using one Debye and two Einstein modes with the corresponding temperatures $\Theta_D = 715\text{K}$, $\Theta_{E,1} = 190\text{K}$, $\Theta_{E,2} = 1071\text{K}$, and the numbers $n_D = 5$, $n_{E,1} = 2$, $n_{E,2} = 2$. The solid line in Fig. 5.11 is the fit result for the total lattice contribution. While the parameters in the phenomenological phonon fit may not be directly physical, they provide a parametrization of the lattice contribution to the specific heat, which can be subtracted to estimate the magnetic specific heat. The red symbols in Fig. 5.11 show the resulting C_m/T over temperature. The inset shows the magnetic entropy $S_m(T)$ obtained by integrating C_m/T over temperature. The magnetic entropy saturates around 100(2) % of $R \ln 2$ per formula unit, which is in agreement with the entropy of a two-level spin-half system.

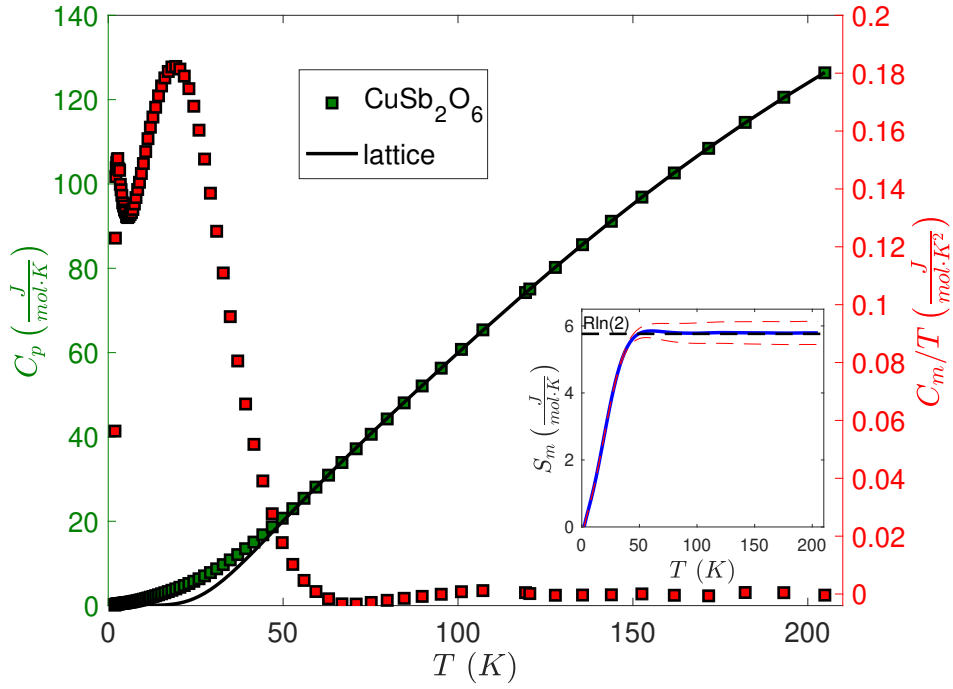
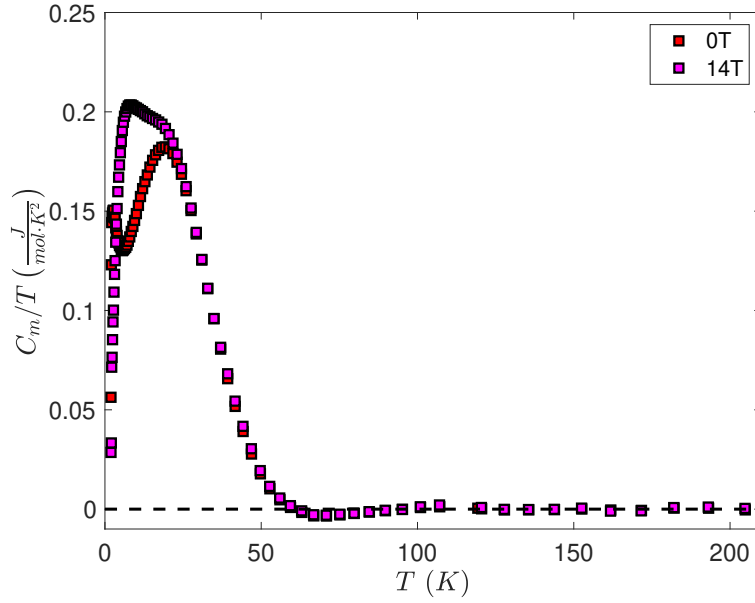


FIGURE 5.11

Specific heat C_p as a function of temperature in zero field (green). The solid black line is the fitted lattice contribution. The red curve (right vertical axis) corresponds to the magnetic part of the specific heat C_m/T . The inset shows the magnetic entropy S_m (blue). The red dashed lines show confidence interval.

A similar analysis was performed on 14 T data (Fig. 5.12). The magnetic contribution in the 14 T field has slight differences compared to 0 T data, and at $T \approx 25$ K two curves start to coincide. One has to notice that the magnetic part of the specific heat drops to zero slightly above 50 K, which is in good agreement with the experimental results discussed above.


FIGURE 5.12

Magnetic contribution to the specific heat at 0T and 14T applied magnetic field.

Overall, experimental findings so far indicate the absence of magnetic ordering down to 1.7K. The susceptibility data indicate the presence of significant antiferromagnetic interactions, while the magnetic specific heat data showed that all magnetic fluctuations are concentrated up to 50K. No splitting of ZFC and FC magnetic susceptibility is observed, thereby confirming the absence of a spin-glass state.

5.5 ABSENCE OF LONG-RANGE MAGNETIC ORDER

By now, we were still missing low-temperature measurements having the experimental findings down to $T = 1.7$ K only. However, thermodynamic studies at temperatures as low as possible are necessary to demonstrate the quantum spin-liquid character for this material. With muon spectroscopy, one can probe the local fields resulting from static moments, even disordered ones. So, performing such experiment at very low temperatures could reveal the presence or absence of long-range magnetic order and spin freezing.

Muon spin relaxation experiment has been performed using MUSR instrument at ISIS facility. In this experiment, we have used dilution refrigerator (down to 46 mK) and orange cryostat (2 – 200 K). For the measurements, about 2 g of powder CuSb_2O_6 (separately for dilution and cryostat) was attached to a silver plate for a good thermalization.

Figure 5.13 represents muon relaxation signal in zero field for the selected temperatures below 2 K. At all temperatures, the signal decreases continuously without oscillations up to $15 \mu\text{s}$.

Note that the data are shifted vertically by 0.02 successively, starting from 0.046 K for better visualization.

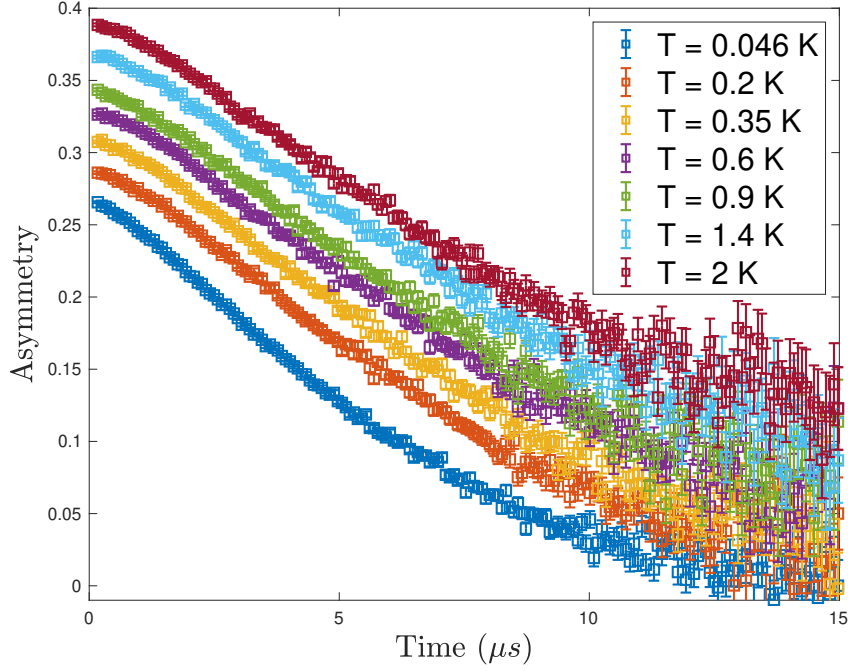


FIGURE 5.13

Selected low-temperature ZF- μ SR signals up to 2 K. The data are shifted vertically starting from 0.046 K by 0.02 a.u.

The absence of LRMO was reported previously [124] down to 2 K. Figure 5.14 represents muon relaxation signal in zero field at 0.046 K and 2 K. Since these two curves do not show any muon precession or significant drop of the asymmetry, it may be concluded that there is no LRMO down to 46 mK in this compound.

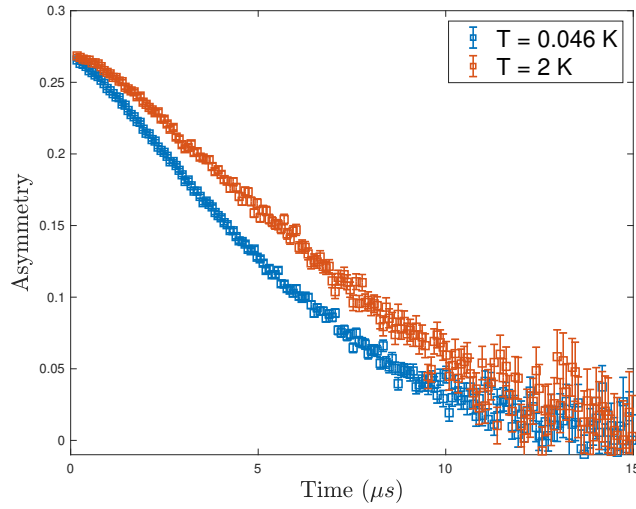


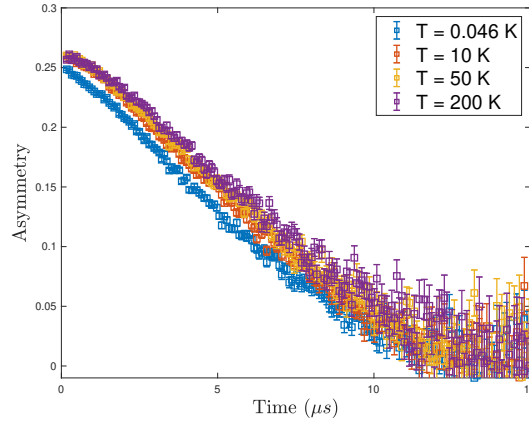
FIGURE 5.14
ZF- μ SR signals at $T = 46$ mK and $T = 2$ K.

Our ZF data are well-fitted with the following function:

$$A(t) = A_0 \left(\exp \left(-\frac{\Delta^2 t^2}{2} \right) \left(1 - \Delta^2 t^2 \right) \frac{2}{3} + \frac{1}{3} \right) \exp(-\lambda t) + A_{bkg},$$

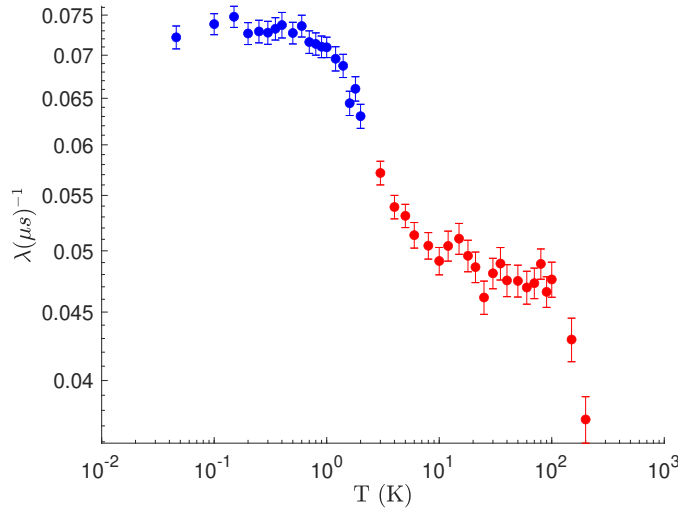
where $\exp \left(-\frac{\Delta^2 t^2}{2} \right) \left(1 - \Delta^2 t^2 \right) \frac{2}{3} + \frac{1}{3}$ – Kubo-Toyabe relaxation function, which is related to the nuclear static fields [126]. Here, $A_0 \approx 0.25$ is the initial asymmetry, λ is the μ^+ spin relaxation rate, and A_{bkg} is a background constant. As background constant depends on the sample environment, from the low temperature fit we fixed A_{bkg} at the values 0.008 and 0.018 for the cryostat and dilution fridge respectively, and background-subtracted data will be shown in the following. The spectrum at 200 K was fit with $\Delta = 0.11 \mu\text{s}^{-1}$, a typical rate for depolarization by Cu nuclear moments [127], which we fixed and used for all temperatures. We have also attempted to describe the data using a product function of Gaussian Kubo-Toyabe and stretched exponent function $A_0 \cdot GKT \cdot \exp(-(\lambda t)^\beta)$. However, at all temperatures it showed small deviations around $\beta = 1$. Another fit was assuming only stretched exponent function $A_0 \exp(-(\lambda t)^\beta)$, but nonphysical negative value of background constant A_{bkg} , and nonphysical "intermediate" $1 < \beta < 2$ were obtained. Overall, neither of these expressions capture the behavior well across the whole temperature range.

In figure 5.15 zero-field asymmetry curves at 0.046, 10, 50 and 200 K are shown. As can be seen, the muon depolarization is slow, indicating weak magnetism, and the variation with temperature is very weak. However, the fact that the data can be described only with the product of GKT and exponential decay indicates the contribution from nuclear moments and electronic local moments.


FIGURE 5.15

Zero field background-subtracted muon asymmetry curves at 0.046, 10, 50 and 200 K.

Any spin freezing can be ruled out on the following arguments. Zero-field muon decay asymmetry data relax to the same baseline value at all temperatures. This is significant – if the system were to undergo a spin freezing transition at low temperatures, one would expect to observe a recovery of the polarization to one-third tail below the transition due to the presence of disordered, static, local fields at the muon stopping site [128]. In a spin glass, the relaxation rate will typically increase by several orders of magnitude below the freezing point ($\lambda \approx 1 - 20 \mu\text{s}^{-1}$) [128–130].


FIGURE 5.16

Temperature dependence of the μ^+ spin relaxation rates from the zero field μSR measurements. Blue circles represent dilution fridge data, red circles – cryostat data.

Figure 5.16 shows the temperature dependence of the muon spin depolarization rate, λ . Above ≈ 30 K, the system is in a fast fluctuating regime from which there is a slowing of spin

dynamics down to 1 K. Below 1 K the data show a plateau in the depolarization rate – a clear indicator of persistent dynamics at low temperatures. In our case, relaxation plateau $\lambda(T)_{T<1}$ reaches the value of $0.075 \mu\text{s}^{-1}$. The magnitude of the plateaus, however, for potential QSL candidates, can vary significantly between systems [131], from e.g. $\lambda = 0.05 \mu\text{s}^{-1}$ in Herbertsmithite [132],[133] and $\text{ZnCu}_3(\text{OH})_6\text{SO}_4$ [134] to $\lambda = 0.45 \mu\text{s}^{-1}$ in Kapellasite [135] and $[\text{NH}_4]_2[\text{C}_7\text{H}_{14}\text{N}][\text{V}_7\text{O}_6\text{F}_{18}]$ [136].

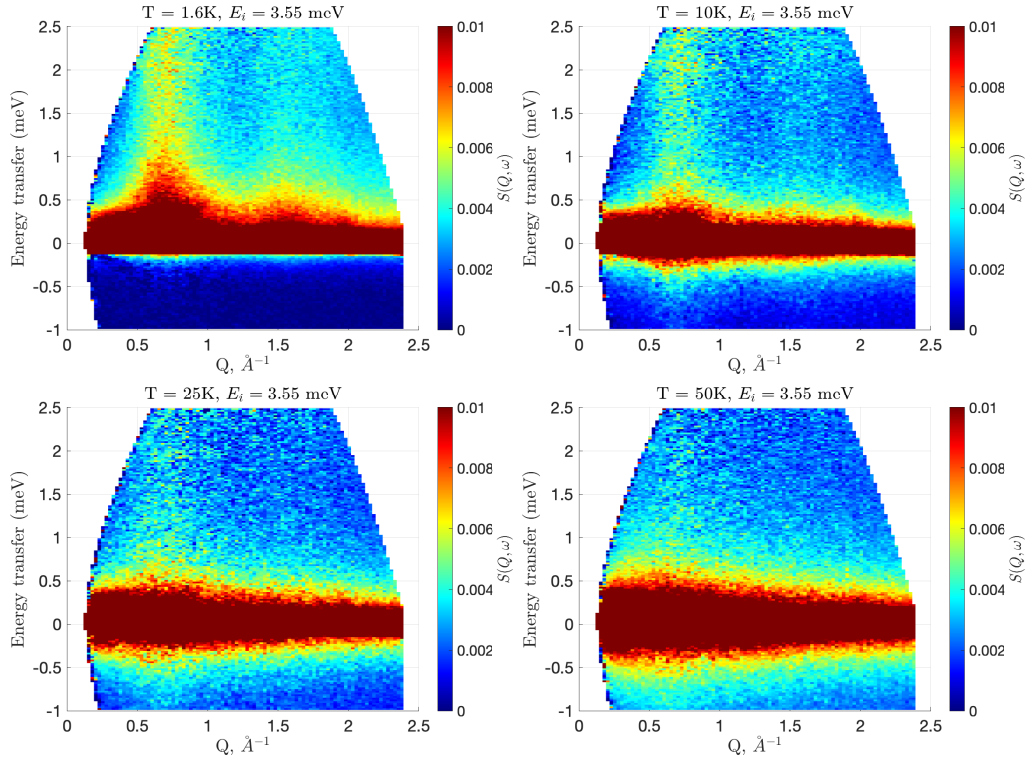
Overall, according to static magnetic properties, CuSb_2O_6 has met the essential requirement of QSL – the absence of any static ordering down to 46 mK. Now we move to dynamic magnetic properties measured by means of neutron scattering.

5.6 MAGNETIC EXCITATIONS IN CuSb_2O_6

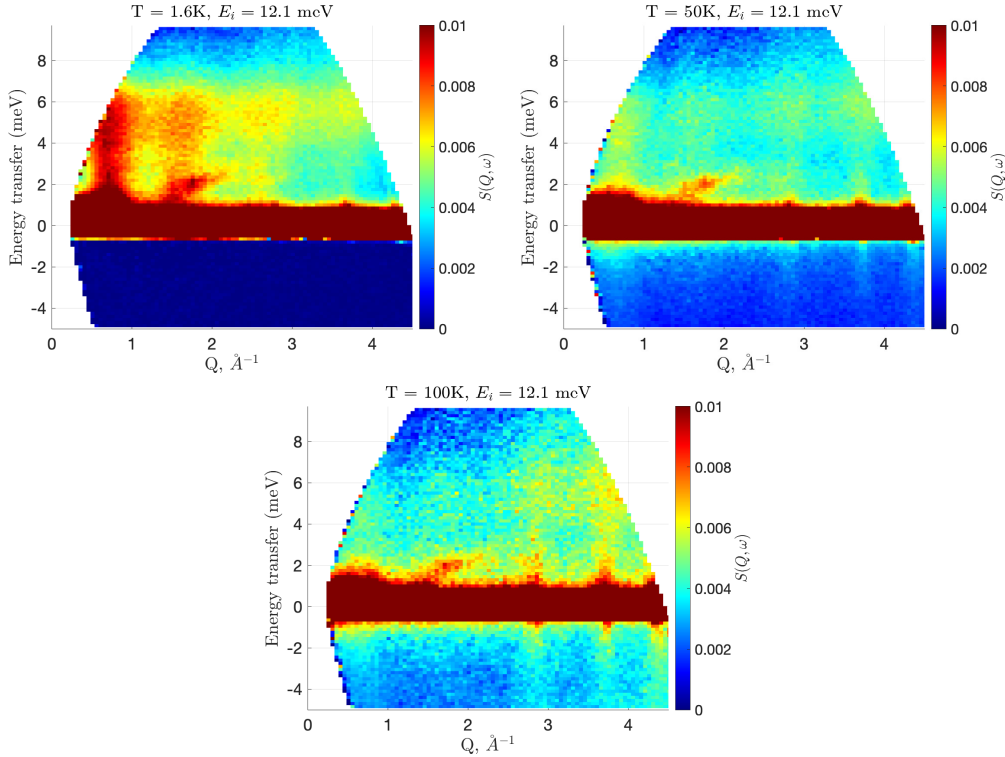
First, to have an overview of possible magnetic excitations, inelastic neutron scattering measurements were performed at $1.6 \text{ K} < T < 100 \text{ K}$ on the neutron time-of-flight spectrometer IN5 at the ILL using incident neutron energies of 3.55 and 12.1 meV. A powder sample of mass 10.5 g was held in an annular aluminium can.

The data reduction for each energy and temperature was performed with MANTID software [58] as follows. The data were loaded and normalized to monitor counts. We calibrated incident energy and fitted elastic channel in order to adjust the time-of-flight axis. The solid angle and detector efficiency was corrected by dividing the measured counts by measurement of vanadium. Finally, the TOF axis was converted to energy transfer $\hbar\omega$, scattering angle 2Θ was converted to Q , and we get $S(Q, \omega)$ map as an output. The same procedure was applied to the empty container data measured at the lowest $T = 1.6 \text{ K}$ temperature in order to subtract the background caused by neutron scattering on the sample environment and sample holder (cryostat), and by the instrument.

Standard data reduction gave the neutron scattering function $S(Q, \omega)$, shown in Fig. 5.17 and 5.18 for $E_i = 3.55$ and 12.1 meV respectively. With high incident energy, one can observe steep dispersion that reaches out to about 6-7 meV at 1.6 K and its absence at $T = 100 \text{ K}$, which, to some extent, tells us that observed scattering can be attributed to the magnetic one. The “dispersive feature” near 1.5 \AA^{-1} is spurious, it is absent at $E_i = 3.55 \text{ meV}$. Moreover, at lower energy, we observe structure-less paramagnetic scattering already at $T = 50 \text{ K}$, which fully agrees with previous macromagnetic measurements. Two lobes of the excitations at $Q \approx 0.7$ and 1.5 \AA^{-1} at $E_i = 3.55 \text{ meV}$ are clearly of magnetic origin, whereas at higher energy $E_i = 12.1 \text{ meV}$ other two lobes interfere with nuclear scattering.


FIGURE 5.17

$S(Q, \omega)$ measured at $T = 1.6, 10, 25$ and 50 K at IN5 with neutron incident energy $E_i = 3.55$ meV


FIGURE 5.18

$S(Q, \omega)$ measured at $T = 1.6, 50$ and 100 K at IN5 with neutron incident energy $E_i = 12.1$ meV

Complementary to IN5, we have performed low-temperature $T = 60$ mK and $T = 1.7$ K inelastic scattering experiment at LET instrument with incident energies 12.14, 3.7, 1.77 and 1.03 meV (Fig. 5.19) to find out if there is any gap at lower energies, which makes sense to study only at dilution temperatures. The same sample was used and loaded to the copper can in order to provide a good thermalization. Unfortunately, empty container measurements were not conducted since it makes sense to perform such measurements only with a dilution fridge setup. One can observe Bragg peaks from copper container at $E_i = 12.14$ meV starting from $Q = 3 \text{ \AA}^{-1}$.

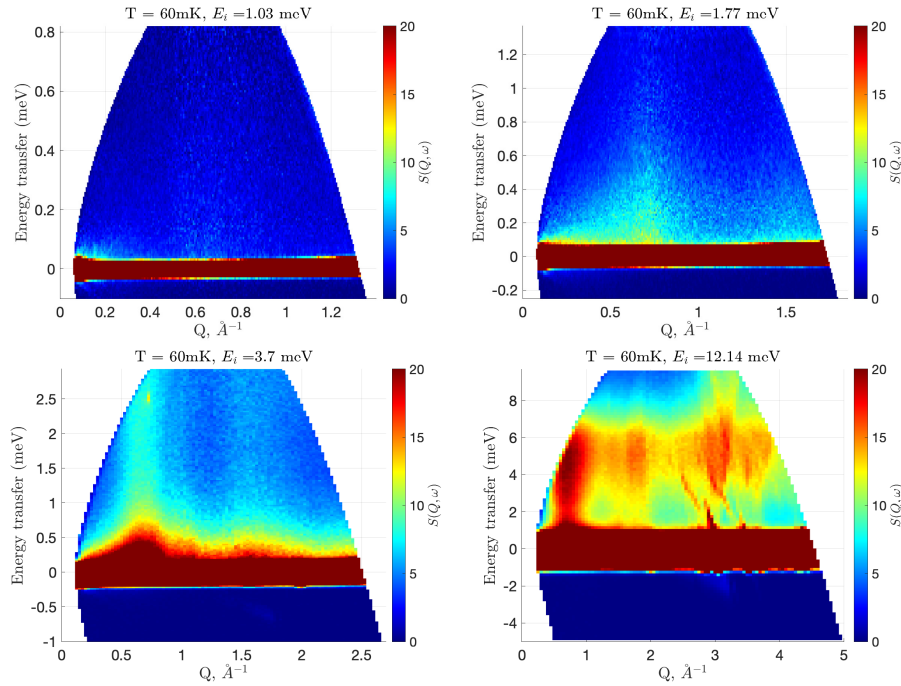
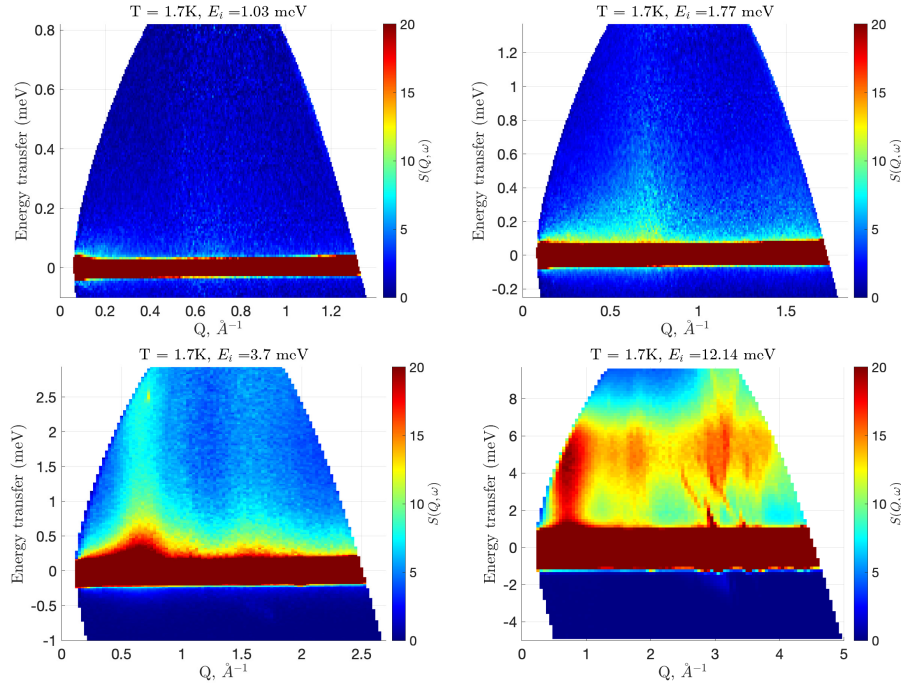


FIGURE 5.19

$S(Q, \omega)$ measured at $T = 60$ mK at LET with neutron incident energy $E_i = 1.03, 1.07, 3.70$, and 12.14 meV


FIGURE 5.20

$S(Q, \omega)$ measured at $T = 1.7\text{K}$ at LET with neutron incident energy $E_i = 1.03, 1.07, 3.70$, and 12.14 meV

Using detailed balance, we can extract the imaginary part of dynamic susceptibility $\chi''(Q, \omega)$ using the following equation

$$S(Q, \omega) = \frac{1}{\pi} \frac{1}{1 - e^{-\hbar\omega/k_B T}} \chi''(Q, \omega).$$

The advantage of $\chi''(Q, \omega)$ is that trivial temperature dependence of $S(Q, \omega)$ related to the population of excitations has been removed (Fig. 5.21 and 5.22).

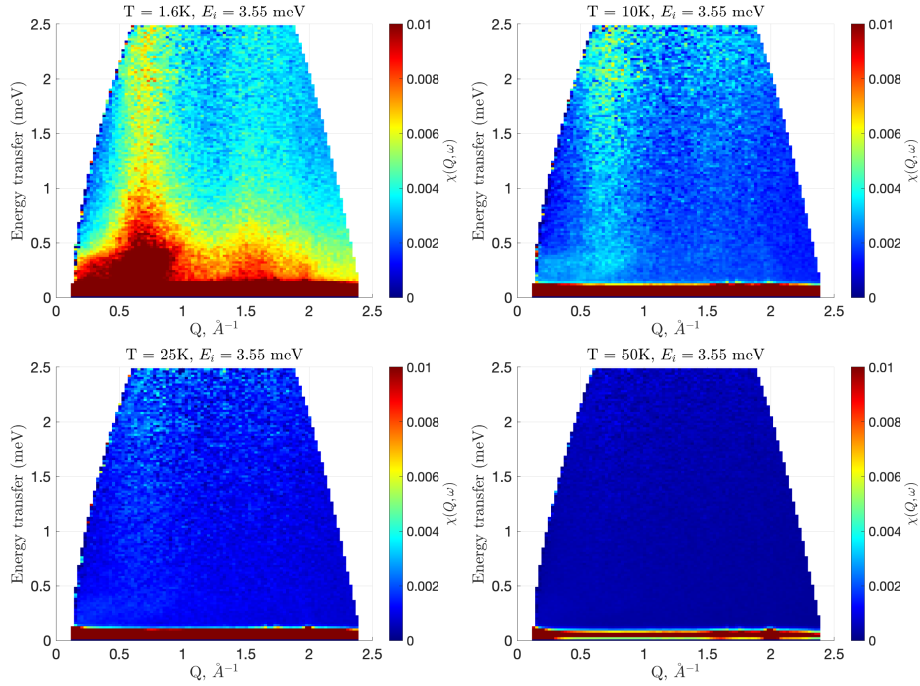


FIGURE 5.21

$\chi''(Q, \omega)$ measured at $T = 1.6, 10, 25$, and 50 K at IN5 with neutron incident energy $E_i = 3.55$ meV

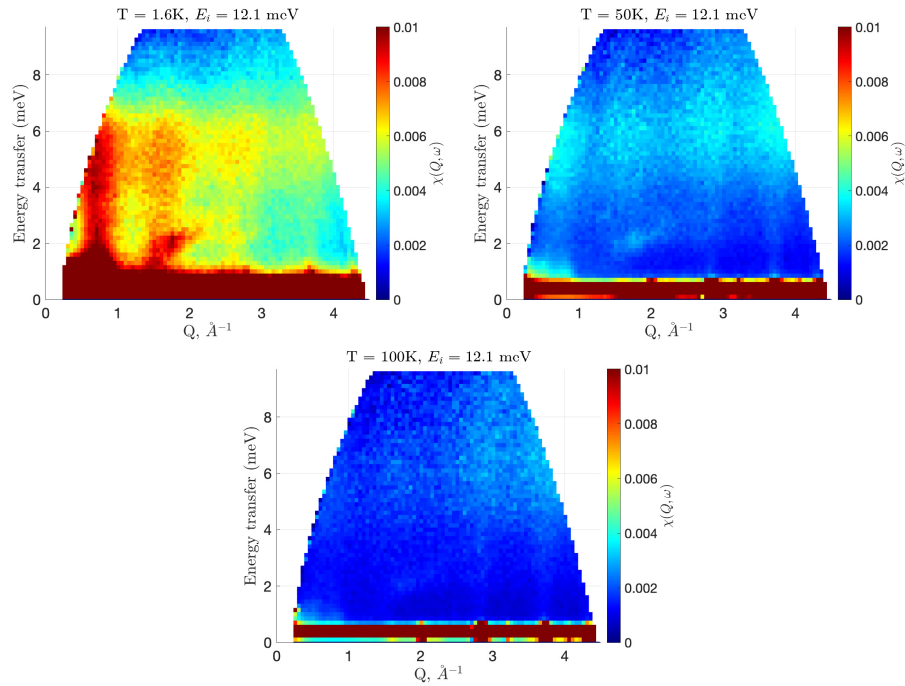


FIGURE 5.22

$\chi''(Q, \omega)$ measured at $T = 1.6, 50$, and 100 K at IN5 with neutron incident energy $E_i = 12.1$ meV

The imaginary part of the magnetic susceptibility $\chi''(Q)$ obtained by integrating $\chi''(Q, \omega)$ over the energy range $0.4 \text{ meV} < E < 2 \text{ meV}$ is shown in Fig. 5.23. This energy range was chosen to

avoid the elastic line, the remaining IN5 background at energies $E > 2$ meV and an additional spot at $E \approx 2.5$ meV on LET data. At low temperature, one can observe two broad features centered at $Q \approx 0.65 \text{ \AA}^{-1}$ and $Q \approx 1.5 \text{ \AA}^{-1}$, which gradually disappears with increasing temperature (Fig. 5.23 *left*). Interestingly that LET data at 1.7 K and 60 mK (Fig. 5.23 *middle*) show no qualitative change and only a small increase of intensity at the lowest temperature. An additional feature occurs at LET data on the first peak around $Q \approx 1 \text{ \AA}^{-1}$. However, further comparison with scaled IN5 data (Fig. 5.23 *right*) confirms the same character of the observed excitations, and most likely, this feature was hidden in the IN5 experiment due to the worse instrument resolution.

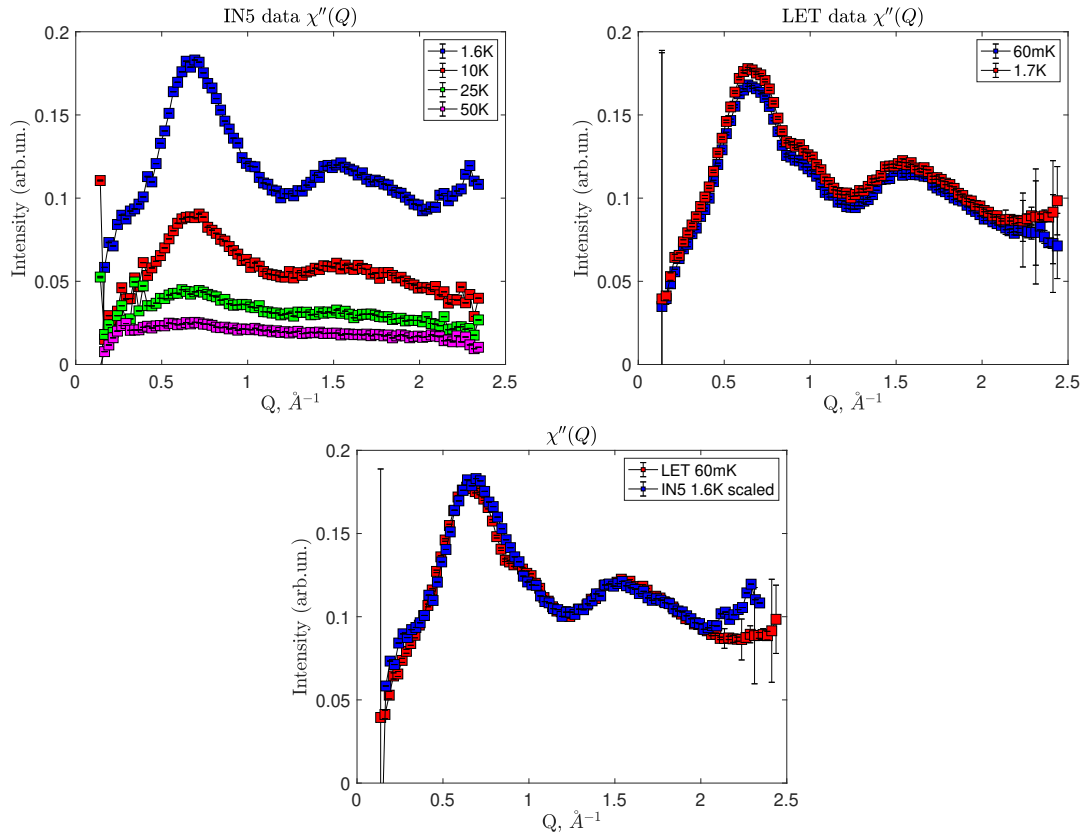


FIGURE 5.23

Wave-vector dependence of $\chi''(Q)$ integrated over the energy range $0.4 < E < 2$ meV: *left* IN5 data; *middle* LET data; *right* comparison of IN5 data ($E_i = 3.55$ meV) and LET data ($E_i = 3.70$ meV). Integrated LET and IN5 data was prepared with the same momentum transfer $Q = 0.025 \text{ \AA}^{-1}$ and energy $E = 0.02$ meV binning.

Low-energy LET data with neutron incident energies $E_i = 1.77$ and 1.03 meV were used in order to study the presence or absence of an anisotropic gap in the spectra of CuSb_2O_6 . For this purpose, we have integrated the imaginary part of the dynamic susceptibility over $0.5 \text{ \AA}^{-1} < Q < 0.8 \text{ \AA}^{-1}$ range, which corresponds to the first broad and most intensive feature (Fig. 5.24). As a result, we observe paramagnetic-like scattering with a maximum around $E \approx 0.5$ meV. An encouraging

intensity drop of 60 mK data on both data-sets around $E \approx 0.035$ meV might indicate the presence of an anisotropic gap, which might be hidden due to the instrument resolution. If a gap exists, it is smaller than $\Delta < 0.035$ meV.

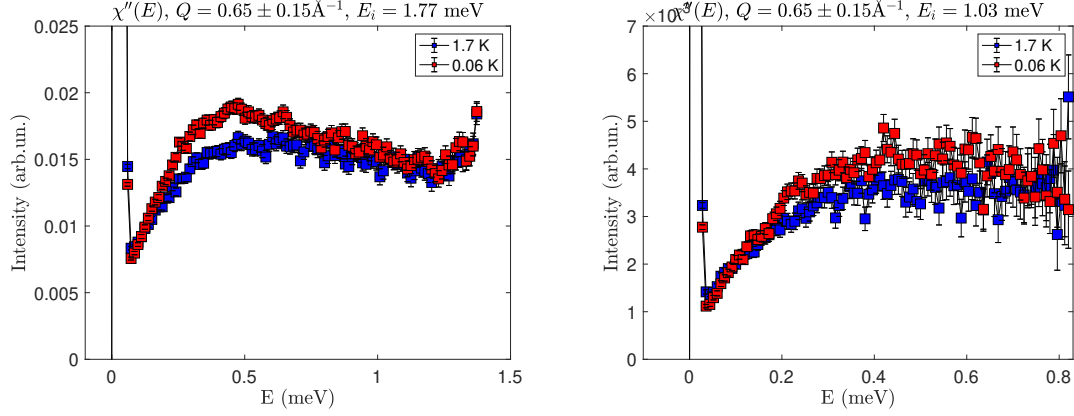


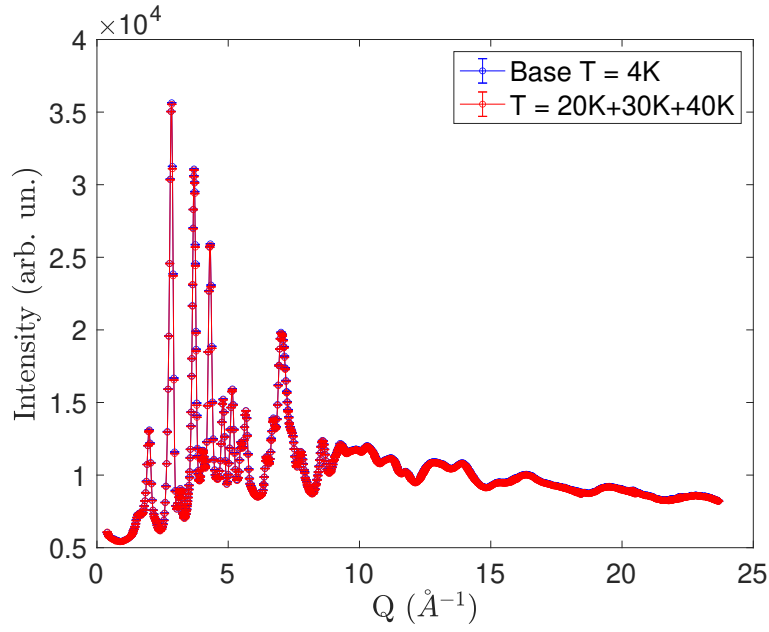
FIGURE 5.24

Energy dependence of the imaginary part of the magnetic susceptibility $\chi''(E)$ integrated over momentum transfer range $0.5 < Q < 0.8 \text{ \AA}^{-1}$ for $T = 1.7$ and 0.06 K. LET data with incident energy *left*: $E_i = 1.77$ meV and *right*: $E_i = 1.03$ meV

It is worth to mention that the observed broad continuous-like scattering appearing at specific $|\mathbf{Q}|$ values (e.g. Fig.5.21), was evidenced in several other potential QSL candidates [135], [137], [11]. Indeed, the observed spectra are very far from the classical paramagnons, which are prototypes of magnons in a paramagnetic state. Despite that we are limited only to $S(|\mathbf{Q}|, \omega)$, from $S(|\mathbf{Q}|)$ one can extract information about spin-spin correlations in the system, and this will be a subject of the following Section.

5.7 CHARACTER OF SPIN CORRELATIONS IN CuSb_2O_6

We have already discussed in Section 2.1.3 that diffraction experiment is actually the same spectroscopy method but without analyzing final energies. The main aspect of the diffraction experiment is that all final energies are integrated, hence all excitations (lattice and magnetic) are integrated and ultimately contribute to the diffraction pattern. We have performed a powder neutron diffraction experiment at D4 instrument with the incident neutron wavelength of $\lambda = 0.5 \text{ \AA}$. The advantage of using D4 instrument is high incident energy $E_i > 300$ meV.

**FIGURE 5.25**

Diffraction patterns measured at D4 instrument at $T = 4$ K (blue) and at $T = 20, 30$ and 40 K, which were merged into one data-set (red).

The diffraction patterns were measured at $T = 4$ K (base and stable temperature of D4 instrument), and at several higher temperatures $T = 20, 30$, and 40 K. No difference was observed between those high temperature data, hence, we have merged them into one data-set (Fig. 5.25). Simple subtraction of these two data-sets is shown in Fig. 5.26. Interestingly that we could observe very weak but significant intensities at the same characteristic vectors $Q \approx 0.65, 1$, and 1.5 \AA^{-1} , as were captured at IN5 and LET data. Therefore, despite the fact that we have integrated IN5 and LET data in a certain energy range excluding elastic line, we can extrapolate that range to 0 meV , since we have detected those features in difference diffraction pattern, and determine the energy integrated inelastic signal as $S(Q)$.

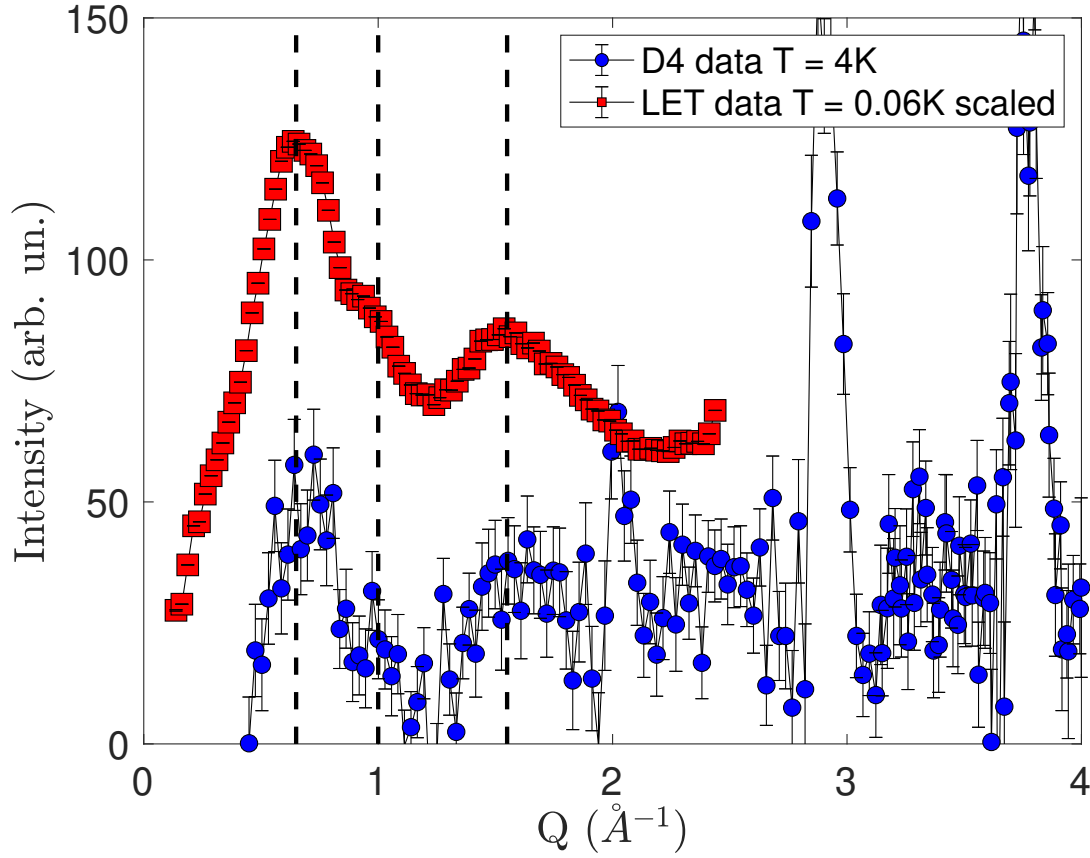


FIGURE 5.26

Difference diffraction pattern measured at D4 (blue) and integrated LET signal (red) in $0.4 < E < 3$ meV energy range. Dashed lines are the guides to the eye depicting common characteristic wave-vector features.

With the reverse Monte Carlo method implemented in SPINVERT software [35], one can reconstruct spin pair correlation function by fitting diffuse magnetic scattering independently of Hamiltonian. For the diffuse magnetic scattering data, we have taken $S(Q)$ obtained by integration of LET inelastic data at $T = 60$ mK and 1.7 K over the energy range $1 < E < 12$ meV.

First of all, technical variables (box, moves, and runs) have been tested in order to get optimal solution for the limited time of calculations. For the following calculations, we have used a $12 \times 12 \times 12$ box with 1728 randomly oriented spins (1 magnetic atom per unit cell), fixed to their crystallographic positions. Refinements were performed for 2000 proposed moves per magnetic moment, demonstrating satisfactory convergence. To minimize the statistical noise, the calculated neutron scattering was averaged over 30 independent spin configurations for each temperature.

The fit of the experimental data is shown in the first row of Fig. 5.27) *Top left*. As one can

notice, there is no significant difference between the two temperatures, which is somewhat agreed with the muon spectroscopy experiment in terms of low-temperature plateau starting at $T \approx 1$ K in Fig.5.16. Moreover, the fit of the experimental data is very good (shown by dashed line) – all the features are sufficiently described. The spin pair correlation function (Fig. 5.27 *Top right*) demonstrates sharply faded dependence with the distance between magnetic atoms. One can conclude that there is no point in considering neighbours further than that in the fifth coordination shell. For clarity, we have added the crystal structure of CuSb_2O_6 with specified distances between the neighbors in order to match with the observed spin pair correlations. Surprisingly, the strongest correlations are found to be of FM character (first positive value in Fig. 5.27 *Top right*). Moreover, that distance corresponds to the interlayer spacing. As of the most intriguing in-plane correlations within the triangular motifs, they are of antiferromagnetic origin. In addition, for the further neighbour, which is on the diagonal with distance 6.83 \AA (Fig. 5.27 *Right*), the weaker antiferromagnetic spin pair correlations can be observed. The obtained spin pair correlation function shows an intriguing result, which, at the same time, does not contradict the previous experimental findings. However, one should keep in mind that $\langle \mathbf{S}(0) \cdot \mathbf{S}(r) \rangle$ gives us the information about correlations and not interactions so that e.g. strong FM correlations between the planes might be a result of a strong AFM interaction along the diagonal etc.

Stone in [138] shows that for an isotropic powder sample, the first moment K_1 could be expressed as

$$K_1(Q) = -\frac{2}{3} \left| \frac{g}{2} f(Q) \right|^2 \frac{1}{N} \sum_{r,d} J_d \langle \mathbf{S}_r \cdot \mathbf{S}_{r+d} \rangle \left(1 - \frac{\sin Qd}{Qd} \right). \quad (5.2)$$

$S(Q)$ has as coefficients of $\frac{\sin Qd}{Qd}$ the correlation function $\langle \mathbf{S}(0) \cdot \mathbf{S}(r) \rangle$ in Eq.2.17. $K_1(Q)$ has as coefficients of $\frac{\sin Qd}{Qd}$ the correlation function $\langle \mathbf{S}(0) \cdot \mathbf{S}(r) \rangle$ multiplied with the exchange J_d apart from proportionality constants. Therefore, we can try to fit the first moment with SPINVERT and expect to obtain the same spin pair correlation function multiplied by exchange interactions. The results are shown in the second row of Fig.5.27

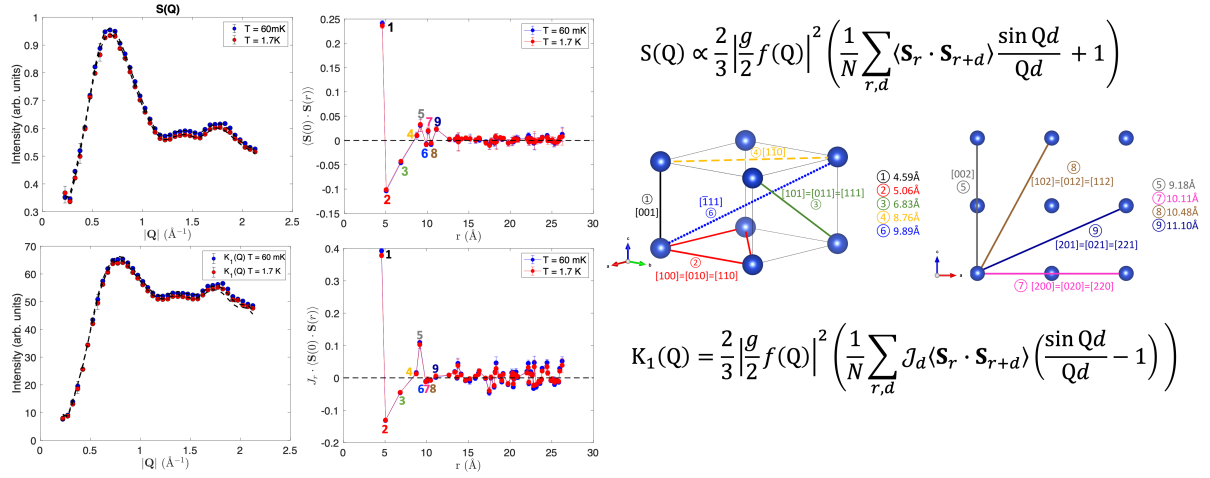


FIGURE 5.27

First row: *left* SPINVERT fit results of $S(Q)$ *right* Temperature dependence of spin-pair correlation function obtained from $S(Q)$. Second row: *left* SPINVERT fit results of $K_1(Q)$ *right* Temperature dependence of spin-pair correlation function obtained from $K_1(Q)$. *Right*: Crystal structure of CuSb_2O_6 with indicated distances.

As one can notice, the first moment $K_1(Q)$ does not differ a lot from $S(Q)$, qualitatively only the position of the first peak is shifted. As well as for $S(Q)$, there is no obvious change between the two temperatures. The results for $J_d \langle \mathbf{S}_r \cdot \mathbf{S}_{r+d} \rangle$ are shown in Fig.5.27. Since the data for the first moment $K_1(Q)$ very likely resemble $S(Q)$, one would not expect a huge change in a spin pair correlation function (or its "analog" for $K_1(Q)$). If one divides $K_1(Q)$ result by $S(Q)$ result shown in the *right* column of Fig.5.27, one will obtain numbers of the same sign, which correspond to exchange interactions J_d . This directly indicates interactions of the same sign, which obviously cannot be of a ferromagnetic nature, hence antiferromagnetic.

Now we will look closer on the obtained results (Fig.5.28). If we consider only triangular planes, which are the neighbors numbered as 2,4,7, we can see that first two of them (J_1 and J_2 in the phase diagrams given by [12] and [139]) clearly correspond to the AFM interactions, whereas the ratio for the third one (J_3 in the phase diagram given by [139]) is of the opposite sign, which might result to FM exchange. However, for our case we would exclude this FM interaction from our consideration, because if there is one, it is very weak or even zero. Therefore, since we have those two of AFM nature, and since we do not observe any long-range order, most likely CuSb_2O_6 falls into the $J_1 - J_2$ region with spin liquid phase [12, 139] and of course, additional interactions between the planes of AFM nature will only create more disorder and frustration in the system.

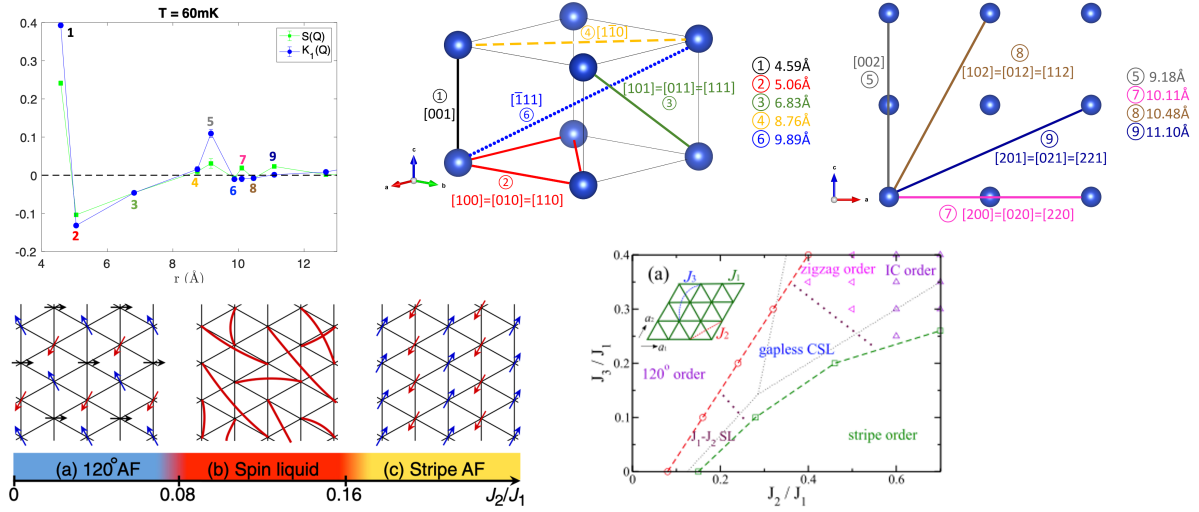


FIGURE 5.28

First row: *left* SPINVERT fit results of $S(Q)$ *right* Temperature dependence of spin-pair correlation function obtained from $S(Q)$. Second row: *left* SPINVERT fit results of $K_1(Q)$ *right* Temperature dependence of spin-pair correlation function obtained from $K_1(Q)$. *Right*: Crystal structure of CuSb_2O_6 with indicated distances.

5.8 SUMMARY

We presented a potential QSL compound CuSb_2O_6 , in which Cu^{2+} ions arrange in a triangular structure. The sample is available only in powder, so we were limited to those experimental techniques adapted for polycrystalline samples. Susceptibility, specific heat, and inelastic neutron scattering suggest the presence of magnetic fluctuations up to $T = 50$ K. Muon spectroscopy ruled out any sign of a static magnetic moment. Low-temperature inelastic scattering showed gapless continuous-like scattering, emerging at specific Q values, which is believed to be associated with the fractionalized quasiparticles, spinons, that are expected for a QSL state. Reverse Monte Carlo simulations of the first moment obtained by integrating over the whole energy region conclude the fully frustrated, most-probably three-dimensional AFM interaction scheme.

CHAPTER 6

CONCLUSION

This thesis presented an experimental study of spinon-like excitations in three examples of quantum $S = 1/2$ Heisenberg antiferromagnets. Constantly evolving experimental techniques allow to explore exotic and usually weak phenomena with unmatched precision. Research findings contribute greatly to many-body physics understanding and stimulate more intensive theoretical research.

The results of the dynamics $\text{CuSO}_4 \cdot 5\text{D}_2\text{O}$ in the applied magnetic field would probably be the final point in quantum Heisenberg $S = 1/2$ chain studies since it is clear that any discrepancies with theory will be due to the imperfection of the sample. For the first time, full field-dependent dynamics of Heisenberg spin-1/2 model material have been studied. All results indicate model behaviour of $\text{CuSO}_4 \cdot 5\text{D}_2\text{O}$. Further study requires paramagnetic mode subtraction in time-of-flight experiment and following quantitative analysis.

As of $\text{Cu}_6[\text{Si}_6\text{O}_{18}] \cdot 6\text{H}_2\text{O}$, despite a large number of experimental and theoretical findings, the results are still controversial and do not fall on the same curve. Therefore, further analytical study is needed in order to reveal the nature of the observed spinon-like continuum.

Finally, CuSb_2O_6 is a promising material to demonstrate a quantum spin liquid behaviour. The dimensionality of this QSL state is still under question, although it could be revealed with theoretical or numerical calculations.

BIBLIOGRAPHY

- [1] C. Broholm et al. ‘Quantum spin liquids’. In: *Sc.* 367 (2020), eaay0668.
- [2] L. Savary and L. Balents. ‘Quantum spin liquids: a review’. In: *Rep. Prog. Phys.* 80 (2016), p. 016502.
- [3] D. A. Tennant. ‘Studies of Spinons, Majoranas, and Monopoles in Spin Liquid and Quantum Critical Magnets with Neutrons’. In: *JPSJ* 88 (2019), p. 081009.
- [4] L. Clark and A. H. Abdeldaim. ‘Quantum Spin Liquids from a Materials Perspective’. In: *Ann. Rev. Mat. Res.* 51 (2021), p. 495.
- [5] J. Wen et al. ‘Experimental identification of quantum spin liquids’. In: *npj Quant. Mat.* 4 (2019), p. 12.
- [6] J. R. Chamorro, T. M. McQueen and T. T. Tran. ‘Chemistry of Quantum Spin Liquids’. In: *Chem. Rev.* 121 (2021), p. 2898.
- [7] B. Lake et al. ‘Quantum criticality and universal scaling of a quantum antiferromagnet’. In: *Nat. Mat.* 4 (2005), p. 329.
- [8] H. Bethe. ‘Zur Theorie der Metalle’. In: *Zeitschrift für Physik* 71 (1931), p. 205.
- [9] P. W. Anderson. ‘Resonating valence bonds: A new kind of insulator?’ In: *Materials Research Bulletin* 8.2 (1973), p. 153.
- [10] B. Bernu et al. ‘Exact spectra, spin susceptibilities, and order parameter of the quantum Heisenberg antiferromagnet on the triangular lattice’. In: *Phys. Rev. B* 50 (1994), p. 10048.
- [11] T. Han et al. ‘Fractionalized excitations in the spin-liquid state of a kagome-lattice antiferromagnet’. In: *Nat.* 492 (2012), p. 406.
- [12] Y. Iqbal et al. ‘Spin liquid nature in the Heisenberg $J_1 - J_2$ triangular antiferromagnet’. In: *Phys. Rev. B* 93 (2016), p. 144411.
- [13] T. Fennell et al. ‘Magnetic Coulomb Phase in the Spin Ice $\text{Ho}_2\text{Ti}_2\text{O}_7$ ’. In: *Science* 326 (2009), p. 415.
- [14] J. Hopkinson et al. ‘Classical Antiferromagnet on a Hyperkagome Lattice’. In: *Phys. Rev. Lett.* 99 (2007), p. 037201.

- [15] S. Chillal et al. ‘Evidence for a three-dimensional quantum spin liquid in $\text{PbCuTe}_2\text{O}_6$ ’. In: *Nat. Comm.* 11 (2020), p. 2348.
- [16] A. M. Samarakoon et al. ‘Machine-learning-assisted insight into spin ice $\text{Dy}_2\text{Ti}_2\text{O}_7$ ’. In: *Nat. Comm.* 11 (2020), p. 892.
- [17] G. L. Squires. *Introduction to the Theory of Thermal Neutron Scattering*. 3rd ed. Cambridge University Press, 2012.
- [18] S. W. Lovesey. *Theory of neutron scattering from condensed matter. Vol. 12*. 1984.
- [19] F. Hippert et al. *Neutron and X-ray Spectroscopy*. 1st ed. Springer, Dordrecht, 2006.
- [20] H. M. Rietveld. ‘A profile refinement method for nuclear and magnetic structures’. In: *JAC* 2 (1969), p. 65.
- [21] J. R-. Carvajal. ‘Recent advances in magnetic structure determination by neutron powder diffraction’. In: *PBCM* 192 (1993), p. 55.
- [22] *Layout of a D2B@ILL instrument*. <https://www.ill.eu/users/instruments/instruments-list/d2b/how-it-works/simulated-experiment>.
- [23] W. Schweika. *Polarized Neutron Scattering and Polarization Analysis*. 2012.
- [24] M. Blume. ‘Polarization Effects in the Magnetic Elastic Scattering of Slow Neutrons’. In: *Phys. Rev.* 130 (1963), p. 1670.
- [25] S. V. Maleyev, V. G. Baryakhtar and R. A. Suris. ‘On the polarization of slow neutrons scattered in crystals’. In: *Sov. Phys. Sol. St* 4 (1963), p. 2533.
- [26] F. Tasset et al. ‘Spherical neutron polarimetry with Cryopad-II’. In: *Phys. B: Cond. Matt.* 267 (1999), p. 69.
- [27] *Layout of a D3@ILL instrument*. <https://www.ill.eu/users/instruments/instruments-list/d3/description/instrument-layout>.
- [28] Eddy Lelievre-Berna. ‘Novel polarized neutron tools’. In: 4785 (2002), p. 112.
- [29] M. Mourigal. ‘Order and Dynamics of Model Quantum Antiferromagnets’. In: *EPFL* (2011).
- [30] H. Mutka. ‘Coupled time and space focusing for time-of-flight inelastic scattering’. In: *Nucl. Instr. Meth. Phys. Res. A* 338 (1994), p. 144.
- [31] *IN5 Description*. URL: <https://www.ill.eu/users/instruments/instruments-list/in5/description/instrument-layout>.
- [32] M. Russina and F. Mezei. ‘Implementation of Repetition Rate Multiplication in Cold, Thermal and Hot Neutron Spectroscopy’. In: *Jour. Phys. Conf. Ser.* 251 (2010), p. 012079.
- [33] S. Toth and B. Lake. ‘Linear spin wave theory for single-Q incommensurate magnetic structures’. In: *JPCM* 27 (2015), p. 166002.
- [34] T. Holstein and H. Primakoff. ‘Field Dependence of the Intrinsic Domain Magnetization of a Ferromagnet’. In: *Phys. Rev.* 58 (1940), p. 1098.

- [35] J. A. M. Paddison, J. R. Stewart and A. L. Goodwin. ‘Spinvert: a program for refinement of paramagnetic diffuse scattering data’. In: *Jour. Phys.: Cond. Matt.* 25 (2013), p. 454220.
- [36] R. L. Karlin. *Magnetochemistry*. Springer Berlin, 1989.
- [37] A. Tari. *The Specific Heat of Matter at Low Temperatures*. Imp. Coll. Press, 2003.
- [38] R. Kubo and T. Toyabe. *Magnetic Resonance and Relaxation*. Ed. by R. Blinc. North Holland, 1967.
- [39] R. S. Hayano et al. ‘Zero-and low-field spin relaxation studied by positive muons’. In: *Phys. Rev. B* 20 (1979), p. 850.
- [40] A. Amato. ‘Lecture Notes on μ SR technique’. In: (2018).
- [41] E. Ising. ‘Beitrag zur Theorie des Ferromagnetismus’. In: *Z. Physik* 31 (1925), p. 253.
- [42] F. D. M. Haldane. ‘General Relation of Correlation Exponents and Spectral Properties of One-Dimensional Fermi Systems: Application to the Anisotropic $S = \frac{1}{2}$ Heisenberg Chain’. In: *Phys. Rev. Lett.* 45 (1980), p. 1358.
- [43] J. des Cloizeaux and J. J. Pearson. ‘Spin-Wave Spectrum of the Antiferromagnetic Linear Chain’. In: *Phys. Rev.* 128 (1962), p. 2131.
- [44] G. Müller et al. ‘Quantum spin dynamics of the antiferromagnetic linear chain in zero and nonzero magnetic field’. In: *Phys. Rev. B* 24 (1981), p. 1429.
- [45] I. A. Zaliznyak et al. ‘Spinons in the Strongly Correlated Copper Oxide Chains in SrCuO_2 ’. In: *Phys. Rev. Lett.* 93 (2004), p. 087202.
- [46] M. B. Stone et al. ‘Extended Quantum Critical Phase in a Magnetized Spin- $\frac{1}{2}$ Antiferromagnetic Chain’. In: *Phys. Rev. Lett.* 91 (2003), p. 037205.
- [47] D. C. Dender et al. ‘Direct Observation of Field-Induced Incommensurate Fluctuations in a One-Dimensional $S = 1/2$ Antiferromagnet’. In: *Phys. Rev. Lett.* 79 (1997), p. 1750.
- [48] J. -S. Caux and R. Hagemans. ‘The four-spinon dynamical structure factor of the Heisenberg chain’. In: *J. Stat. Mech.* 2006 (2006), P12013.
- [49] M. Mourigal et al. ‘Fractional spinon excitations in the quantum Heisenberg antiferromagnetic chain’. In: *Nat. Phys.* 9 (2013), p. 435.
- [50] M. Karbach and G. Müller. ‘Line-shape predictions via Bethe ansatz for the one-dimensional spin- $\frac{1}{2}$ Heisenberg antiferromagnet in a magnetic field’. In: *Phys. Rev. B* 62 (2000), p. 14871.
- [51] M. Karbach, D. Biegel and G. Müller. ‘Quasiparticles governing the zero-temperature dynamics of the one-dimensional spin-1/2 Heisenberg antiferromagnet in a magnetic field’. In: *Phys. Rev. B* 66 (2002), p. 054405.
- [52] M. Kohno. ‘Dynamically Dominant Excitations of String Solutions in the Spin-1/2 Antiferromagnetic Heisenberg Chain in a Magnetic Field’. In: *Phys. Rev. Lett.* 102 (2009), p. 037203.

- [53] A. K. Bera et al. ‘Dispersions of many-body Bethe strings’. In: *Nat. Phys.* 16 (2020), p. 625.
- [54] Q. Faure et al. ‘Tomonaga-Luttinger Liquid Spin Dynamics in the Quasi-One-Dimensional Ising-Like Antiferromagnet $\text{BaCo}_2\text{V}_2\text{O}_8$ ’. In: *Phys. Rev. Lett.* 123 (2019), p. 027204.
- [55] L. S. Wu et al. ‘Tomonaga–Luttinger liquid behavior and spinon confinement in YbAlO_3 ’. In: *Nat. Comm.* 10 (2019), p. 698.
- [56] C. A. Beevers and H. Lipson. ‘The crystal structure of copper sulphate pentahydrate, $\text{CuSO}_4 \cdot 5\text{H}_2\text{O}$ ’. In: *Proc. R. Soc. Lond. A* 146 (1934), p. 570.
- [57] M. W. Van Tol and N. J. Poulis. ‘A high-field phase transition in the linear chain compound $\text{CuSO}_4 \cdot 5\text{H}_2\text{O}$ ’. In: *Phys.* 69 (1973), p. 341.
- [58] O. Arnold et al. ‘Mantid—Data analysis and visualization package for neutron scattering and μSR experiments’. In: *Nucl. Instr. Meth. Phys. Res. A* 764 (2014), p. 156.
- [59] R. A. Ewings et al. ‘Horace: Software for the analysis of data from single crystal spectroscopy experiments at time-of-flight neutron instruments’. In: *Nucl. Instrum. Methods Phys. Res. Sect. A* 834 (2016), p. 132.
- [60] P. J. Brown. ‘Magnetic form factors’. In: *Int. Tabl. Cryst. C* (2006).
- [61] J.-C. Bissey, R. Berger and Y. Servant. ‘Differentiated g-values and exchange interaction between dissimilar copper ions as studied by EPR in the linear chain system $\text{CuSO}_4 \cdot 5\text{H}_2\text{O}$ ’. In: *Sol. St. Comm.* 93 (1995), p. 243.
- [62] K. C. Rule et al. ‘Dynamics of azurite $\text{Cu}_3(\text{CO}_3)_2(\text{OH})_2$ in a magnetic field as determined by neutron scattering’. In: *Phys. Rev. B* 84 (2011), p. 184419.
- [63] I. Tsukada et al. ‘Two-Stage Spin-Flop Transitions in the $S = 1/2$ Antiferromagnetic Spin Chain $\text{BaCu}_2\text{Si}_2\text{O}_7$ ’. In: *Phys. Rev. Lett.* 87 (2001), p. 127203.
- [64] I. U. Heilmann et al. ‘Neutron study of the line-shape and field dependence of magnetic excitations in $\text{CuCl}_2 \cdot 2\text{N}(\text{C}_5\text{D}_5)$ ’. In: *Phys. Rev. B* 18 (1978), p. 3530.
- [65] Q. Faure et al. ‘Topological quantum phase transition in the Ising-like antiferromagnetic spin chain $\text{BaCo}_2\text{V}_2\text{O}_8$ ’. In: *Nat. Phys.* 14 (2018), p. 716.
- [66] W. Eysel and K.-H. Breuer. ‘Structural and chemical varieties of diopside, $\text{Cu}_6[\text{Si}_6\text{O}_{18}] \cdot 6\text{H}_2\text{O}$: I. Thermal properties’. In: *Z. Deutsch. Gemmol. Ges.* 184 (1988), p. 1.
- [67] E. L. Belokoneva et al. ‘The charge-density distribution, its multipole refinement and the antiferromagnetic structure of diopside, $\text{Cu}_6[\text{Si}_6\text{O}_{18}] \cdot 6\text{H}_2\text{O}$ ’. In: *PCM* 29 (2002), p. 430.
- [68] R. E. Newnham and R. P. Santoro. ‘Magnetic and Optical Properties of Diopside’. In: *PSSB* 19 (1967), K87.
- [69] M. Wintenberger, G. André and M. F. Gardette. ‘Magnetic properties of green diopside $\text{CuSiO}_3\text{H}_2\text{O}$ and of black diopside CuSiO_3 , and magnetic structure of black diopside’. In: *Sol. St. Comm.* 87 (1993), p. 309.

- [70] I. A. Kiseleva et al. ‘Thermodynamic properties of copper silicate: diopside: $\text{Cu}_6\text{Si}_6\text{O}_{18} \cdot 6\text{H}_2\text{O}$ ’. In: *Jour. Chem. Therm.* 25 (1993), p. 621.
- [71] J. M. Law et al. ‘Description of Anhydrous (Black) Diopside as a $S = 1/2$ Uniform Antiferromagnetic Chain System’. In: *Z. Anorg. Allg. Chem.* 636 (2010), p. 54.
- [72] K. Matsui et al. ‘Ground State of the Spin-1/2 Chain of Green Diopside at High Fields’. In: *JPS Conf. Proc.* 3 (2014), p. 014011.
- [73] A. Podlesnyak et al. ‘Coupled antiferromagnetic spin- $\frac{1}{2}$ chains in green diopside $\text{Cu}_6[\text{Si}_6\text{O}_{18}] \cdot 6\text{H}_2\text{O}$ ’. In: *Phys. Rev. B* 93 (2016), p. 064426.
- [74] C. Gros et al. ‘Quantum phase transition in the diopside magnetic lattice’. In: *EPL* 60 (2002), p. 276.
- [75] O. Janson et al. ‘Large quantum fluctuations in the strongly coupled spin- $\frac{1}{2}$ chains of green diopside $\text{Cu}_6\text{Si}_6\text{O}_{18} \cdot 6\text{H}_2\text{O}$ ’. In: *Phys. Rev. B* 82 (2010), p. 014424.
- [76] A. Berlie and I. Terry. ‘Absence of quantum criticality and bulk 3D magnetism in green diopside’. In: *EPL* 120 (2017), p. 47006.
- [77] N. Qureshi. ‘Mag2Pol: a program for the analysis of spherical neutron polarimetry, flipping ratio and integrated intensity data’. In: *JAC* 52 (2019), p. 175.
- [78] S. Blundell. *Magnetism in Condensed Matter*. Oxford Master Series in Physics, 2001.
- [79] S. R. Mohapatra and A. K. Singh. ‘Spin Frustrated Multiferroics: A New Way to Technology’. In: *J. Mater. Sci. Nanomater.* 2 (2017), p. 1000101.
- [80] M. E. Zhitomirsky. ‘Enhanced magnetocaloric effect in frustrated magnets’. In: *Phys. Rev. B* 67 (2003), p. 104421.
- [81] L. Seabra, P. Sindzingre and N. Shannon T. Momoi. ‘Novel phases in a square-lattice frustrated ferromagnet: $\frac{1}{3}$ -magnetization plateau, helicoidal spin liquid, and vortex crystal’. In: *Phys. Rev. B* 93 (2016), p. 085132.
- [82] P. Chandra and B. Doucot. ‘Possible spin-liquid state at large S for the frustrated square Heisenberg lattice’. In: *Phys. Rev. B* 38 (1988), p. 9335.
- [83] J. Oitmaa and R. R. P. Singh. ‘Phase diagram of the $J_1 - J_2 - J_3$ Heisenberg model on the honeycomb lattice: A series expansion study’. In: *Phys. Rev. B* 84 (2011), p. 094424.
- [84] J. Fouet, P. Sindzingre and C. Lhuillier. ‘An investigation of the quantum $J_1 - J_2 - J_3$ model on the honeycomb lattice’. In: *Eur. Phys. J. B* 20 (2001), p. 241.
- [85] M. J. Harris et al. ‘Geometrical Frustration in the Ferromagnetic Pyrochlore $\text{Ho}_2\text{Ti}_2\text{O}_7$ ’. In: *Phys. Rev. Lett.* 79 (1997), p. 2554.
- [86] N. P. Raju et al. ‘Transition to long-range magnetic order in the highly frustrated insulating pyrochlore antiferromagnet $\text{Gd}_2\text{Ti}_2\text{O}_7$ ’. In: *Phys. Rev. B* 59 (1999), p. 14489.
- [87] S. E. Palmer and J. T. Chalker. ‘Order induced by dipolar interactions in a geometrically frustrated antiferromagnet’. In: *Phys. Rev. B* 62 (2000), p. 488.

- [88] M. Elhajal et al. ‘Ordering in the pyrochlore antiferromagnet due to Dzyaloshinsky-Moriya interactions’. In: *Phys. Rev. B* 71 (2005), p. 094420.
- [89] O. Tchernyshyov, R. Moessner and S. L. Sondhi. ‘Spin-Peierls phases in pyrochlore antiferromagnets’. In: *Phys. Rev. B* 66 (2002), p. 064403.
- [90] E. F. Shender et al. ‘Kagomé antiferromagnet with defects: Satisfaction, frustration, and spin folding in a random spin system’. In: *Phys. Rev. Lett.* 70 (1993), p. 3812.
- [91] R. Moessner and A. J. Berlinsky. ‘Magnetic Susceptibility of Diluted Pyrochlore and $\text{SrCr}_{9-9x}\text{Ga}_{3+9x}\text{O}_{19}$ Antiferromagnets’. In: *Phys. Rev. Lett.* 83 (1999), p. 3293.
- [92] T. E. Saunders and J. T. Chalker. ‘Spin Freezing in Geometrically Frustrated Antiferromagnets with Weak Disorder’. In: *Phys. Rev. Lett.* 98 (2007), p. 157201.
- [93] G. H. Wannier. ‘Antiferromagnetism. The Triangular Ising Net’. In: *Phys. Rev.* 79 (1950), p. 357.
- [94] J. Stephenson. ‘Ising-Model Spin Correlations on the Triangular Lattice. III. Isotropic Antiferromagnetic Lattice’. In: *Jour. of Math. Phys.* 11 (1970), p. 413.
- [95] T. Horiguchi, O. Nagai and S. Miyashita. ‘Structure of Ground States of Antiferromagnetic Ising Model with General-Spin on Triangular Lattice’. In: *J. Phys. Soc. Jpn.* 60 (1991), p. 1513.
- [96] O. Nagai, S. Miyashita and T. Horiguchi. ‘Ground state of the antiferromagnetic Ising model of general spin S on a triangular lattice’. In: *Phys. Rev. B* 47 (1993), p. 202.
- [97] O. Nagai et al. ‘Spin-ordering property of Ising model with general spin S on an antiferromagnetic triangular lattice’. In: *Phys. Lett. A* 195 (1994), p. 263.
- [98] A. Lipowski, T. Horiguchi and Y. Honda. ‘Partial ordering at the ground state of frustrated spin- S Ising models’. In: *Phys. A: Stat. Mech. Appl.* 237 (1997), p. 297.
- [99] C. Zeng and C. L. Henley. ‘Zero-temperature phase transitions of an antiferromagnetic Ising model of general spin on a triangular lattice’. In: *Phys. Rev. B* 55 (1997), p. 14935.
- [100] B. D. Metcalf. ‘Ground state spin orderings of the triangular Ising model with the nearest and next nearest neighbor interaction’. In: *Phys. Lett. A* 46 (1974), p. 325.
- [101] V. L. Berezinskii. ‘Destruction of Long-range Order in One-dimensional and Two-dimensional Systems having a Continuous Symmetry Group I. Classical Systems’. In: *J. Exp. Theor. Phys* 32 (1971), p. 493.
- [102] V. L. Berezinskii. ‘Destruction of Long-range Order in One-dimensional and Two-dimensional Systems Possessing a Continuous Symmetry Group. II. Quantum Systems’. In: *J. Exp. Theor. Phys* 34 (1972), p. 610.
- [103] J. M. Kosterlitz and D. J. Thouless. ‘Ordering, metastability and phase transitions in two-dimensional systems’. In: *J. Phys. C: Sol. St. Phys.* 6 (1973), p. 1181.
- [104] J. M. Kosterlitz. ‘The critical properties of the two-dimensional xy model’. In: *J. Phys. C: Sol. St. Phys.* 7 (1974), p. 1046.

- [105] D. P. Landau. ‘Critical and multicritical behavior in a triangular-lattice-gas Ising model: Repulsive nearest-neighbor and attractive next-nearest-neighbor coupling’. In: *Phys. Rev. B* 27 (1983), p. 5604.
- [106] S. Fujiki et al. ‘Monte Carlo Simulation of the Antiferromagnetic Ising Model on the Triangular Lattice with the First and Second Neighbour Interactions’. In: *J. Phys. Soc. Jpn.* 52 (1983), p. 1531.
- [107] H. Takayama et al. ‘Monte Carlo Study of a Triangular Ising Lattice. II. Occurrence of the Kosterlitz-Thouless-Like Phase Transition’. In: *J. Phys. Soc. Jpn.* 52 (1983), p. 2888.
- [108] N. G. Fytas and A. Malakis. ‘Criticality in the randomness-induced second-order phase transition of the triangular Ising antiferromagnet with nearest- and next-nearest-neighbor interactions’. In: *Phys. A: Stat. Mech. Appl.* 388 (2009), p. 4950.
- [109] Z. Hu et al. ‘Evidence of the Berezinskii-Kosterlitz-Thouless phase in a frustrated magnet’. In: *Nat. Commun.* 11 (2020), p. 5631.
- [110] S. E. Korshunov, A. Vallat and H. Beck. ‘Frustrated XY models with accidental degeneracy of the ground state’. In: *Phys. Rev. B* 51 (1995), p. 3071.
- [111] T. Garel and S. Doniach. ‘On the critical behaviour of two-dimensional XY helimagnets’. In: *J. Phys. C: Sol. St. Phys.* 13 (1980), p. L887.
- [112] M. Hébert and A. Caillé. ‘Mean-field phase diagram of a coupled XY-Ising model for discotic liquid crystals’. In: *Phys. Rev. E* 51 (1995), R1651.
- [113] P. Minnhagen. ‘The two-dimensional Coulomb gas, vortex unbinding, and superfluid-superconducting films’. In: *Rev. Mod. Phys.* 59 (1987), p. 1001.
- [114] N. D. Mermin. ‘The topological theory of defects in ordered media’. In: *Rev. Mod. Phys.* 51 (1979), p. 591.
- [115] D. H. Lee et al. ‘Discrete-Symmetry Breaking and Novel Critical Phenomena in an Antiferromagnetic Planar (XY) Model in Two Dimensions’. In: *Phys. Rev. Lett.* 52 (1984), p. 433.
- [116] S. Miyashita and H. Shiba. ‘Nature of the Phase Transition of the Two-Dimensional Antiferromagnetic Plane Rotator Model on the Triangular Lattice’. In: *J. Phys. Soc. Jpn.* 53 (1984), p. 1145.
- [117] J. D. Noh et al. ‘Critical behavior of the frustrated antiferromagnetic six-state clock model on a triangular lattice’. In: *Phys. Rev. E* 66 (2002), p. 026111.
- [118] A. B. Lima, L. A. S. Mól and B. V. Costa. ‘The Fully Frustrated XY Model Revisited: A New Universality Class’. In: *J. Stat. Phys.* 175 (2019), p. 960.
- [119] D. H. Lee et al. ‘Symmetry analysis and Monte Carlo study of a frustrated antiferromagnetic planar (XY) model in two dimensions’. In: *Phys. Rev. B* 33 (1986), p. 450.
- [120] J. Sznajd and J. Zittartz. ‘The low temperature phase in the 2D quantum XY model’. In: *J. Magn. Magn. Mat.* 104 (1992), p. 220.

- [121] S. Homma et al. ‘Thermodynamic Properties of Antiferromagnetic Quantum XY-Model on the Triangular Lattice’. In: *J. Phys. Soc. Jpn.* 62 (1993), p. 880.
- [122] K. Harada and N. Kawashima. ‘Kosterlitz-Thouless Transition of Quantum XY Model in Two Dimensions’. In: *J. Phys. Soc. Jpn.* 67 (1998), p. 2768.
- [123] A. W. Sandvik and C. J. Hamer. ‘Ground-state parameters, finite-size scaling, and low-temperature properties of the two-dimensional $S = \frac{1}{2}$ XY model’. In: *Phys. Rev. B* 60 (1999), p. 6588.
- [124] A. Yu. Nikulin et al. ‘Preparation and characterization of metastable trigonal layered MSb_2O_6 phases (M = Co, Ni, Cu, Zn, and Mg) and considerations on FeSb_2O_6 ’. In: *Dalton Trans.* 46 (2017), p. 6059.
- [125] T. Ungár. ‘Characterization of nanocrystalline materials by X-ray line profile analysis’. In: *J. Mat. Sc.* 42 (2007), p. 1584.
- [126] P. Mendels et al. ‘Quantum Magnetism in the Paratacamite Family: Towards an Ideal Kagomé Lattice’. In: *Phys. Rev. Lett.* 98 (2007), p. 077204.
- [127] E. M. Kenney et al. ‘Coexistence of static and dynamic magnetism in the Kitaev spin liquid material Cu_2IrO_3 ’. In: *Phys. Rev. B* 100 (2019), p. 094418.
- [128] Y. J. Uemura et al. ‘Muon-spin relaxation in AuFe and CuMn spin glasses’. In: *Phys. Rev. B* 31 (1985), p. 546.
- [129] Y. J. Uemura et al. ‘Spin Fluctuations in Frustrated Kagomé Lattice System $\text{SrCr}_8\text{Ga}_4\text{O}_{19}$ Studied by Muon Spin Relaxation’. In: *Phys. Rev. Lett.* 73 (1994), p. 3306.
- [130] D. Bono et al. ‘ μSR Study of the Quantum Dynamics in the Frustrated $S = \frac{3}{2}$ Kagomé Bilayers’. In: *Phys. Rev. Lett.* 93 (2004), p. 187201.
- [131] J. A. Quilliam et al. ‘Gapless quantum spin liquid ground state in the spin-1 antiferromagnet $6\text{HB-Ba}_3\text{NiSb}_2\text{O}_9$ ’. In: *Phys. Rev. B* 93 (2016), p. 214432.
- [132] E. Kermarrec et al. ‘Spin-liquid ground state in the frustrated kagome antiferromagnet $\text{MgCu}_3(\text{OH})_6\text{Cl}_2$ ’. In: *Phys. Rev. B* 84 (2011), p. 100401.
- [133] P. Mendels et al. ‘Quantum Magnetism in the Paratacamite Family: Towards an Ideal Kagomé Lattice’. In: *Phys. Rev. Lett.* 98 (2007), p. 077204.
- [134] M. Gomilsek et al. ‘Instabilities of spin-liquid states in a quantum kagome antiferromagnet’. In: *Phys. Rev. B* 93 (2016), p. 060405.
- [135] B. Fåk et al. ‘Kapellasite: A Kagome Quantum Spin Liquid with Competing Interactions’. In: *Phys. Rev. Lett.* 109 (2012), p. 037208.
- [136] L. Clark et al. ‘Gapless Spin Liquid Ground State in the $S=1/2$ Vanadium Oxyfluoride Kagome Antiferromagnet $[\text{NH}_4]_2[\text{C}_7\text{H}_{14}\text{N}][\text{V}_7\text{O}_6\text{F}_{18}]$ ’. In: *Phys. Rev. Lett.* 110 (2013), p. 207208.
- [137] Y. Shen et al. ‘Fractionalized excitations in the partially magnetized spin liquid candidate YbMgGaO_4 ’. In: *Nat. Comm.* 9 (2018), p. 4138.

- [138] M. B. Stone et al. ‘Frustrated three-dimensional quantum spin liquid in CuHpCl’. In: *Phys. Rev. B* 65 (2002), p. 064423.
- [139] S. Gong et al. ‘Chiral spin liquid with spinon Fermi surfaces in the spin- $\frac{1}{2}$ triangular Heisenberg model’. In: *Phys. Rev. B* 100 (2019), p. 241111.

CURRICULUM VITAE

Safiulina Irina

EPFL & ILL PhD student

16/02/1993 (Chelyabinsk, Russia)

Employment History

- Electronic engineer at Saint Petersburg State University, Saint Petersburg (January 2015 – June 2015)
- Research laboratory assistant at Petersburg Nuclear Physics Institute, Gatchina (October 2015 – August 2017)
- PhD student at Institute Laue-Langevin, Grenoble (September 2017 – August 2020)
- PhD student at EPFL, Lausanne (September 2021 – February 2022)

Education

- Bachelor Degree in Physics, Physics Department, Saint Petersburg State University, Saint Petersburg (September 2010 – August 2015); thesis title "Development of a prototype of a one-coordinate scintillator fiber neutron detector"
- Master degree in Physics with distinction, Physics Department, Saint Petersburg State University, Saint Petersburg (September 2015 – August 2017); thesis title "Investigation of the mesoscopic structure of transition metal monogermanides"
- PhD at École polytechnique fédérale de Lausanne, Lausanne (September 2017 – February 2022); thesis title "Spinon-like excitations in spin-1/2 quantum antiferromagnets"

Publications

- I. A. Safiulina, E. V. Altynbaev, E. G. Iashina A. Heinemann, L. N. Fomicheva, A. V. Tsvyashchenko, and S. V. Grigoriev. Investigation of the Mesostructure of Transition-Metal

Monogermanides Synthesized under Pressure. In: *Phys. Sol. St.* 60 (2018), p. 751.

- A. Korshunov, I. Safiulina, and A. Kursbakov. Spin Correlations and Short-Range Magnetic Order in the Honeycomb-Layered $\text{Na}_2\text{Ni}_2\text{TeO}_6$. In: *PSSb* 257 (2019), p. 1900232.
- A. N. Korshunov, A. I. Kurbakov, I. A. Safiulina, A. E. Susloparova, V. Yu. Pomjakushin, and Th. Mueller. Long-range magnetic ordering in $\text{Li}_2\text{MnGeO}_4$ and precursor short-range spin correlations. In: *Phys. Rev. B* 102 (2020), p. 214420.